Development of Numerical Modeling Methods for Prediction of Ignition Processes in Aero-Engines

Vom Fachbereich Maschinenbau
an der Technischen Universität Darmstadt
zur
Erlangung des Grades eines Doktor-Ingenieurs (Dr.-Ing.)
genehmigte

D i s s e r t a t i o n

von

Dipl.-Ing. Jeremy Weckering

geboren in Toul, Frankreich

Berichterstatter:	Prof. Dr.–Ing. J. Janicka
Mitberichterstatter:	Prof. E. Mastorakos
Tag der Einreichung:	04. 05. 2010
Tag der mündlichen Prüfung:	25. 06. 2010

Darmstadt 2011
D 17

Acknowledgments

This thesis encompasses the work performed during my research at the institute "Energy and Powerplant Technology" (EKT) at Darmstadt University of Technology, where I was a foundation member of the Graduate Program GRK1344 "Unsteady System Modeling of Aircraft Engines" of the German Research Foundation (DFG). The financial support from Darmstadt University of Technology is also gratefully acknowledged.

I would like to express my gratitude to my supervisor, and head of institute EKT, Prof. Dr.-Ing. Johannes Janicka, for his valuable advice, continuous encouragement and guidance while giving large autonomy. Prof. Dr.rer.nat. Amsini Sadiki always readily offered his advice in scientific matters and beyond, aid in publications and manuscript revision. Dr. Robert Gordon provided fruitful discussion about autoignition and, specifically, the vitiated coflow burner. Thomas Breitenberger and Martin Obermüller performed substantial code validation work within their diploma theses under my supervision. Thomas' contribution to LES validation was outstanding.

Dr.-Ing. Thomas Doerr, head of Rolls-Royce Deutschland combustion department, welcomed me during my six-month stay in Dahlewitz and gave me insight into the technical issues of ignition in aero-engines. Dr. Ruud Eggels provided intensive advice on chemistry modeling. Dr.-Ing. Max Staufer's support in code development and great cooperation were also highly valued.

Prof. Epaminondas Mastorakos welcomed me at Cambridge University during Spring 2009. He provided valuable advice and substantial aid in publications. The support of Dr. Antonios Triantafyllidis was also appreciated.

Many thanks to my colleagues at EKT, GRK1344, Rolls-Royce and the Hopkinson Laboratory who exchanged ideas with me and made my PhD enjoyable. Pradeep Pantangi and Markus Schmitt were particularly affable during the final stage of this work. The support of the computer administration and office teams were highly valued. The English editing advice of Larissa Moore is gratefully acknowledged.

For their unfailing support despite the distance, my gratitude goes to my parents Liliane and Francis Weckering, my sister Marjorie and my friends Constanze, Fred, Alex, Matthieu and Katharina.

Ainsi la contemplation de la flamme pérennise une rêverie première. Elle nous détache du monde et elle agrandit le monde du rêveur. La flamme est à elle seule une grande présence, mais, près d'elle, on va rêver loin, trop loin: « on se perd en rêveries. » La flamme est là, menue et chétive, luttant pour maintenir son être, et le rêveur s'en va rêver ailleurs, perdant son propre être, en rêvant trop grand – en rêvant au monde. La flamme est un monde pour l'homme seul.

La Flamme d'une Chandelle, Gaston Bachelard (1884-1962)

Zusammenfassung

Entwicklung von numerischen Modellierungsmethoden zur Vorhersage von Zündprozessen in Flugtriebwerken

Gegenstand dieser Arbeit ist die Entwicklung von numerischen Methoden zur Vorhersage von Zündprozessen mit dem übergeordneten Ziel, die Wiederzündbarkeit von Flugtriebwerken bei großen Flughöhen numerisch ermitteln zu können. Die Motivation erwächst aus einem verstärkten technischen Interesse der Industrie, numerische Methoden zur Vorhersage der Zündbarkeit einer Brennkammer einzusetzen.

In der Tat sind neue Verbrennungskonzepte zur weiteren Senkung der Emissionen von thermischen Stickoxiden durch instabile Verbrennungsbedingungen gekennzeichnet. Gleichzeitig erschweren diese Bedingungen den erfolgreichen Ablauf der Wiederzündung. Folglich ist die Entwicklung von effizienteren Flugtriebwerken durch die notwendige Sicherstellung der effektiven Wiederzündung der Brennkammer bei allen Betriebsbedingungen beeinträchtigt. Schließlich erweisen sich niedrige Drücke und niedrige Temperaturen bei großen Flughöhen als besonders ungünstig und stehen im Mittelpunkt der Bemühungen zur verbesserten Wiederzündbarkeit von Triebwerken.

Darüber hinaus erfordern magere Verbrennungskonzepte komplexe Luft-Brennstoff-Mischungsprozesse. Dies führt zur komplexen Brennkammergeometrien, die als numerische Gitter mit Multi-Block Strukturen nur mit großem Aufwand vernetzt werden können. Deshalb wurde die Entwicklung eines unstrukturierten Codes zur Strömungssimulation vorangetrieben. Dieser Code, PRECISE-UNS (Predictive-System for Real Engine Combustors - Unstructured), basiert auf dem Finite Volumen Code Dolfyn, dessen Fortran Quelltext zugänglich ist. Alle dokumentierten Untersuchungen wurden mit PRECISE-UNS durchgeführt.

Die erfolgreiche Zündung einer Brennkammer besteht aus mehreren Phasen, darunter die Flammen-Kern-Generierung, der Kern-Wachstum, die Kern-Konvektion, die Flammen-Ausbreitung und -Stabilisierung. Zündsequenzen sind also instationäre Phänomenen, die sich einerseits durch die Interaktion zwischen der langsamen Chemie und der

turbulenten Strömung auszeichnen und andererseits ausgeprägte probabilistische Eigenschaften aufweisen. Daher wurden zwei Methoden entwickelt und verwendet, die diese Eigenschaften erfassen können.

Zunächst wurde eine rechenzeit-effiziente Methode mit Fortschrittsvariablen-Ansatz entwickelt. Diese Methode ermöglicht die Berücksichtigung der Interaktion zwischen der langsamen Chemie und der turbulenten Strömung durch die Anwendung von Wahrscheinlichkeitsdichtefunktionen. An einer, in einer heißen Begleitströmung selbstzündenden, abgehobenen, turbulenten Methan-Jet-Flamme wurde die Methode angewandt. Hierzu konnte eine abgehobene Flamme simuliert und deren Stabilisierungsmechanismus identifiziert werden. Insbesondere konnte das Verlöschen von gezündeten, sehr mageren Fluid-Elementen durch schnelle Mischung mit dem kalten Jet nachgewiesen werden. Dadurch wurde die Eignung der Methode validiert, Effekte der Interaktion zwischen der langsamen Chemie und der turbulenten Strömung wiederzugeben.

Der zweite wichtiger Punkt dieser Arbeit besteht in der Entwicklung einer besonders rechen-effizienten Methode zur statistischen Untersuchung von Zündprozessen. Zur Simulation instationärer Phänomenen in technischen Systemen ist die Methode der Grobstruktursimulation, im Englischen Large-Eddy Simulation (LES), besonders geeignet und wurde zur Simulation von Zündsequenzen eingesetzt. Der einhergehende große Rechenaufwand verbietet jedoch jegliche aussagekräftige Ensemble Mittelung zur Ermittlung von statistischen Werten. Die neue Methode wurde konzipiert, um Ensemble Mittelung zu ermöglichen. Zum Monitoring der Zündereignisse verbindet diese Methode die Verfolgung von Lagrangeschen Partikeln mit LES und untersucht die lokale turbulente Flammengeschwindigkeit auf den Oberflächen von gezündeten Kernen. Die Methode basiert auf zwei Annahmen: (i) der Verlauf einer Zündung, von der Flammenkern-Generierung bis zum Übergang zu einer Flammenfront, ist durch das gesamte Strömungsfeld zum Zündzeitpunkt vorgegeben. (ii) Das Wachstum von Flammenkernen, inklusiv der Effekte der thermischen Expansion, kann unter Berücksichtigung von experimentellen Beobachtungen modelliert werden. Dadurch können die Oberflächen von mehreren Flammenkernen gleichzeitig erfasst werden sowie Zündereignissen, die an unterschiedlichen Orten initiiert wurden, gleichzeitig simuliert werden. Schließlich wird der statistische Verlauf von Zündungsereignissen unter der Berücksichtigung der korrelierten Effekte (i) der Strömungsbedingungen am Ort der Zündvorrichtung, (ii) der Konvektion des Kerns und (iii) des Übergangs des Kerns zu einer ausbreitenden Flammenfront untersucht. Die Methode wurde an einem fremdgezündeten, nicht-vorgemischten Methan-Jet angewandt. Die konditionierten Wahrscheinlichkeiten von Flammenkern Generierung, Konvektion, Wachstum und Stabilisierung stimmen mit den experimentell gemessenen Zündwahrscheinlichkeiten gut überein.

Abstract

Development of Numerical Modeling Methods for Prediction of Ignition Processes in Aero-Engines

The focus of this thesis is the development of numerical methods for the prediction of ignition processes as part of predicting the relight capability of aero-engines at high altitudes. It is motivated by an increased demand from aero-engine designers for numerical prediction of the ignitability of modern combustion chambers.

Development of lean burn concepts for reducing the formation of thermal nitrogen oxides is accompanied by less stabile combustion conditions, which negatively affect ignition processes, leading to full relight of the combustor. Consequently, the development of advanced aero-engines is impeded by the necessity of ensuring an effective relight in all operating conditions. The adverse conditions of low pressure and low temperature at high altitudes are the focus of efforts to develop combustors with advanced relight capability.

Lean-burn combustion concepts imply complex air-fuel mixing and therefore complex combustor geometries, which are laborious to mesh with multi-block mesh structures. A code for computational flow dynamics (CFD) that is able to handle unstructured meshes was necessary. This code, PRECISE-UNS (Predictive-System for Real Engine Combustors - Unstructured), is built on Dolfyn, an open-source code written in Fortran. All investigations documented in this work have been performed using PRECISE-UNS.

The effective ignition of a combustor consists of several phases, including the initiation of a kernel of flame, kernel growth and convection, and flame propagation followed by stabilization. Ignition events are intrinsically unsteady combustion phenomena, characterized by slow chemistry effects interacting with the turbulent flow, and probabilistic properties. Therefore two methods have been developed and applied for capturing these effects.

First a computationally time-efficient method based on a progress variable approach and relying on probability density functions for considering the interaction between slow

chemistry and turbulent flow has been developed. This method was applied to a turbulent methane-air jet flame autoigniting in a hot coflow. The lifted flame could be simulated and the stabilization mechanism identified. In particular, the quenching of ignited, very lean fluid elements by the cold jet could be demonstrated. Thus, the ability of the method to reproduce the effects of slow chemistry interaction with the turbulent flow could be validated.

Secondly a particularly cost-effective method for performing statistical investigations of spark ignition has been designed. For this purpose, the method of Large-Eddy Simulation (LES), which is particularly useful in technical systems for simulating unsteady phenomena, such as spark ignition events, was considered. It was successfully applied in simulating ignition sequences. However, the computational cost of such time-resolved investigations is too high for performing statistical analysis based on ensemble averaging. The new method, that has been designed for enabling ensemble averaging, couples LES to a Lagrangian monitoring of fluid particles and explores the effects of local turbulent flow properties on upstream and downstream flame propagation in the axial direction following radial kernel growth through a sub-grid turbulent flame speed model. The method is based on two assumptions: (i) the evolution of an ignition event, from initiation to transition, then to a propagating flame, is determined by the global turbulent flow at ignition time. (ii) The growth of an ignited kernel can be modeled using experimental observations. Thus, the surface of several flame kernels can be captured simultaneously, as well as ignition events that have been generated at different locations. Finally, the conditional statistics of ignition events are analyzed for the joint probabilistic behavior of (i) kernel generation, (ii) convection and (iii) subsequent flame propagation. The method was applied to a spark ignited, non-premixed methane jet. The conditional probability of formation, convection, growth and stabilization of flame kernels results in prediction of the overall flame ignition probability, which agrees well with experimental data.

Contents

List of Figures

Nomenclature

Uppercase Latin letters

$A_{i,R}$	Arrhenius' pre-exponential constant
C_g	Germano constant
C_s	Smagorinsky constant
D	Diffusivity
$E_{k,i,R}$	Activation energy
J	Jacobi matrix
M_k	Molecular weight
R	Universal gas constant
S_ij	Strain rate tensor
T	Temperature
$Y_c,\ Y_{eq}$	Progress variable, progress variable value at equilibrium

Lowercase Latin letters

c	Normalized Progress Variable
c_p	Specific heat capacity
f	Mixture fraction
g	Gravity
h	Enthalpy
k	Turbulent kinetic energy
$k_{f,R},\ k_{b,R}$	Forward, backward reaction rate-coefficent
l_t	Integral length scale
$m,\ \dot{m}$	Mass, mass flux
p	Pressure (1 psi = 6 894 Pa)
$r_{f,R},\ r_{b,R}$	Forward, backward reaction rate
s_L	Laminar flame speed
s_T	Turbulent flame speed
t_{ign}	Ignition delay
u_i	Velocity
z_k	Element mass-fraction

Uppercase Greek letters

Δ	LES filter width
Γ	LES filter width

Lowercase Greek letters

χ	Scalar dissipation rate
δ_f	Flame thickness
δ_{ij}	Kronecker symbol
$\dot{\omega_x}$	Source of "x"
η_k	Kolmogorov length scale
λ	Heat conductivity
μ	Dynamic viscosity
ν	Kinematic viscosity
$\nu''_{k,R}$	Stoichiometric coefficients of products
$\nu'_{k,R}$	Stoichiometric coefficients of reactants
ϕ	Equivalence ratio
ϕ	Scalar
ψ	Thermochemical composition space
ρ	Density
τ_C	Chemical reaction time scale
τ_T	Turbulent time scale
τ_{ij}	Stress tensor
τ_k	Kolmogorov time scale
ε	Kinetic energy dissipation rate

Operators and Symbols

$< . >$	Time averaging operator
$\bar{.}$	Time averaging operator
$\dot{.}$	Time derivative
$\tilde{.}$	Favre averaging operator

Dimensionless Numbers

Da	Damköhler Number
Ka	Karlowitz Number
Le	Lewis number
Re	Reynolds Number
Sc	Schmidt Number

Abbreviations

AFR	Air-Fuel Ratio
AI	Autoignition
ATF	Artificially Thickened Flame
CAEP	Committee on Aviation and Environmental Protection
CDS	Central Differencing Scheme
CFD	Computational Fluid Dynamics
CFL	Courant-Friedrichs-Lewy (number)
CMC	Conditional Moment Closure
DNS	Direct Numerical Simulation
EBU	Eddy Break-Up
FAR	Fuel-Air Ratio
FDF	Filtered Density Function
FGM	Flamelet Generated Manifold
GRI	Gas Research Institute
ICAO	International Civil Aviation Organization
LDI	Lean Direct Injection
LES	Large-Eddy Simulation
LP(P)	Lean Premixed Partially vaporized
LPP	Lean Premixed Pre-vaporized
MIE	Minimum Ignition Energy
PDF	Probability Density Function
PRECISE-MB	Predictive-System for Real Engine Combustors - MultiBlocking
PRECISE-UNS	Predictive-System for Real Engine Combustors - Unstructured
RANS	Reynolds Averaged Navier Stokes
RQL	Rich burn - Quick quench - Lean burn
RR	Rolls-Royce
SGS	Sub-Grid Scale
UDS	Upwind Differencing Scheme
VCB	Vitiated Coflow Burner

1 Introduction

Innovations in combustion technology are crucial for an ecologically sustainable supply of affordable water, heating, electricity and transportation. In power production, gas turbines are used extensively both for electric power and mechanical drive applications. Technical issues associated with ignition phenomena impede the development of new combustion concepts for further reduction of the formation of thermal nitrogen oxides within gas turbine combustion chambers. This work aims to develop methods for predicting ignition processes, as they are essential for the design of advanced combustors in aero-engines.

1.1 General Issues related to Combustion

The transformation from pre-industrialized to modern industrial societies in the late eighteenth century closely relates to a considerable increase in energy demand. More than 80% of energy converted now relies on the combustion of fossil fuels [86]. Although global energy consumption reduced exceptionally in 2009 as a result of the financial and economic crisis, the *International Energy Agency* (IEA) predicts the demand to resume its long-term upward trend. According to a *Reference Scenario* that assumes no change in government policies, combustion is set to maintain its dominant position in energy production, with fossil fuels forecast to account for 77% of the 40% demand increase from 2007 to 2030 [86].

Driven by increasing oil prices, energy efficiency and carbon dioxide intensity have steadily and considerably improved in recent decades. Although further notable improvements are expected, especially in transport and industry, energy-related carbon dioxide CO_2 emissions are projected to rise from 28.8 Gt in 2007 to 40.2 Gt in 2030 [86]. *Cap and trade* schemes, such as the *European Union Emission Trading Scheme* which has included aviation activities since 2008 [58], provide industry with tangible objectives by giving a price to CO_2 emissions. The economic incentives of emission trading schemes are likely to profoundly redefine optimization criteria.

Local and global environmental concerns gear the development of combustion systems towards reduced noise and exhaust gas emissions. The emission of nitrogen oxides NO_x due to combustion particularly has serious public health and environmental effects. NO_x reacts with volatile organic compounds in the presence of sunlight to form ozone (O_3). Ground-level ozone can be transported by wind currents and cause ill health far from the original sources [55]. Nitrogen oxides are also involved in smog formation.

The 2007 assessment report by the *Intergovernmental Panel on Climate Change* (IPCC) [84] noted that changes in atmospheric concentrations of greenhouse gases and aerosols alter the energy balance of the climate system, and concluded that an "increase in anthropogenic greenhouse gas concentrations is very likely to have caused most of the increases in global average temperatures since the mid-20th century". Thus, a scientific consensus on the stringency of limiting anthropogenic greenhouse gas emissions has been achieved. The political endorsement of these conclusions has not been achieved yet. However, industrialists are already seriously considering environmental concerns in their development strategies.

In this context, the sector of air transportation presents particularly challenging issues. Firstly, air traffic is developing all over the world and its contribution to global CO_2 emissions is also increasing. Projections to 2050 by the IPCC [83] range from 7162 Mt to 2442 Mt compared to CO_2 emissions of 480 Mt in 2002. Secondly, in addition to CO_2 emissions, the chemical species released at cruise altitude during the fuel combustion process have a highly complex and certain impact on the global radiation balance of the atmosphere. Nitrogen oxides (NO_x) are particularly good at forming the greenhouse gas ozone when emitted at cruise altitudes. Depending on meteorological conditions, processes in exhaust plumes involving water vapor and aerosols may lead to the formation of persistent condensation trails, affecting upper troposphere cirrus cloudiness and the moisture budget [85].

According to IPCC estimations, the total climate impact of aviation, except highly uncertain cirrus cloud effects, is currently two to four times higher than the effect of its past carbon dioxide emissions alone. In 2001, the *Advisory Council for Aeronautics Research in Europe* (ACARE), a public-private joint initiative of the *Directorate-General for Transport and Energy* of the European Commission published it's prospective report "A Vision for 2020" [59] which appealed for cleaner and quieter aircrafts. The council's recommendations for 2020 consist of a 50% cut in CO_2 emissions and an 80% cut in NO_x emissions compared to their levels in 2000.

Regulatory approaches such as the ICAO Landing Take-Off cycle (LTO) Certification Standards in the aviation sector and the *Euro* [57] and *Tier* [54] emissions standards in the automotive sector, could effectively enforce considerable improvements in emissions. However, further technology forcing is a highly contentious topic in aircraft emissions, since trade-offs exist. Indeed, in the constant striving for more fuel-efficient engines, the overall pressure ratio (OPR) has tended to increase, so that the emissions index for NO_x (EINO_x, g NO_x/kg fuel) has increased over time, across the global fleet [56]. The regulating agency of the *United Nations*, the *International Civil Aviation Organization* (ICAO), could not ignore this. In 2004, the ICAO *Committee on Aviation and Environmental Protection* (CAEP), after setting legislative limits for NO_x emissions (CAEP6), agreed that NO_x stringency would not be further reviewed until CAEP8 in 2010. However, reducting NO_x emissions is of utmost importance to combustor developers as it is directly related to ignition phenomena.

1.2 Technical Issues associated with Ignition Phenomena

1.2.1 Design of Modern Combustion Systems

Given the profound implications of combustion emissions on environmental protection, significant research efforts are focused on the development of advanced systems. In order to meet substantially tightened emissions standards, new combustion concepts are required. In the following paragraphs, general aspects of the design of combustion systems are first introduced. Advanced combustion concepts are then presented, with an emphasis on ignition-related issues.

Combustion systems are benchmarked to a set of properties. For some of these properties, regulations and explicit customer demands define the required levels. In addition, some other levels are targeted according to the marketing strategy, which showcases the product line-up and therefore adapts it to upcoming mandatory levels.

For aero-engines, Doerr [46] detailed the following four criteria: performance requirements, interface requirements, engine operability requirements and emissions requirements. These requirements can be applied to combustion systems in general. The performance requirements include combustion efficiency, durability, costs, weight and fuel-flexibility. Combustor integration is made possible by interface requirements. Engine operability means proper functioning under all operating conditions including transient regimes. Regulations define limits and penalties for emission levels from exhaust gases,

such as carbon monoxide (CO), unburnt hydrocarbons (UHC), sulfur dioxide (SO_2), nitrogen oxides (NO_x), carbon dioxide (CO_2) and soot (smoke) as well as for noise emissions.

Some of these properties can be improved simultaneously. Indeed improving fuel-efficiency has a direct impact on operating costs and CO_2 emissions. Progress in material science, including better understanding of environmentally induced fatigue phenomena (for example Weckering et al. [178]) and ceramic coating techniques, has permitted improved durability of turbomachinery components which reduces engine weight and increases compression ratios.

However, developers choose trade-offs. In particular, limiting the formation of NO_x implies a limitation in high temperatures, which impede thermodynamical efficiency and the oxidation of soot particles and UHC. The avoidance of stoichiometric conditions implies combustion concepts have complex air/fuel mixing, which is more likely to produce instabilities. Therefore, limiting NO_x emissions from aero-engines without impaired efficiency exacerbates the need for operability and, more specifically, relight capability. Integration aspects are also tightened. The occurrence of unsteady effects is more likely in lean burn conditions. Transient phenomena in the combustor, such as relight, affect the turbine and compressor too. The resulting transient loads must be taken into account in the design of both turbine and compressor. Despite deliberately targeting compact design, the combustor exit temperature traverse must be adapted to the high-pressure (HP) turbine nozzle guide vane (NGV). Since further reduction in emissions must be achieved without negatively affecting fuel-efficiency, new combustion systems concepts are required.

Research efforts concentrate on the development of combustion systems that emit low quantities of noxious nitrogen oxides. The development toward less NO_x emitting combustion concepts has specific technical issues. Among them, controlling ignition is identified as a major challenge. In combustion engines and gas turbines, the nitrogen oxides are mainly formed through high temperature oxidation of the nitrogen found in air, as per the Zeldovich mechanism [188]. The rate of formation of thermal NO_x is a function of the local temperature and oxygen concentration. Hence, low-NO_x concepts rely on low temperature combustion (LTC) that is achieved by operating under fuel-lean or fuel-diluted conditions. Fuel-lean conditions refer to high overall air/fuel ratios (AFR), low overall fuel/air ratios (FAR), while fuel-diluted conditions refer to dilution with inert gas obtained through exhaust gas recirculation (EGR). In the following, the ignition-related aspects of low NO_x combustion engines and aero-engine are emphasized.

Advanced Combustion Engines

Even though advanced combined exhaust gas post-treatment concepts specifically optimized for NO_x reduction have been developed in the automotive sector (Waldbüßer [174], Weckering [177]), preventing the formation of NO_x during combustion is preferred.

Advanced compression ignition engines relying on the LTC concept and delivering high efficiencies and low NO_x, such as Homogeneous Charge Compression Ignition (HCCI) and Premixed Charge Compression Ignition (PCCI) are currently being intensively investigated. As in conventional compression ignition engines, combustion is initiated by autoignition due to high temperatures induced by compression. The ignition time is determined by the time of the main injection. In many diesel engines, the ignition of the main injection is caused by interaction with a pre-ignited pilot injection, as numerically investigated by Hasse [74] (and Weckering [176]). Combustion in conventional diesel engines is mainly controlled by mixing. Thus, the fast pressure increase directly following ignition is only attributable to the combustion of the fuel part that is already vaporized. On the contrary, autoignition of homogeneous or premixed charges results in a much faster pressure increase. This characteristic constrains high loads operability. At low-loads, emissions and combustion efficiency deteriorate within HCCI engines. Indeed, the mixtures are so dilute that combustion temperatures are too low for bulk gas reactions to complete before they are quenched by the expansion stroke [43]. Enhanced stratifications are needed to smooth the pressure increase due to ignition at high loads, whereas HCCI/Spark-Ignition hybrid combustion systems have the ability to enhance low loads. Further information can be found in a review on in-cylinder processes in advanced compression ignition engines by Dec [43].

In *spray-guided spark-ignited direct injection* (SG SIDI) gasoline engines, highly stratified fuel charge and heavy dilution enable part-load operating conditions with high efficiency and low emissions. However, cycle-to-cycle variations are observed since the evolution of an ignited kernel of flame is sensitive to local equivalence ratios and transient flow conditions. Hence, robust ignition and complete combustion are key development issues, so that research efforts concentrate on the understanding of ignition processes (Fansler et al. [60] and Drake et al. [49])

Advanced Gas Turbines

Development of gas turbines combustors is driven by the need to minimize thermal NO_x formation. However, design options for aero-engine combustors are constrained by several requirements. In particular, lowering of the NO_x emissions cannot be achieved at the cost of engine operability in conditions such as *weak extinction*, *altitude relight*,

pull-away, *cold start* and *combustion instabilities*. In addition, *thrust-to-weight ratio*, complexity, durability and cost must be taken into account.

The *Rich Burn - Quick Quench - Lean Burn* (RQL) concept allows reduction in the residence time of reacting fluid elements at high NO_x formation rates without a dramatical increase of combustor complexity and weight. In this concept, combustion under rich conditions happens in a well-mixed first reaction zone with minimal cooling. The mixture is then rapidly diluted with secondary air in a quenching zone and finally convected into a secondary reaction zone for complete burn out under lean conditions. The rapid quenching prevents the combustion from occurring under stoichiometric conditions. This way, the "high NO_x route" as displayed in the principle diagram (Figure 1.1), is bypassed. Rolls-Royce has applied the RQL scheme in the RR Trent and RRD BR700 combustors (Figure 1.2). This concept can be further optimized with advanced quenching and reduced residence time. However, reducing residence time can affect the ignition capability of the combustor. Indeed, successful ignition requires the generation of a flame kernel which can propagate as a flame and stabilize in the recirculating flow of the primary combustion zone. Reducing the residence time of fluid elements within the combustion chamber also reduces the time taken for the flame kernel to reach the recirculation zone and thus increases the flame kernel's propensity to blow out.

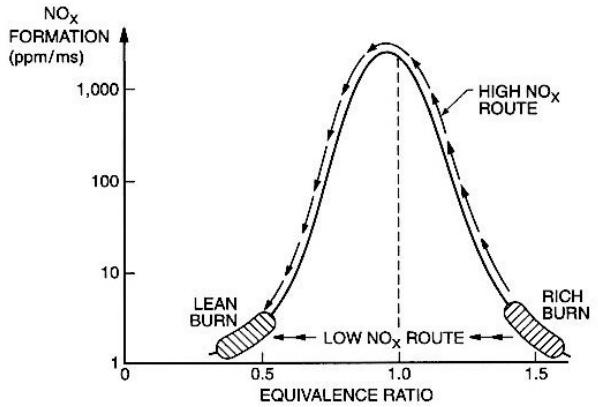

Figure 1.1: Principle of RQL combustion [112]

Further rich burn concepts have been developed, in which the weak extinction stability and altitude relighting are ensured by a pilot stage, whilst the high power main stage is optimized for low emissions. Pratt & Whitney has developed low-NO_x combustors, based on RQL, in the framework of its *Technology for Advanced Low* NO_x (TALON) program and claims NO_x production 70% below CAEP2 levels McKinney et al. [120]. Although rich burn combustion has a good performance record, it will presumably not cope with

medium to long term engine emissions requirements [46]. Subsequently, large civil engine combustor design is moving toward a lean burn approach [149].

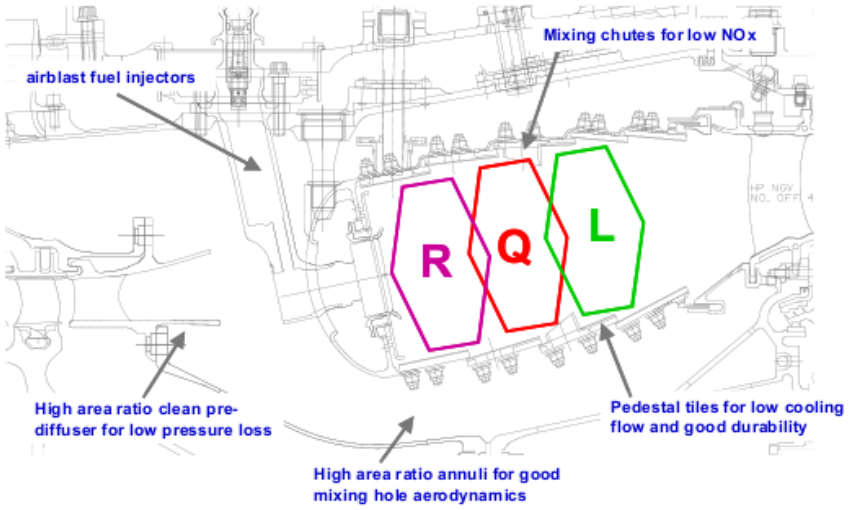

Figure 1.2: RQL principle applied to the RR Trent 900 combustor [46]

Lean Premixed Pre-vaporized (LPP) or *Lean Premixed Partially vaporized* (LP(P)) is a lean burn concept, in which pre-vaporization and premixing of the fuel are required before the mixture enters the combustion chamber. However, this concepts has several disadvantages. In the cold combustor at low pressure, the establishment of a sustainable ignition flame kernel may be impeded by fuel vapor concentrations below the lean flammability limit. In lean premixed combustion the stability of the burner may be unsettled by acoustic waves. This can lead to flame flashbacks, which could penetrate into the pre-vaporization zone. In addition, autoignition could be induced in the premixing duct due to operating temperatures and pressures, thus leading to the destruction of the combustor. Thus, the inherent risks of lean premixed fuel preparation represents a serious security obstacle to its implementation in commercial aero-engines.

In the Sequential EnVironmental (SEV) burners for stationary gas turbines made by the company ALSTOM (GT 24/26), a lean burn concept is applied in both combustion chambers. In the first chamber, fuel premixing is achieved within the upstream narrow part of a double-cone, where no autoignition is likely to occur. The double-cone leads directly into the combustion chamber and lean premixed combustion takes place in both the downstream part of the double-cone and the combustion chamber (see numerical simulations by Biagioli [12]) . Combustion within the sequential burner is initiated and controlled by autoignition of the fuel, which is injected into a high temperature oxidizer consisting of the exhaust gas from the first burner. The flame position is thus a result of the

autoignition of a turbulent mixture. Therefore, knowledge of the autoignition properties for the available fuel compositions and the effects of turbulent mixing is required when adjusting the configuration parameters to obtain a flame at its nominal position (see numerical simulations by Brandt [21]).

In the lean burn concept *Lean Direct Injection* (LDI) (US patent [30] and Nikolaus et al. [127]), fuel-air mixing is achieved in the combustion chamber by injectors alone, without mixing with secondary air. The fuel preparation is therefore not subject to uncontrolled effects before the combustion chamber. However, the LDI concept presents the following specific design challenges. The cooling of the chamber must be achieved without secondary air injection. The injectors have to ensure complex mixing that is adaptable for various operating conditions. According to the pre-filming air-blast concept [46], the injectors' modules consist of a concentric arrangement of a pilot fuel injector nested in the center of the main fuel stage, embedded into a large air swirler. As in staged RQL, the pilot zone is operating under rich conditions whilst the main flame is operating lean and ensures the burn out of the fuel injected by the pilot injector. Rapid quenching happens in the interaction zone, reducing the residing time at high NO_x formation rates. Controlling of this interaction zone is a key issue for optimization. Apart from fuel preparation security concerns, the move of lean burn combustion systems into service maturity levels is more likely to happen for systems based on LDI concepts [46].

A 50% reduction in NO_x emissions compared to the CAEP2 standards could be achieved within the framework of the low emissions programs RR ANTLE and RRD Engine3E [110, 46]. Within these programs Rolls-Royce demonstrated the potential of this technology to cope with tighter limits. The NOx reductions achieved by the programs must also be comparable with *Technology Readiness Levels* (TRL), such as engines in service.

This short review of modern combustion system design shows how the stringency of reducing emissions, especially nitrous oxides, gears the development of combustion systems towards advanced, low NO_x combustion concepts. In advanced compression engines, the sensitivity of autoignition to in-cylinder conditions has considerably increased, so that controlling autoignition is the main challenge. In lean premixed aero-engines, operating temperatures and pressures may induce uncontrolled autoignition in the mixing duct and the destruction of the combustor. More generally in aero-engines, the targeted reduction of residence time is hindered by the need for effective stabilization of ignition flame kernels in the adverse conditions at high altitudes. Therefore, controlling ignition is key to the development of next generation engines.

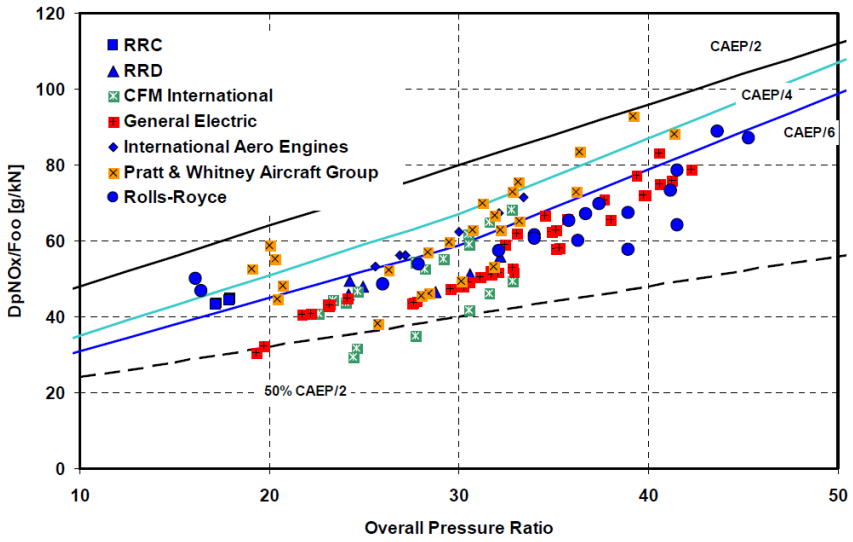

Figure 1.3: Low emissions combustion technology programs compared to legislative limits [46]. CAEP/6 shows the current limits. The y-axis shows the weighted NO_x emissions in grams per kN thrust. A weighting scheme is applied so that it is representative for a Landing Take-Off (LTO) cycle. The reference thrust is maximal value or take-off thrust F_{00}

1.2.2 Ignition in Aero-Engines

Ignition can be achieved using many different technical ignition systems. A review of the available sources of ignition, including spark ignition, torch igniter, glow plug, hot-surface ignition, plasma jet and laser ignition among others, can be found in [112]. However, ignition of aero-engine combustors is commonly achieved by energy deposition through electrical discharges visible as sparks. According to redundancy principles, two independent igniters are required for civil engine certification.

In surface discharge igniters, a semi-conducting pellet separates the central high-tension electrode and the igniter body (Figure 1.4). This pellet provides a low resistance path between the electrodes. The discharge ionizes the surface of the pellet and is observed as a high intensity flashover from the electrode to the body. Spark energy ranges from 2 J for small gas turbine engine applications to between 4 and 12 J in larger ones [112]. Typical values for duration and rate are 10 μs, and 50 to 250 sparks per minutes respectively [23]. Igniters need to be replaceable units since they undergo erosion. They are used for starting and relighting after a flame goes out and are also operated during landing and inclement weather conditions to prevent extinction induced by hail or rain ingestion.

During starting, fuel atomization and favorable flow conditions must first be achieved before the combustors can be ignited. To do this, a small gas turbine called the *Auxiliary Power Unit* is used to supply starters with compressed air. The starter first activates

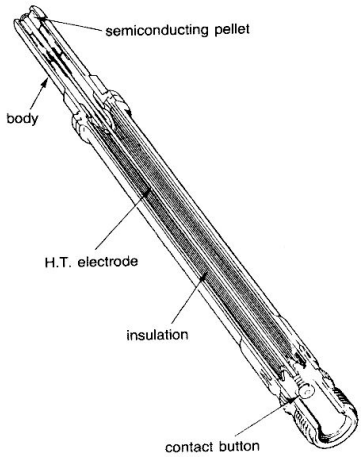

Figure 1.4: Surface discharge igniter [112]

the high pressure compressor and then the whole turbo-machinery [23]. The fuel pump is activated as soon as air flows through the combustor so that fuel atomization is effective. Low ambient temperatures affect the fuel, so that atomization and vaporization are hampered by high viscosity and low volatility. Therefore, starting the combustor can be difficult under cold start conditions. In addition, acceleration to idle conditions is affected by low combustion efficiencies due to cold fuel.

After a flame out event during flight at high aircraft speeds, the static pressure in front of the engine can sustain the rotation of the shafts through a windmill effect. Despite a pressure loss inside the combustion chamber, gas flows through the combustor and a certain fuel atomization is achieved, so that quick relighting is possible. At lower aircraft speeds, relight is achieved with the assistance of the starter. The compressed air supply is then taken overassumed by the active engine(s). Customers demand that relight after a total power loss must also be achievable solely by windmilling. In case of prolonged power loss, low temperatures affect combustor and fuel; both relight and acceleration capabilities can be drastically affected in a cold soaked engine [46].

Successful ignition requires favorable conditions in terms of FAR and air mass flow through the combustor. Hence, a typical gas turbine ignition loop can be defined in this coordinate system (Figure 1.5). The ignitable domain delineated by this curve is within the combustion stability loop. The lower branch represents the weak stability limit. In lean burn combustion systems, flame-out, as caused by *Lean Blow Out* (LBO) is likely to occur when this limit is reached.

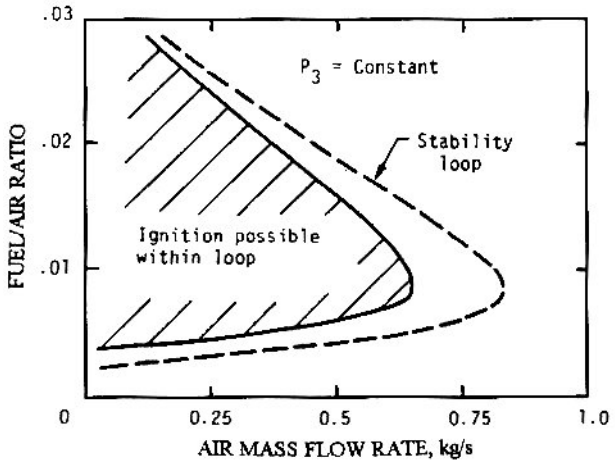

Figure 1.5: Typical gas turbine combustor ignition and stability loops [112]

At high altitudes, sub-atmospheric relight conditions affect ignition capability [46]. In Figure 1.6, the "4 psi" curve represents the window of ignitability for a combustor inlet pressure of 4 psi or 0.28 bars. Depending on windmilling characteristics, this corresponds approximately to an altitude of 35 000 ft or 10.7 km. The "max.mf" curve shows the fuel/air ratio at which ignition can be achieved with maximum air massflow through the combustor for a given inlet pressure.

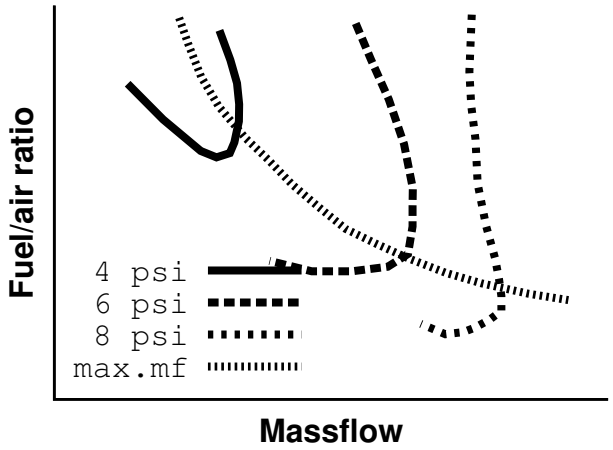

Figure 1.6: Ignitability curve at different sub-atmospheric conditions [46]

For windmilling relight, the maximum speed should not be exceeded in order to prevent flow velocities that are too high within the primary combustion zone. A minimum aircraft speed is required to ensure fuel atomization. Thus, the ignition performance of an aero-engine is commonly expressed as an ignitable operating range, represented as an envelope

in an altitude/Mach number diagram (Figure 1.7).

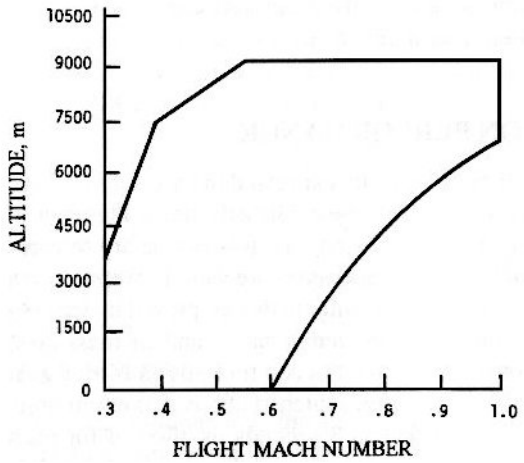

Figure 1.7: Altitude relight limits for a conventional annular combustor [112]

Before entry to service, the altitude relight capability has to be proven by flight tests and certification procedures. However, ignition capability needs to be validated in the development stages of the combustor. Depending on the TRL, more or less extensive tests are carried out. Ignition tests are first performed in single sector combustors at atmospheric conditions, before more expensive high pressure and sub-atmospheric tests are undertaken. The *Component Development Program* on ignition capability is carried out using tests on fully annular rigs, under conditions ranging from sub-atmospheric to high pressure, to validate the final ignition phase "light-around". For further TRL, altitude relight capability and sub-atmospheric combustion efficiency are validated on core engines within the *Engine Development Program* then on flight engines.

1.2.3 Characterization of Ignition Phases in Aero-Engines

According to Lefebvre [112], a significant advance in the understanding of gas turbine ignition was achieved in 1957 when he realized, that at least two distinct phases are involved in the ignition process. The first phase consists of the formation of a kernel of flame induced by energy deposition. The kernel should have sufficient size and temperature to be able to propagate. The second phase is the subsequent flame propagation into the primary zone followed by stabilization. In annular combustion chambers, a third phase, called light-around, consists of the spread of the flame from the ignited sectors to the adjacent ones. The factors influencing these three phases are of prime importance to the design of combustor chambers. They have been identified by Lefebvre and are reported here according to [112].

Factors Influencing Phase 1. Survival of the kernel of hot gas created by the spark depends entirely on whether or not the heat re1ease by combustion within the kernel exceeds the rate of heat loss to the surroundings by radiation and turbulent diffusion. the rate of heat release is governed mainly by the effective fuel/air ratio adjacent to the plug, which should be close to stoichiometric, and by the size and temperature of the kernel, which are, in turn, determined by the energy and duration of the spark. The rate of heat loss from the kernel is largely dictated by the local conditions of velocity and turbulence and by the quantity of excess fuel present in the ignition zone. This phase of the ignition process is also strongly affected by the design of the igniter plug-flush fire or sunken fire, by its location, and by the extent to which the plug tip protrudes through the liner wall.

Factors Influencing Phase 2. The location of the igniter is also important in phase 2 because it determines whether the hot kernel is entrained into the primary-zone reversal or is swept away downstream. This phase is also governed by all the factors that control flame stability. Thus, an increase in pressure and/or temperature, or a reduction in primary-zone velocity, or any change in fuel/air ratio toward the stoichiometric value, all of which are beneficial to stability, will also improve phase 2.

Factors Influencing Phase 3. The location of the interconnector tubes is of prime importance. Ideally, the tube entrance should coincide with the region of highest gas temperature in the liner, whereas the tube exit should be sited so as to ensure that the issuing hot gas flows directly into the recirculation zone of the adjacent liner. Care should be taken to minimize the flow of film-cooling air over the ends of the tube because this could interfere with the flow of hot gas and, more important, seriously reduce its temperature. Phase 3 is aided by the use of interconnectors in which the flow area is made large in order to facilitate the passage of flame, and whose length is kept short to minimize heat loss by external convection to the annulus air.

The object of ignition development is to ensure that stability and ignition limits are separated only by the effects of heat loss [112]. Indeed, the flow properties that control stability also exercise a similar influence on ignition behavior. However, the limits can not be the same since stability limits relate to burning conditions, whereas ignition takes place within cold liner walls and therefore undergoes higher heat loss.

If the ignition performance of a combustor is unsatisfactory, the first step is to find out in which phase the bottleneck is arising [112]. This identification can be achieved in combustor test rigs equipped with high-speed Mie-scattering. At Rolls-Royce, these investigations are conducted in a single sector combustor under atmospheric, high-pressure and sub-atmospheric conditions [46, 110].

Thus, if the encountered difficulties can be attributed to the generation of a sustainable kernel of flame during Phase 1, a reasonable measure would be to double-check the level of atomization near the igniter over a range of operating conditions including the adverse conditions of altitude relight.

Phase 2 is responsible when blow-out events (vigorous flame kernels blowing out of the combustion chamber) are observed while the air mass flowing trough the combustor is low enough that a flame could stabilize in the cold chamber. In such cases, transient flow conditions did not favorably convect well-generated kernels to the primary combustion zone. However, not all sparks necessarily lead to successful ignition. Among all ignition events generated by the spark repetition rate, at least one should undergo favorable generation, convection and propagation conditions so that it can inflame the sector, leading to successful light around. Finally, a criterion for "Phase 2 capability" can be defined as a minimum probability of favorable transient flow conditions.

By analyzing the correlations of experimental data from a large number of conventional aircraft combustion chambers, Lefebvre [111] derived empirical equations for LBO and *lean lightup out* (LLO). The similarity between the expressions for the LBO and LLO values is noticeable and confirms that ignition research should aim to reduce the difference between LBO and LLO to the higher heat loss in the cold chamber. However, the empirical expressions may require revisions to be extended for new combustion concepts.

1.3 Theoretical Background and Literature Review

1.3.1 Knowledge of Ignition Processes

Definitions

Ignition covers a variety of physical phenomena not easily encompassed in a general definition. Mastorakos [118] introduced ignition as follows: "The autoignition (or *spontaneous ignition* or *self-ignition*) and the spark ignition (or *forced ignition* or *assisted ignition*) of a flammable mixture are fundamental problems in combustion science. They deal with the transition from an unreacted (in the case of spark ignition) or slowly reacting (in the case of autoignition) state to a fully or vigorous burning state that corresponds to combustion at high temperature."

An ignition process is defined in this work according to Lefebvre's original observations [112] of the ignition phases in gas turbines: any combustion phenomenon involved in the transition from an initial stationary non-reacting state to a final stationary state that is

reacting in the case of successful ignition or not reacting otherwise. Thus, the definition includes the processes of flame kernel generation, kernel growth, kernel convection, kernel quenching, flame blow-out, flame propagation and flame stabilization. Autoignition in LPP premixing ducts is also considered as an ignition process in this work, although it is a separated issue. Current knowledge of ignition processes is briefly introduced in this section. The physical fundamentals of ignition are presented in more detail in Section 2.3.2. For further information, refer to a recent review: *Ignition of turbulent non-premixed flames* by Mastorakos [118].

Classification

The ignition processes involved in combustion systems can be categorized according to simpler problems, which can be investigated with model burners. Mastorakos [118] presents four canonical turbulent ignition problems: a turbulent jet into oxidizer, a jet-type mixing flow, an opposed jet flow and a volumetric compression. These configurations can implicate gaseous and heterogeneous mixtures of liquid and vapor fuel with gaseous oxidizer. Figure 1.8.a shows the mixing field of turbulent jet into oxidizer, which is characteristic for an autoigniting configuration. Indeed, the mixing with a hot coflow generally results in a most reactive layer ξ_{MR} relatively close to the lean flammability limit ξ_{lean}. For a high coflow velocity $U_{2,0}$, the flow mimics the premixing duct of an LPP gas turbine [118].

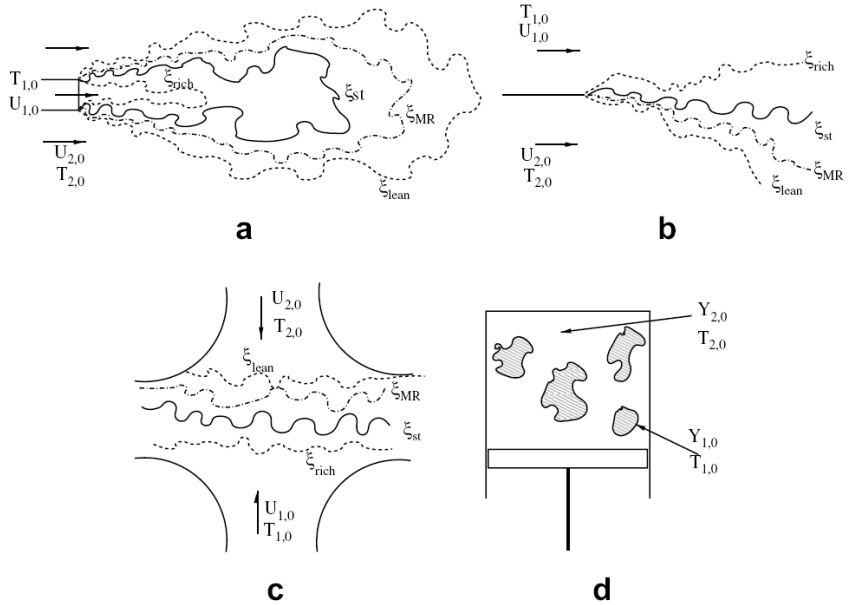

Figure 1.8: Schematics of canonical non-premixed turbulent ignition problems [118]. 1: fuel; 2: oxidizer. a) Turbulent fuel jet in oxidizer coflow, b) spatial mixing layer, c) opposed jet flow and d) volumetric compression.

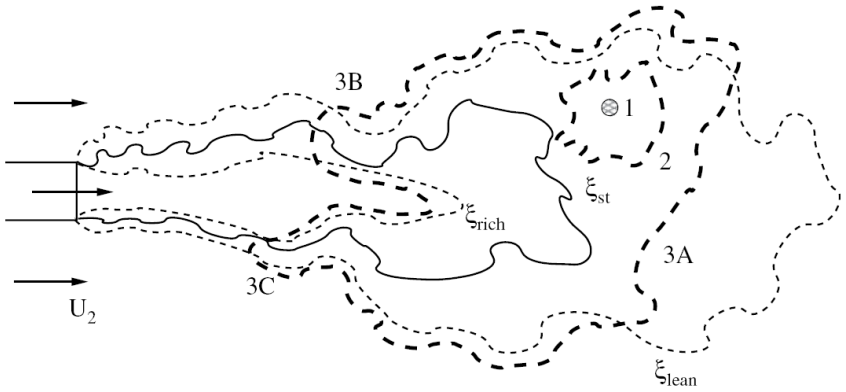

Figure 1.9: Canonical turbulent jet into oxidizer, ignited [118]

If fuel and oxidizer have about the same temperatures, the most reactive layer generally lies close to the stoichiometric isoline ξ_{st} and is not usually represented. Figure 1.9 shows a forced ignited non-premixed turbulent jet. Although a turbulent jet into oxidizer may seem to be a simple problem, the transient evolution following a forced ignition event is governed by different combustion regimes and follows the same canonical ignition processes as in an aero-engine. Indeed, Figure 1.9 displays three ignition phases that are also observed in gas turbines. Line 1 shows a kernel immediately after ignition, line 2, a stratified-charge premixed flame and line 3, three combustion features found in partially-premixed combustion. Portion 3A shows a turbulent stratified-charge premixed flame, portion 3B, an edge flame with low mixture fraction gradient and portion 3C, an edge flame with high mixture fraction gradient. Therefore, the non-premixed turbulent jet is an appropriate model burner to use to investigate ignition processes involved in relight in aero-engines.

Autoignition

Experimental work has been conducted in shock tubes, constant-volume bombs, steady-flow reactors and rapid-compression machines to investigate the basic ignition characteristics of a variety of fuels. A review on the autoignition characteristics of binary methane-hydrocarbons mixtures is given by Spadaccini [157]. Investigation of autoignition of sprays dates from 1949, when Mullins [125] investigated kerosene sprays injected into uniform turbulent hot air. Aggarwal [1] reviewed autoignition of sprays. Only a few experiments explore the effect of turbulence-autoignition interaction. The model burner by Cabra et al. [28], referred to as the *vitiated coflow burner*, and the burner by Markides and Mastorakos [117], referred to as the *Cambridge experiment*, are major references.

Spark Ignition

Due to the practical significance of *spark ignition*, operational experience of combustion engines and aero-engines has been gained. Detailed information on spark ignition can be found in Heywood [76]. Available sources of forced ignition, including spark ignition, torch igniter, glow plug, hot-surface ignition, plasma jet and laser ignition, is given by [112]. Systematic investigation of *minimum ignition energy* (MIE) and *quenching distance* have been conducted by Ballal and Lefebvre and their co-workers [161, 7, 143, 8, 9]. Their findings are fundamental for the understanding of the generation of a sustainable kernel of flame and are further described in Section 2.3.2.

Ahmed et al. investigated spark ignition of gaseous, non-premixed turbulent configurations for different model burners. They provided detailed information on ignition probability and transient behavior of ignited kernels for jets [5], counterflows [4] and recirculating flames [3]. The results for the jets are presented in Section 5.2.

Proper atomization of fuel is of utmost importance for aero-engine relight. Heat losses that sustain fuel evaporation have an impact on flame propagation, whereas local spray properties are critical for flame kernel generation. Spark ignition of sprays is also treated in the review by Aggarwal [1]. Even though numerical investigations have been reported for spray ignition [118], only gaseous mixtures are considered for the development of methods for ignition processes here. Hence, the emphasis in the next section on numerical methods for ignition in gaseous flows.

1.3.2 Numerical Methods for Ignition Processes

The validation procedure for relight capability (Section 1.2.2) illustrates that the development of advanced combustion systems can be an extensive process. Therefore, the design process needs to be guided by a thorough understanding of the ignition processes and supported by experimental validation of the whole process. Predictive methods for auto-ignition processes can also sustain the design process of combustors with high temperature oxidizers, such as the ALSTOM's SEV [21] as well as the design process for the premixing duct in LPP aero-engines. The suite of numerical methods for ignition processes covers a wide-range of complexity, from simple empirical expressions to computationally intensive, three-dimensional transient resolution of reacting technical configurations using Computational Fluid Dynamics (CFD).

Empirical Laws and Asymptotical Analysis

From the investigations of the basic ignition characteristics introduced in previous sections, empirical expressions for ignition delays could be derived, along with chemical kinetic models capable of reproducing ignition delays. Reviews of kinetic modeling have been carried out by Spadaccini [157] for methane fuels, and by Dagaut and Cathonnet [37] for kerosene.

Based on their systematic investigations, Ballal and Lefebvre [8] derived empirical laws for *minimum ignition energy* (MIE) and *quenching distance* for drop size, equivalence ratio, fuel volatility, fuel density and air pressure. These empirical laws were extended to become a general model for spark-ignition for gaseous and liquid fuel-air mixtures in [9]. More recently, Huang et al. [79] performed systematic measurements of MIE in lean turbulent methane-air mixtures, with an equivalence ratio of 0.6 and over a range of turbulence intensities. The authors reported a transition from an almost linear relation between MIE and turbulence intensity to an exponential relation. They concluded the existence of both thin and broken reaction zones regimes, as proposed by Peters [131].

Based on the analytical study of a non-premixed diffusion layer, Liñán [114] demonstrated that the lower turning point of the S-shaped response of flame temperature with the non-dimensional Damköhler number (Section 2.3.4) corresponds to autoignition. Hence, the sudden transition from a "frozen" mixing layer to a burning state can happen when the strain rate is lower than a critical value. This value is lower than the critical strain at extinction, exhibiting an hysteresis phenomenon.

Direct Numerical Simulations of Ignition

Direct Numerical Simulations (DNS) of reacting flows assumes no modeling of the fluid flow. However, combustion needs to be modeled, applying fairly extensive models, such as detailed-chemistry with complex diffusion schemes [77] or *Conditional Moment Closure* (CMC) [119].

To investigate the fundamentals of autoignition, DNS has been applied to homogeneous reactors, one-dimensional mixing layers and to two and three-dimensional configurations. In non-premixed configurations, auto-ignition occurs preferentially at some mixture fractions. This phenomenon can be verified by calculating autoignition delays in quiescent homogeneous reactors, using chemical kinetic models. Performing this over a range of fuel-air mixtures permits the determination of the mixture fraction of the most reactive layer, ξ_{MR}. In the case of a cold fuel jet issuing into a hot oxidizer, the most reactive layer is situated in the lean region (as reported by Cabra et al. [29] for methane) as

found using the 12-step reduced mechanisms developed by Sung et al. [163] and the 325-species, 53-reactions GRI3.0 mechanism from Berkeley University [153]. However, ξ_{MR} is not an intrinsic property of the fuel as it depends on operating conditions [118]. Further insights into the autoignition process of non-premixed configurations can be gained by solving transient mixing layers, as documented for laminar hydrogen-air constant-strain mixing layers [118]. DNS of autoignition of 2-D turbulent non-premixed configurations allowed the investigation of formation of flame kernels and of the "spotty" nature of their localization [119, 77] and [118]. Three-dimensional calculations have been performed to investigate the effects of mixture and turbulence on flame propagation in the context of autoignition [47] and of forced ignition [31, 148, 32, 98].

RANS Simulations

CFD calculations relying on time-averaged transport equations (*Reynolds Averaged Navier Stokes* - RANS) in combination with turbulence models, such as $k-\epsilon$ model [89], and with combustion models, such as equilibrium chemistry, the flamelets approach or conditional moment closure, provide time averaged results for turbulent reacting flows. They permit low cost-intensive parameter variations to optimize combustor configurations and are commonly used in industry. Thus, ignition models have been developed to reproduce the characteristics of spark ignition in combustion engines. In particular, Lagrangian tracers have been integrated into RANS spark ignition models to track the sub-grid motion of the flame kernel surface in [50, 164, 38].

Although autoignition is an unsteady phenomena, turbulent, lifted jet flames controlled by autoignition may exhibit a steady state and can therefore be simulated using RANS methodology. This is the case in the vitiated coflow investigated by Cabra et al. [28] and simulated by Gordon et al. [69] for both hydrogen and methane jets. Using the particle-based *Probability Density Function* (PDF) approach (Pope [140, 141]) with detailed chemistry, Gordon investigated transport budgets of radicals and demonstrated that the stabilization mechanism is due to autoignition. He also reported the build up of a radical pool of precursors, containing minor species such as CH_3, CH_2O, C_2H_2, C_2H_4, C_2H_6, HO_2, and H_2O_2. Michel et al. [122, 123, 124] also investigated this configuration using the *Approximated Diffusion Flame Presumed Conditional Moment* (ADF-PCM) model in combination with a chemistry look-up table based on the calculations of autoigniting homogeneous reactors.

However, the dynamics of ignition processes usually depend on the scales of time-dependent turbulent motion. Thus, methods that are spatially and time-resolved, like *large eddy simulations* (LES), are required.

Large Eddy Simulations

Unsteady and spatially averaged transport equations are solved within LES. According to a defined filter size, the impact of unresolved small turbulent scales is modeled, and large-scale energy-containing eddies are resolved. Since LES are instantaneous simulations, they can capture the impact of more complex flow phenomena, that cannot be satisfactorily treated with RANS or *unsteady RANS* (URANS), such as flame flapping, as described by Poinsot and Veynante [139] (Section 4.5.5). The LES approach is therefore appropriate for the simulation of transient phenomena, such as ignition processes in technical systems. Progress in modeling reacting flows using LES has been reviewed by Janicka and Sadiki [88], Bilger et al. [14] and Pitsch [135]. A recent review on PDF methods for turbulent reacting flows, including LES, was carried out by Haworth [75]. In the context of LES, *Probability Density Function* (PDF) methods are often referred to as *Filtered Density Function* (FDF) methods.

Regarding the simulation of autoignition, several LES of turbulent lifted flames autoigniting in a hot coflow have been reported. The lifted hydrogen flame measured by Cabra et al. [28], has been simulated by Jones et al. [92] and Jones and Navarro-Martinez [91], applying the Eulerian stochastic field method to the joint FDF of the reacting scalars. Using the *Conditional Moment Closure* (CMC) model of Klimenko and Bilger [99], Navarro-Martinez and Kronenburg [126] performed LES of the autoigniting methane configuration, experimentally measured by Cabra et al. [29] as well. The lifted flame has also been investigated using LES, including a *Progress Variable* approach in combination with an investigation of the chemistry of laminar premixed flames and of autoigniting homogeneous reactors by Domingo et al. [48].

LES of forced ignition sequences have been performed in the last two years. Boileau et al. [16] reported an ignition sequence in a gas turbine combustor, using the *Artificially Thickened Flame* (ATF) approach, as introduced by Colin et al. [35] for performing LES of turbulent premixed combustion. Spark ignition of a turbulent methane jet, experimentally investigated by Ahmed and Mastorakos [5], has also been simulated using LES by Lacaze et al. [105], applying the ATF model for combustion. LES of spark ignition of the bluff-body configuration, experimentally investigated by Ahmed et al. [3], has been reported by Triantafyllidis et al. [168] using CMC, while Subramanian et al. [162] applied a tabulated-chemistry method based on the PCM-FPI model. Vermorel et al. [172] performed LES of combustion cycles in spark ignited combustion engines, using the *Arc and Kernel Tracking Ignition Model* (AKTIM) introduced by Duclos and Colin [50], coupled with an extended, coherent flame model for the subsequent combustion. From these studies, it is recognized that the time-resolved calculation of an ignition sequence, as simulated

in [16, 105, 168, 162, 172], requires manycomputational resources, to the extent that the exploitation of time-resolved events is excluded when performing statistical analysis, such as when predicting the experimentally-observable ignition probability.

1.4 Scope

As outlined in Section 1.2.1, low-emission combustion research concepts highlight the importance of mastering ignition processes. Aero-engine designers demand predictive methods to develop combustors with advanced altitude relight capability. More generally, the development towards less stabile, lean-burn combustion concepts increases the probability of unsteady effects occuring. The unsteady phenomena within an aero-engine involve complex physical coupling effects between engine components.

The joint proposal "*Unsteady System Modeling of Aircraft Engines*" ("*Instationäre Systemmodellierung von Flugtriebwerken*") [44] by TU Darmstadt and Rolls-Royce Deutschland in 2006 to the *German Research Foundation* (DFG: *Deutsche Forschungsgemeinschaft*) has been granted funding. As a result, the Graduate School GRK1344 (*Graduiertenkolleg* 1344) was created and aims to improve the prediction and control of these unsteady effects.

Lean-burn combustion concepts imply complex air-fuel mixing and therefore complex combustor geometries, which are laborious to mesh with multiblocking structures. For this reason, it has been decided within Rolls-Royce to develop an in-house CFD code working with unstructured meshes. It is called *PRECISE-UNS* (*Predictive-System for Real Engine Combustors - Unstructured*), in analogy to the established in-house code for multiblocking meshes *PRECISE-MB* (*Predictive-System for Real Engine Combustors - MultiBlocking*). The new code is built on *Dolfyn*, an open-source code based on finite volumes and written in Fortran90. The code can be downloaded from the website: `www.dolfyn.net`. All CFD calculations in this work have been carried out using PRECISE-UNS.

1.4.1 Objective

As described in Section 1.2.3, a combustor is considered as having advanced altitude relight capability, when the difference between the limits for ignition blow-out and weak extinction can be reduced to the effects of higher heat loss due to the low temperature of the liner wall. To achieve this, the minimum probability of favorable transient flow conditions for ignition must be ensured over a range of operating conditions.

The general goal of this work is to develop numerical methods for the prediction of altitude relight capability in current and next generation aero-engines. Within the long-term DFG Graduate School funding, the ultimate goal is evaluating the probability of transient flow conditions favorable for the generation, convection and propagation of an ignited kernel to the primary combustion zone.

Ignition events are intrinsically unsteady phenomena, characterized by slow chemistry effects in interaction with the turbulent flow field. Their statistical analyses require averaging over data sets. However, ensemble averaging is particularly difficult for time-resolved calculations with high ranges of time scales. Even the generation of experimental data for such phenomena can be difficult, if the events cannot be repeated at satisfying rates, for example, because of required time for cooling for example. Hence, only a few detailed investigations of the statistics of ignition events have been conducted, such as Ahmed and Mastorakos [5] and Ahmed et al. [4, 3].

LES is particularly appropriate for simulating unsteady phenomena and has been successfully applied to the simulation of spark ignition events in [16, 105, 168, 162, 172]. Nonetheless, the probabilistic nature of spark ignition events is mainly determined by turbulent flow conditions at ignition time, such as local velocity and local mixture fraction. Richardson [147] proposed a statistical analysis method of the ignitability of a combustor without directly modeling the turbulent combustion. The work here focuses especially on developing methods for statistical analysis of ignition processes, based on LES and including the joint effects of local flow conditions at spark location and flame kernel transport and transition to an established flame.

1.4.2 Outline

This introductory chapter provides a general description of the current issues in combustion, such as fossil fuel energy utilization, environmental concerns, emissions regulations and requirements for aero-engines. The technical issues associated with ignition phenomena, such as the design of effective and low-emissions combustion systems in general and for aero-engines specifically, are introduced. In Section 1.3, the state of the art regarding the knowledge and numerical modeling of ignition processes is reviewed. The objective of the thesis and the outline are also defined here.

Chapter 2 provides an introduction to the theory of combustion physics. Section 2.1 presents the governing principles of fluid flow, along with the fundamental relations. A brief description of turbulence is provided in Section 2.2. The fundamentals of combus-

tion theory, including chemical reaction kinetics, auto- and forced ignition principles and different combustion regimes are introduced with more detail in Section 2.3.

The modeling approaches for turbulent reactive flows are examined in Chapter 3. Section 3.1 presents the three principal modeling levels when simulating turbulent flows: (i) *Direct Numerical Simulation*, (ii) *Reynolds-Averaged Navier-Stokes Simulation*, and (iii) *Large Eddy Simulation*. The corresponding averaged or filtered governing equations for turbulent flows and scalar mixing are given as well. Section 3.2 gives an introduction into the modeling of combustion. The *Flamelet Generated Manifolds* model, the chemical reaction mechanism involved in the autoignition of methane and the modeling of ignition kinetics are presented in some detail. The modeling of turbulence chemistry interaction is examined in Section 3.3.

Chapter 4 is devoted to numerical treatment within the flow solver. Section 4.1 introduces the CFD code. Sections 4.2, 4.3 and 4.4 present the approaches applied for discretization in space, for advancing in time and for coupling pressure and velocity fields, respectively. Section 4.5 describes the numerical treatment applied for modeling autoignition.

Chapter 5 is dedicated to documentation of the applications investigated within this work. Section 5.1 presents the results of the investigation of the stabilization mechanism of a turbulent methane-air jet flame autoigniting in a hot coflow. Section 5.2 presents the investigations of a spark ignited methane-air jet, consisting of statistical analysis and the simulation of characteristic ignition events.

Finally, Chapter 6 is a summary of the results, the conclusion and the outlook for future research.

2 Combustion Physics

This chapter provides a basis for understanding the physics involved in turbulent reacting flows, including ignition processes. The principles of fluid flow and species transport are presented first. Following this, the basic concepts used for describing turbulent flows are introduced. The third section provides a short overview on the fundamentals of chemical reaction kinetics and ignition, as well as the regimes of turbulent combustion.

2.1 Fluid Flow

The governing principles of flow dynamics refer to the conservation of mass and momentum. They are expressed as a set of coupled balance equations, which are commonly defined locally and appear in a differential form. Hence, the local description of mass conservation, expressed from an Eulerian point of view, relates the volumetric accumulation rate of mass to the divergence of the mass flux within an infinitesimal volume, or in a localized formula (Eq. 2.1), the density rate of change to the mass flux gradient.

$$\frac{\partial \rho}{\partial t} + \frac{\partial (\rho u_i)}{\partial x_i} = 0 \tag{2.1}$$

Starting from the left hand side, the equation of momentum conservation (Eq. 2.2) consists of the temporal change, the convective transport and the effects of forces resulting from shear, pressure and gravitation. In the following equations, the effect of gravitation is neglected.

$$\frac{\partial (\rho u_i)}{\partial t} + \frac{\partial (\rho u_i u_j)}{\partial x_i} = \frac{\partial \tau_{ij}}{\partial x_i} - \frac{\partial p}{\partial x_i} + \rho g_i \tag{2.2}$$

In Newtonian fluids, the shear stresses are proportionally related to the velocity gradients through the dynamic viscosity, μ. Hence, the stress tensor can be reduced to its deviatoric part

$$\tau_{ij} = \mu \left(\frac{\partial u_j}{\partial x_i} + \frac{\partial u_i}{\partial x_j} - \frac{2}{3} \frac{\partial u_k}{\partial x_k} \delta_{ij} \right). \tag{2.3}$$

Substituting the dynamic viscosity, μ, with the kinematic viscosity, $\nu = \mu/\rho$, and Eq. 2.3 into Eq. 2.2, the *Navier-Stokes Equations* for Newtonian fluids are obtained:

$$\frac{\partial(\rho u_i)}{\partial t} + \frac{\partial(\rho u_i u_j)}{\partial x_i} = \frac{\partial}{\partial x_i}\left[\rho\nu\left(\frac{\partial u_j}{\partial x_i} + \frac{\partial u_i}{\partial x_j}\right) - \frac{2}{3}\rho\nu\frac{\partial u_k}{\partial x_k}\delta_{ij}\right] - \frac{\partial p}{\partial x_i} \tag{2.4}$$

Navier-Stokes equations in conjunction with the continuity equation fully describe the flow of an incompressible Newtonian fluid. For low Mach numbers flows, the enthalpy balance equation is not necessarily required.

Similar to the previous balance equations, the transport of a conserved scalar, ϕ, such as a species mass fraction, can be described by a general transport equation as:

$$\frac{\partial(\rho\phi)}{\partial t} + \frac{\partial\left(\rho\phi u_i\right)}{\partial x_i} = \frac{\partial}{\partial x_i}\left(\rho D_\phi \frac{\partial\phi}{\partial x_i}\right) + \dot{\omega_\phi}. \tag{2.5}$$

Diffusive fluxes appear on the right hand side of Eq. 2.5, with the diffusion coefficient D_ϕ, according to Fick's law, as well as the change of ϕ due to net volumetric sources, $\dot{\omega_\phi}$. In a system of multiple species, different species' diffusion coefficients result in differential diffusion. Hence, binary diffusion coefficients have to be determined if the effects of differential diffusion are to be considered.

The balance equations for mass (Eq. 2.1), momentum (Eq. 2.2) and scalar transport (Eq. 2.5) allow the description of the mixing of non-reacting flows. As chemical reactions within a flame front are coupled through heat exchange, a transport equation for enthalpy, h, is needed for resolving the combustion chemistry. Neglecting compressibility effects (low-Mach number flow), radiation, energy dissipation, and assuming unity Lewis number and constant Prandtl number, the balance equation for enthalpy corresponds to the transport equation of a conserved scalar, where the right hand side term refers to heat diffusion.

$$\frac{\partial(\rho h)}{\partial t} + \frac{\partial\left(\rho h u_i\right)}{\partial x_i} = \frac{\partial}{\partial x_i}\left(\frac{\lambda}{c_p}\frac{\partial h}{\partial x_i}\right) \tag{2.6}$$

2.2 Turbulence

Turbulent flows are *unsteady, three-dimensional, apparently random, multi-scale and dissipative.* They differ from laminar flows, where viscous forces dominate. Rewriting the Navier-Stokes equations (Eq. 2.4) in a non-dimensional form lets a dimensionless number appear.

$$Re = \frac{\rho U_0^2}{\rho\nu U_0/l_0} = \frac{U_0 l_0}{\nu} \tag{2.7}$$

The Reynolds number, Re, corresponds to the ratio of inertial forces, ρU_0^2, to viscous forces, $\frac{\rho \nu U_o}{l_0}$. Hence, this number quantifies the relative importance of the stabilizing viscous forces and the non-linear inertial forces and distinguishes between laminar (low Re) and turbulent (high Re) flows.

Large vortices are generated by the shear of the mean flow [10]. These vortices, also called eddies or structures, interact with each other and break up into smaller eddies. Thus, energy is transferred from the larger structures to the smaller structures and is then dissipated by the smallest eddies. This phenomenon, referred to as *energy cascade*, is a fundamental part of Kolmogorov's theory of isotropic turbulence [101] (Figure 2.1). At a given length scale r, the energy dissipation rate $\varepsilon(r)$, Eq. 2.8, is estimated as the

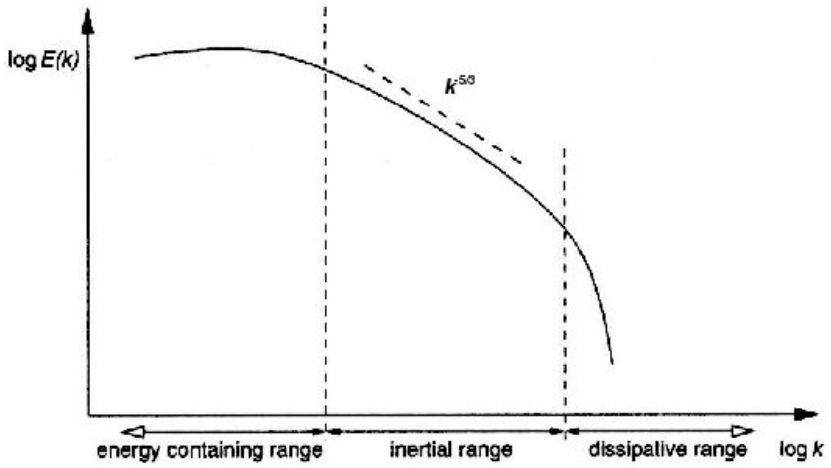

Figure 2.1: Sketch of a turbulent energy spectrum. (Reproduced from [93])

ratio of the turbulent kinetic energy $u'^2(r)$ and the time scale $r/u'(r)$. It is found to be constant in the inertial range, where the turbulent Reynolds number, $Re_t(r) = u'(r)r/\nu$ is high.

$$\varepsilon(r) = \frac{u'^2(r)}{r/u'(r)} = \frac{u'^3}{r} \tag{2.8}$$

At the smallest scale, called the *Kolmogorov length scale*, η_k, the viscous forces balance with the inertial forces. Hence, the Kolmogorov length scale can be defined from the *kinematic viscosity* ν and the *kinetic energy dissipation rate* ε.

$$\eta_k = \left[\frac{\nu^3}{\varepsilon}\right]^{\frac{1}{4}} \tag{2.9}$$

The integral length scale, l_t, can be mathematically defined using the normalized spatial autocorrelation function, $R_{u_i u_j}(r, x)$, of velocity at a point x in direction r:

$$R_{u_i u_j}(r, x) = \frac{< u_i'(x) u_j'(x + r) >}{\sqrt{< u_i'(x)^2 >< u_j'(x + r)^2 >}}, \tag{2.10}$$

$$l_t(x) = \int_0^\infty R_{uu}(r, x) dr. \tag{2.11}$$

As the integral length scale carries the bulk of the turbulent energy, the kinetic energy dissipated in the dissipative range of small eddies displayed on the *energy cascade* sketch (Figure 2.1), can be estimated as:

$$\varepsilon \approx \frac{u'^3}{l_t}. \tag{2.12}$$

Finally, the ratio between the largest and the smallest scales is dependent on the *turbulent Reynolds number*, $Re_t = u' l_t / \nu$ as:

$$\frac{l_t}{\eta_k} \approx Re_t^{3/4}. \tag{2.13}$$

2.3 Combustion

This section provides an introduction to the combustion theory relevant to this work. Chemical reaction generalities are first introduced. The classical distinction between premixed and non-premixed flames is presented. For more detailed information, refer to [185], [131] or [175].

2.3.1 Chemical Reaction Kinetics

Globally, combustion is the exothermic conversion of fuel and oxidizer into reaction products. Considering the combustion of methane (CH_4) in air, the reaction can be written in a global form as:

$$CH_4 + 2O_2 \Longrightarrow CO_2 + 2H_2O. \tag{2.14}$$

This global formulation represents the ideal conversion of all reactants into products without considering time. Thus, only the fuel CH_4, the oxygen of the air (O_2) and the products, carbon dioxide (CO_2) and water (H_2O) appear, while nitrogen (N_2) and minor species are not mentioned. In reality, the chemical pathway is more complex and minor species are formed, such as OH and CO. The global reaction provides the global stoichiometric coefficients of reactants and products, denoted ν_*' and ν_*'', for the respective

species.

$$\nu'_{CH_4} = 1, \quad \nu'_{O_2} = 2, \quad \nu''_{CO_2} = 1 \quad and \quad \nu''_{H_2O} = 2. \tag{2.15}$$

The global reaction equation can be written in a general form for the complete reaction of a hydrocarbon fuel, C_mH_n, as:

$$\nu'_F C_n H_m + \nu'_{O_2} O_2 \Longrightarrow \nu''_{CO_2} CO_2 + \nu''_{H_2O} H_2O. \tag{2.16}$$

In this formulation the stoichiometric coefficients of fuel and oxygen are related as $(m + n/4)\nu'_F = \nu'_{O_2}$. The changes of mass fractions of oxygen, dY_{O_2}, and fuel, dY_F, are related to each other in Eq. 2.17, where the M_* denote the molecular weights of the respective species.

$$\frac{dY_{O_2}}{\nu'_{O_2} M_{O_2}} = \frac{dY_F}{\nu'_F M_F} \tag{2.17}$$

Introducing the stoichiometric oxygen-to-fuel mass ratio, $\nu = \nu'_{O_2} M_{O_2} / \nu'_F M_F$, and the integrating equation (Eq. 2.17) for a homogeneous mixture in unburnt initial conditions, subscript u, lead to:

$$\nu Y_F - O_2 = \nu Y_{F,u} - Y_{O_2,u}. \tag{2.18}$$

In a stoichiometric mixture, fuel and oxygen are entirely consumed after ideal combustion. Hence, the stoichiometric mixing can be expressed for mass fraction as:

$$\left(\frac{Y_{O_2,u}}{Y_{F,u}} \right)_{st} = \nu. \tag{2.19}$$

The equivalence ratio, ϕ, is defined as the normalized *Fuel-to-Air Ratio* in the unburnt mixture, $FAR = Y_{O_2,u}/Y_{F,u}$, as:

$$\phi = \frac{FAR}{FAR_{st}} = \frac{Y_{F,u}/Y_{air}}{(Y_{F,u}/Y_{air})_{st}}. \tag{2.20}$$

To investigate reaction kinetics, decomposition into a set of elementary reactions is needed. The following equation represents the j-th reaction in a system of N species:

$$\sum_{k=1}^{N} \nu'_{k,R_j} \varphi_k \rightleftharpoons \sum_{k=1}^{N} \nu''_{k,R_j} \varphi_k. \tag{2.21}$$

In this equation, index k refers to the k-th species. The molar stoichiometric coefficients of the reactants and products are represented by ν'_{k,R_j} and $\nu''_{k,R}$. In order to simulate the combustion of a flame, the transport equation, Eq. 2.5, needs to be solved for all species mass fractions, x_*, as well as for the corresponding chemical source term, $\dot{\omega_{x_*}}$.

The chemical source term of the k-th species is the sum of the differences between the production and the consumption rates in all N_R reactions. Hence, for the forward and backward reaction rates, r_{f,R_j} and r_{b,R_j}, the chemical source term reads:

$$\dot{\omega_{x_k}} = \sum_{j=1}^{N_R} \left(\nu''_{k,R_j} - \nu'_{k,R_j}\right) \left(r_{f,R_j} - r_{b,R_j}\right). \tag{2.22}$$

The forward and backward reaction rates of the elementary reactions, Eq. 2.21, are proportional to the product of the concentrations of the respective reacting species, raised to the power of the corresponding stoichiometric coefficient.

$$r_{f,R_j} = k_{f,R_j} \prod_{k=1}^{N} \left(\frac{\rho x_k}{M_k}\right)^{\nu'_{k,R_j}}, \qquad r_{b,R_j} = k_{b,R_j} \prod_{k=1}^{N} \left(\frac{\rho x_k}{M_k}\right)^{\nu''_{k,R_j}}. \tag{2.23}$$

The rate-coefficients, $k_{b,R}$ and $k_{f,R}$, are approximated by an exponential equation, the Arrhenius-law:

$$k_{i,R} \approx A_{i,R} exp\left(-\frac{E_{a,i,R_j}}{RT}\right), \tag{2.24}$$

where i represents the backward b or forward f direction, the pre-exponential coefficient A_{i,R_j} a reaction rate constant, E_{a,i,R_j} the activation energy, R the universal gas constant and T the temperature.

Finally, the set of equations for the elementary reactions, Eq. 2.21, together with the balance equations for mass (Eq. 2.1), momentum (Eq. 2.2), species transport (Eq. 2.5) and enthalpy (Eq. 2.6) allows a description of the mixing of non-reacting flows. Despite the wide range of chemistry time scales involved in chemical reactions, chemistry codes such as *Chem1D* developed at the *Eindhoven University of Technology* [33] allow to resolve the species concentrations within laminar flames. Therefore, chemical kinetics mechanisms, such as the GRI3.0 mechanism for methane from Berkeley University with 325 species and 53 reactions [153], provide all species and reactions coefficients. However, the resolution of detailed chemistry is beyond the scope of engineering applications, since wide ranges of length scales dramatically increase the stiffness of the set of equations. Therefore, combustion modeling must be considered (Section 3.2).

2.3.2 Ignition Fundamentals

Autoignition

Gaseous mixtures and heterogeneous mixtures with liquid fuel can encounter spontaneous and forced ignition. In fuel-air mixtures at temperatures in the order of 750 K

and higher, chain branching reactions can accelerate the generation of radicals and heat and subsequently lead to the thermal runaway called autoignition. In an adiabatic homogeneous system and a simple Arrhenius approach, it can be shown that this thermal explosion process follows an exponential course [108]. The time span between the process initiation and the thermal runaway is the ignition delay time. It is a fundamental quantity of the autoignition process and which depends on temperature and pressure conditions, and the kinetic properties of the reaction process.

The basic characteristics of autoignition have been investigated in shock tubes, constant-volume bombs, steady-flow reactors and rapid-compression machines. Based on extensive investigations under controlled conditions, empirical correlations for ignition delays could be derived for a variety of fuels. In addition, detailed chemistry mechanisms capable of reproducing delay time could be derived. A review on the ignition characteristics of binary methane-hydrocarbons mixtures is given by Spadaccini [157].

Ignition delay generally decreases with increasing temperature. While this dependency is monotonous for lower hydrocarbons such as hydrogen (H_2) and methane (CH_4), more complex reaction paths including *degenerated chain branching* exist for higher hydrocarbons. Consequently, *negative temperature coefficients* are observed at intermediate temperatures (for example, Gallagher et al. [64]). Due to the complexity of the chemical reaction schemes of higher hydrocarbons the existing kinetic models may require further improvements, as noted by Dagaut and Cathonnet [37] in their review of kerosene. In addition, the effect of higher hydrocarbons on methane-based fuel chemistry requires further investigations, since fuel-flexibility is required for stationary gas turbines (for example, Bourque et al. [19]).

The autoignition of methane is presented in Section 3.2.4 to illustrate the autoignition of hydrocarbons and for introducing the modeling of chemical kinetics.

Forced Ignition

For a given fuel-air mixture, the conditions of pressure and temperature where the autoignition can occur are defined by an explosion limit. At temperatures below the explosion limit, autoignition is chemically inhibited. Below this temperature, ignition can be induced by an energy source that introduces a small volume of mixture at higher temperature [175]. Autoignition takes place within this volume and the subsequent kernel of flame may propagate into the unburnt mixture. This limit is also called the *autoignition temperature*. It is a useful practical device to rank the ease by which various compounds

autoignite, but cannot help the understanding of the details of the autoignition process and how this is affected by the flow.

The course of ignition is governed by an interplay between heat release rate and heat loss rate. In order to generate a kernel of flame that is able to propagate, the volume of mixture needs to be heated to a sufficiently high temperature. Thus, a minimum ignition energy density is required. The energy needed is proportional to the pressure and to the deposition volume, but is almost independent of the spark duration for short ignition times. Furthermore, the turbulent fluid time scales are small compared to the ignition delay, so that the effect of convective and diffusive species transport can not be neglected. Indeed, a small ignited volume can be quenched by turbulent mixing before enough heat is released by the reaction. Hence a minimum discharge radius corresponding to a *quenching distance* is required. Finally, this *quenching distance* and the subsequent *minimum ignition energy* increase with the turbulent intensity and with increasing lean and rich conditions, as found by Ballal and Lefebvre [7].

2.3.3 Non-Premixed Combustion

Non-premixed flames are found in technical applications, where fuel and oxidizer are not mixed before entering the combustion zone. They are also referred to as *diffusion flames*, since fuel and oxidizer have to be mixed on a molecular level through diffusion, before they can react with each other. As the chemical reaction is generally faster than molecular mixing, the rate of reaction is determined by mixing and the chemical state essentially depends on the mixture fraction. Non-premixed combustion occurs only in limited regions where the reactants are adequately mixed. It is commonly preferred for safety reasons. Typical industrial applications where diffusion flames are found are diesel engines and aero-engines with conventional combustors. Schematics of canonical non-premixed configurations are displayed in Figure 1.8.

Non-premixed flames are controlled by mixing processes that involve complex phenomena that are demanding to resolve numerically. However, the complexity of the resolution of the mixing can be reduced significantly by applying the Shvab-Zeldovich formalism [185] and the subsequent mixture fraction approach. The formalism requires that the Dufour and Soret effects, the diffusion due to pressure gradients and external forces, the radiative heat transfer and differential diffusion (common diffusivity D for all species) are all neglected. The ratios of heat- to mass-diffusion, called Lewis number, are considered as a unity for all species i, Eq. 2.25. Pressure is also assumed to be constant (low Mach

number assumption).

$$Le_i = \frac{\lambda}{\rho D_i c_p} = 1 \tag{2.25}$$

In the scope of the Shvab-Zeldovich formalism, the system of equations for species transport, Eq. 2.5, and enthalpy, Eq. 2.6, can be reduced to a single transport equation of the mixture fraction, f, Eq. 2.26:

$$\frac{\partial(\rho f)}{\partial t} + \frac{\partial\left(\rho f u_i\right)}{\partial x_i} = \frac{\partial}{\partial x_i}\left(\rho D_f \frac{\partial f}{\partial x_i}\right). \tag{2.26}$$

Within the calculations performed, the diffusion coefficient of the mixture fraction, D_f, is calculated using a constant laminar *Schmidt number*, $Sc = \nu/D_f = 0.7$.

In most non-premixed flames, a stream of fuel (f_u) is mixed with a stream of oxidizer (ox). The mixture fraction is defined as the local ratio of mass flux originating from the fuel feed to the sum of both mass fluxes [131].

$$f = \frac{\dot{m_{fu}}}{\dot{m_{fu}} + \dot{m_{ox}}} \tag{2.27}$$

The mass fraction of the oxidizer corresponds then to $1 - f$. The mass fractions of fuel and oxygen in the unburnt mixture read:

$$Y_{F,u} = f\ Y_{F,fu} \quad , \qquad Y_{O_2,u} = (1-f)\ Y_{O_2,ox}, \tag{2.28}$$

where $Y_{F,u}$ and $Y_{O_2,ox}$ denote the mass fraction of fuel and oxygen in the respective fuel and oxidizer streams. They both account for inerts, such as nitrogen contained in air, and in which the value of the oxygen mass fraction is: $Y_{O_2,air} = 0.232$.

In the stoichiometric coefficients defined in the global reaction, Eq. 2.16, the value of the stoichiometric mixture fraction, f_{st}, can be calculated. For instance, the value of the stoichiometric methane-air mixture fraction is: $f_{st} = 0.055$. An analytical relation between mixture fraction and equivalence ratio can be derived.

$$\phi = \frac{f}{1-f}\ \frac{1-f_{st}}{f_{st}} \tag{2.29}$$

Assuming the hypotheses defined by Shvab and Zeldovich, non-premixed combustion is modeled using balance equations for mass, Eq. 2.1, momentum, Eq. 2.2, and mixture fraction, Eq. 2.26. While thermo-chemistry can be directly obtained from the mixture fraction in the limit of infinitely fast chemistry, "*mixed is burned*" or derived from one or

several progress variables.

2.3.4 Premixed Combustion

In premixed combustion, fuel and oxidizer are mixed on a molecular level prior to chemical reaction. Although this work focuses on non-premixed configurations, forced ignition is preferably initiated in a zone of flammable mixture, where the level of premixedness between fuel and oxidizer may be high enough to ascribe the growth of the flame kernel to premixed combustion. In technical applications premixed flames are essentially turbulent and result in clean and intense combustion in comparison to diffusion flames. Nonetheless, premixed combustion is more subject to instabilities. In particular, acoustic waves induce variations in the local heat release, which may feed back. Flame flashback into the nozzle or autoignition in the premixing unit can seriously affect the integrity of premixed combustion systems.

The principles of laminar and turbulent flames propagation are shown in Figure 2.2, where wall friction and heat exchange are neglected. Turbulent structures are displayed as wrinkling the flame front. The laminar flame speed, s_L, is defined as pointing towards the unburnt mixture as:

$$s_L = \dot{m}/\rho_u, \tag{2.30}$$

where $\dot{m}$ represents the consumption rate along the flame front and ρ_u the density of the fresh gas. The velocity of the burnt gas behind the flame front is obtained from mass conservation law: $(\rho_u/\rho_b)s_L$.

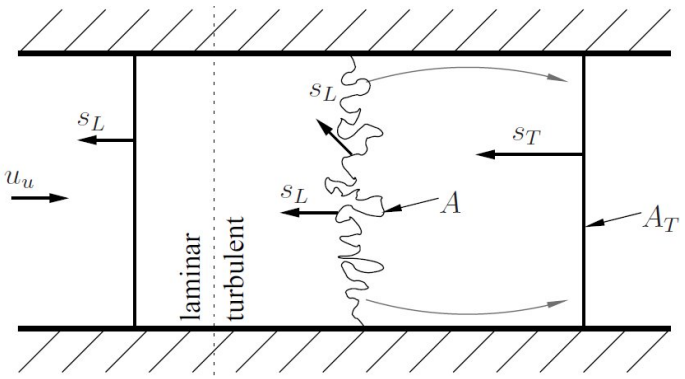

Figure 2.2: Principles of laminar and turbulent flames propagation speed, s_L and s_T respectively. (Reproduced from [62])

In premixed flames, the local reaction rates are essentially controlled by the balance between heat release, due to the exothermic reaction, and thermal diffusion within the

flame reacting zone. Subsequently, three regions are distinguished in premixed flames: a preheat zone, the inner reaction zone and an oxidation zone. Figure 2.3 shows the structure of a one-dimensional, laminar, methane-air premixed flame. In the preheat zone,

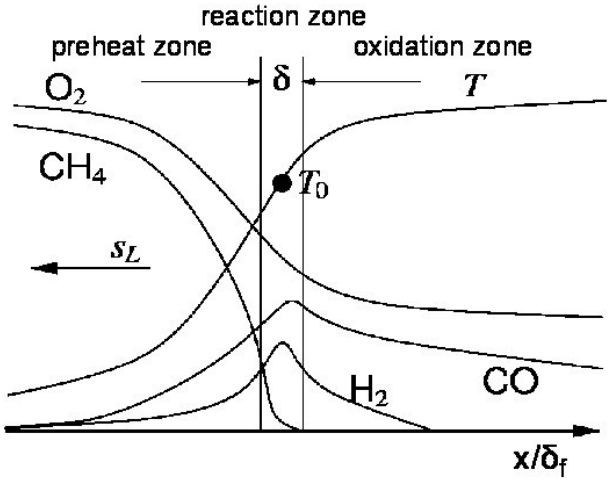

Figure 2.3: Structure of one-dimensional laminar methane-air premixed flame [131].

heat is transferred from the inner reaction zone to the fresh gas by thermal diffusion. Most of the reaction heat is released within the inner reaction zone, which is about 10 times smaller than the flame thickness, $\delta = 0.1$. The flame temperature, T_0, corresponds to the temperature at the maximal fuel consumption rate, while the highest temperature is obtained at the end of the post-flame zone, where radicals are recombined. Under adiabatic conditions, the radicals corresponds to the adiabatic flame temperature. Göttgens et al. [72] introduced a definition of the flame thickness, δ_f, based on scaling laws as:

$$\delta_f = \frac{D_{th,u}}{s_L} = \frac{\lambda_u}{\rho_u c_p s_L}, \tag{2.31}$$

where all quantities are evaluated in the fresh gas, subscript u. Poinsot and Veynante [139] proposed a definition based on the maximal temperature gradient that presents a practical interest for numerical simulations.

$$\delta_f = \frac{T_b - T_u}{max|\frac{\partial T}{\partial x}|} \tag{2.32}$$

Turbulent flame speed has been the focus of numerous experiments, and was reviewed by Bradley [20]. At low turbulence levels, the turbulent flame speed is found to increase almost linearly with the turbulence intensity, whereas this effect is reduced at higher levels. At even higher turbulence levels, broken reaction zones and quenching are observed.

The impact of turbulence on premixed combustion has been investigated by Damköhler [39], who first proposed the existence of different turbulent combustion regimes. Several diagrams propose a definition of the regimes of premixed combustion [131]. Figure 2.4 show the regime classification in terms of the turbulent velocity to laminar flame speed ratio u'/s_L and integral length scale to flame thickness ratio l_t/δ_f. Two non-dimensional numbers are used to classify these regimes (Figure 2.4). The Damköhler number, Da, relates the turbulent time scale, τ_t, to the chemical time scale, τ_C, as:

$$Da = \tau_t/\tau_C = \delta_f s_L/u' l_t. \tag{2.33}$$

While the Karlowitz Number, Ka, compares the chemical time scale, τ_C, to the Kolmogorov time scale, τ_K.

$$Ka = \tau_C/\tau_K = (\delta_f/\eta_K)^2. \tag{2.34}$$

Both numbers are related to the turbulent Reynolds number, Re_t, as:

$$Re_t = \frac{u' l_t}{\nu} = Da^2 Ka^2. \tag{2.35}$$

The region of laminar flames is delineated by the line of unity turbulent Reynolds number:

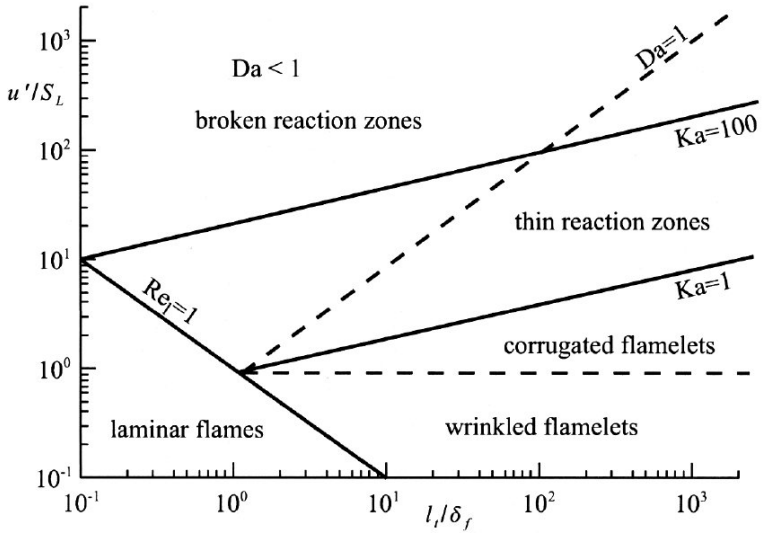

Figure 2.4: Regime diagram for turbulent premixed combustion [18, 131]. (Reproduced from [160])

$Re_t = 1$. The *well-stirred reactor* regime is defined by a mixing time shorter than reaction time, $\tau_t < \tau_C$, $Da < 1$. This regime is not of technical relevance, nor is the regime of wrinkled flamelets that are found in low turbulence intensity, $u' < s_L$. The Klimov-Williams criterion, $Ka = 1$, separates the corrugated flamelets from the thin reaction zones. In the regime of corrugated flamelets, the smallest turbulent scales are bigger

than the flame thickness, and are subsequently not able to affect the flame structure. The regime of $1 < Ka < 100$ is referred to as the regime of *thin reaction zones* [131] or of *thickened wrinkled flames* [139]. Kolmogorov eddies are able to interact with the preheat zone. However, in this regime the inner reaction layer is not disturbed by turbulent motion. In contrast, eddies ten times smaller than the flame thickness, $\delta_f/\eta_K > 10$, $Ka > 100$, are able to disrupt the inner reaction layer, resulting in *broken reaction zones*.

From experimental measurements of the turbulent flame speed, s_T, Damköhler [39] suggested that turbulence increases the reaction consumption rate, in the same proportion to the flame surface area. He proposed a scaling law:

$$s_T = s_L \frac{A}{A_T}. \tag{2.36}$$

Figure 2.2 illustrates this formula, where A denotes the laminar flame front area propagating at laminar flame speed and A_T represents the area of the flame surface projected orthogonally to the direction of flame propagation. The turbulent flame front area, A_T, is moving at the turbulent flame speed s_T. Damköhler [39] estimated the effect of turbulence on the increase of flame surface area as:

$$A = A_T \frac{u'}{s_L}. \tag{2.37}$$

Hence, the turbulent flame speed can be derived from the laminar flame speed and the turbulent velocity accordingly:

$$s_T = s_L \frac{u'}{s_L}. \tag{2.38}$$

Further models have been proposed for modeling the turbulent velocity within RANS and LES simulations, as reviewed by Düsing [51]. The majority of these models can be generalized as:

$$s_T = s_L \left(1 + C \left(\frac{u'}{s_L}\right)\right)^n. \tag{2.39}$$

2.3.5 Partially Premixed Combustion

In technical systems the two idealized combustion regimes presented in the last sections are not usually found in a pure form. The various hybrid regimes of premixed and non-premixed combustion are acknowledged as partially premixed combustion. In premixed applications, mixture stratification effects are commonly found. These effects might even be wanted for controlling the combustion in some applications, particularly in homogeneous charge compression ignition engines. In configurations where fuel and oxidizer are

introduced separately, purely non-premixed combustion may occur, for instance when a diffusion flame is attached to a nozzle. However, lifted flames are frequently obtained, when the fuel velocity exceeds a certain level. In this case, which is relevant to gas turbines, partial premixing occurs prior to combustion and results in a flammable mixture that is lean on the oxidizer side and rich on the fuel side. Figure 2.5 displays the sketch of a so-called *triple flame*, which is characteristic of partially premixed combustion. Two branches of lean-stratified and rich-stratified premixed combustion are represented, while the excess oxidizer from the lean side and the excess fuel from the rich side react in a diffusion flame. A single trailing diffusion flame, referred to as the *edge flame*, may also be observed when the premixed branches are folded into the diffusion flame or when high strain rates result in the extinction of the premixed branches. Wegner [182] reviewed partially premixed combustion in the context of LES of gas turbine combustors. Triple flames are involved in the stabilization of non-premixed lifted flames [109].

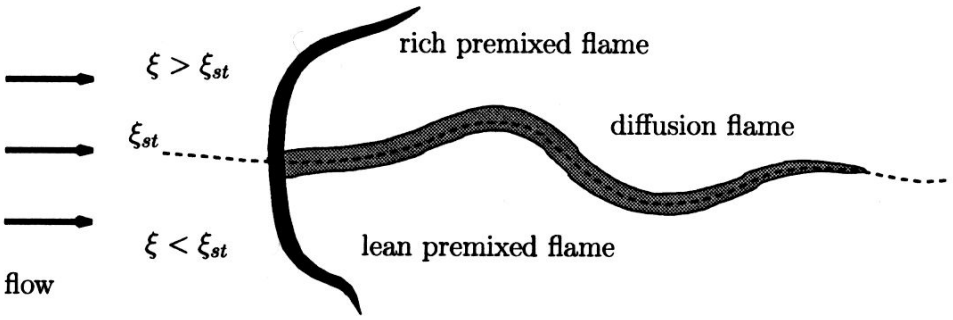

Figure 2.5: Sketch of a triple flame characteristic of partially premixed combustion. (Reproduced from [182])

Partially premixed combustion is involved in flame propagation in stratified mixtures subsequent to ignition in a mixing layer. Hence, this regime is found in both autoignition and forced ignition of non-premixed turbulent configurations. The effects of mixture stratification on turbulent flame propagation have been investigated with 3-D DNS in the context of autoignition [47] and forced ignition [31, 148, 32, 98]. Even though consequent research efforts have been dedicated to turbulent flame speed in partially premixed combustion, the joint effects of turbulence and mixture stratification have not been integrated yet into a general expression for turbulent flame speed. In this work, the local turbulent flame speed in stratified mixtures with high level of premixedness is evaluated from the expression for turbulent premixed flame speed (Eq. 2.39).

3 Modeling Approaches

The underlying basics involved in combustion physics were presented in the previous chapter. Although the governing equations are known, the direct resolution of reacting turbulent flows is beyond the scope of most applications. Therefore, turbulent flow and chemical reaction need to be modeled. The modeling approaches applied within this work for both turbulent flow and combustion are presented in this chapter.

3.1 Turbulence and Mixing Modeling

The physical fundamentals of turbulence were introduced in Section 2.2. To capture the nature of the physics, three principal modeling approaches with different level of complexity can be applied. These methods consist in solving the governing flow equations (Section 2.1) without any modeling (DNS: *Direct Numerical Simulation*), in solving the time-averaged flow equations (RANS: *Reynolds-Averaged Navier-Stokes Simulation*) or in solving the spatially filtered flow equations (LES: *Large Eddy Simulation*).

3.1.1 Direct Numerical Simulation

Once the initial and boundary conditions of a turbulent flow are given, the system is set up and the governing equations of Section 2.2 can be fully resolved with finite computational effort. DNS are commonly used to improve the understanding of fundamental phenomena, and to provide reliable data for validating modeling approaches. The spatial and temporal resolution of the smallest turbulent structures requires to use fine discretization sizes that are dictated by the Kolmogorov scales (Section 2.2). The computational domain must contain the larger scales defined by the integral length scale l_t, hence the number of nodes N_{DNS} scales as:

$$N_{DNS} \sim \left(\frac{l_t}{\eta_k}\right)^3 \approx Re_t^{3/4}. \tag{3.1}$$

Moreover, a stability criterion for temporal discretization, referred to as CFL number (Courant Friedrich Levy, [61]), imposes a restriction on the time-step, that should scale with the distance between two nodes. Finally, the computational effort for a DNS, E_c,

scales as:

$$E_c \sim N_{DNS} \times N_{DNS}^{1/3} \approx Re_t^3. \tag{3.2}$$

This cubic scaling law is inherent to DNS of turbulent flows and restricts the applicability of DNS to moderate turbulent Reynolds numbers.

3.1.2 Reynolds-Averaged Navier-Stokes Simulation

In many technical applications only time-averaged values are of interest. Therefore, a splitting into mean quantities and fluctuations is applied according to Reynolds [144]:

$$\phi = \overline{\phi} + \phi', \tag{3.3}$$

where $\overline{\phi}$ denotes mean quantities (time-averaged) and ϕ' fluctuations.

Applying this definition to the instantaneous mass conservation equation (Eq. 2.1), a time-averaged equation is derived:

$$\frac{\partial \overline{\rho}}{\partial t} + \frac{\partial \overline{\rho u_i}}{\partial x_i} = \frac{\partial \overline{\rho}}{\partial t} + \frac{\partial (\overline{\rho}\ \overline{u_i})}{\partial x_i} + \frac{\partial \rho' u_i'}{\partial x_i} = 0. \tag{3.4}$$

In this equation an unknown term of correlated fluctuations appears. However, this term can be discarded, applying a density averaging of the quantities referred to as *Favre averaging* and defined by:

$$\widetilde{\phi} = \frac{\overline{\rho\phi}}{\overline{\rho}}. \tag{3.5}$$

Hence, the time-averaged continuity equation reads:

$$\frac{\partial \overline{\rho}}{\partial t} + \frac{\partial \overline{\rho}\widetilde{u}_i}{\partial x_i} = 0. \tag{3.6}$$

With respect to the Favre decomposition, fluctuations are denoted as:

$$\phi'' = \phi - \widetilde{\phi}. \tag{3.7}$$

The momentum equation (Eq. 2.2) is rewritten as:

$$\frac{\partial \overline{\rho}\widetilde{u}_i}{\partial t} + \frac{\partial \overline{\rho}\widetilde{u}_i\widetilde{u}_j}{\partial x_i} = \frac{\partial}{\partial x_i}\left[\widetilde{\tau_{ij}} - \overline{\rho}\widetilde{u_i''u_j''}\right] - \frac{\partial \overline{p}}{\partial x_i}. \tag{3.8}$$

Contrary to mass conservation, the conservation of momentum exhibits a quadratic dependency of the velocity fluctuations. This non-linearity results in an unclosed stress term, known as Reynolds stress: $\overline{\rho}\widetilde{u_i''u_j''}$, and which represents the momentum flux due

to turbulent motions. To close the quadratic term, $\widetilde{\overline{\rho} u_i'' u_j''}$, a transport equation can be defined. However, an unclosed cubic term would then appear among others. The closure of turbulence can be achieved by modeling the unknown term using mean values. At the first level, *Boussinesq's eddy viscosity approximation* is usually applied. It assumes that the Reynolds stress tensor is proportional to the trace-less mean strain rate tensor and reads:

$$\widetilde{\overline{\rho} u_i'' u_j''} = -\mu_t \left(\frac{\partial \widetilde{u}_i}{\partial x_j} + \frac{\partial \widetilde{u}_j}{\partial x_i} - \frac{2}{3} \delta_{ij} \frac{\partial \widetilde{u}_k}{\partial x_k} \right) + \frac{2}{3} \overline{\rho} \tilde{k}, \tag{3.9}$$

where $\tilde{k} = \frac{1}{2} \widetilde{u_i'' u_j''}$ denotes the kinetic energy and μ_t represents the so-called turbulent eddy viscosity. Different classes of closure models with varying complexity levels were proposed and successfully applied.

- The simplest closure relies on *algebraic models*, also known as *zero equation models*, where the Reynolds stress tensor is calculated using an algebraic expression for the mean strain rate tensor, as in, for instance, the *mixing length model* by Prandtl [142].

- In *one equation models*, an additional transport equation is solved, typically for the turbulent kinetic energy, k. However, supplementary information, typically a length scale, must be specified.

- Most RANS turbulence models rely on *two equations models*, where a second transport equation is solved [100]. The k-ε model introduced by Jones and Launder [89] solves a transport equation for the turbulence energy, k, and for its dissipation, ε. This instance is probably the most popular example in engineering applications, since it associates good numerical stability and reasonable accuracy. The turbulence viscosity, turbulence length scale and time scale are defined as:

$$\nu_t = C_\mu \frac{\widetilde{k}^2}{\widetilde{\varepsilon}} \; ; \quad l_t = \frac{\widetilde{k}^{3/2}}{\widetilde{\varepsilon}} \; ; \quad \tau_t = \frac{\widetilde{k}^{3/2}}{\widetilde{\varepsilon}} \tag{3.10}$$

  where the value of parameter C_μ is 0.09.

- At the second level, there exist *Reynolds stress models* to solve a transport equation for every second moment terms $\widetilde{u_i'' u_j''}$ [107]. Such models are no longer based on the Boussinesq approximation and are capable of dealing with anisotropic turbulence. However, they remain computationally costly in comparison to two-equation models.

Applying Favre decomposition to the scalar transport 2.5 yields its averaged form:

$$\frac{\partial(\bar{\rho}\widetilde{\phi})}{\partial t} + \frac{\partial\left(\bar{\rho}\widetilde{\phi}\widetilde{u}_i\right)}{\partial x_i} = \frac{\partial}{\partial x_i}\left[\bar{\rho}\widetilde{D}_\phi\frac{\partial\widetilde{\phi}}{\partial x_i} - \overline{\rho\phi''u_i''}\right] + \widetilde{\omega}_\phi. \tag{3.11}$$

The scalar flux due to turbulent motion, $\overline{\rho\phi''u_i''}$, is closed using a gradient assumption:

$$\overline{\rho\phi''u_i''} = -\frac{\mu_t}{Sc_{\phi,t}}\frac{\partial\widetilde{\phi}}{\partial x_i}, \tag{3.12}$$

where μ_t is the turbulent viscosity and $Sc_{\phi,t}$ the turbulent Schmidt number for scalar ϕ. The source term, $\widetilde{\omega}_\phi$, represents the time-averaged source term of scalar, ϕ, such as a chemical species and needs to be modeled, as presented in Section 3.2.

3.1.3 Large Eddy Simulation

Large eddy simulations solve the larger structures of the turbulent flow, while the small eddies are modeled. This approach relies on the fact that most of the turbulent kinetic energy is contained in the large structures, while the effects of the small eddies can be modeled due to their universal and nearly isotropic character. The cut-off size of the resolved eddies can be defined according to the accuracy requirements. Therefore, LES permits the resolution of unsteady turbulent flows of many technical systems at computational costs that are acceptable to research purposes and within current computing capabilities. Following the development of computing technologies and the emergence of skilled users, temporally resolved calculations are on the way to becoming an engineering tool.

Spatial Filtering

The separation between the large resolved and the small modeled scales is achieved by applying a spatial low-pass filter. Thus, the filtered field of a quantity ϕ is determined by convolution with a LES filter, G, by:

$$\overline{\phi(x,t)} = \int \phi\left(x - x', t\right)\ G\left(x'\right) dx'. \tag{3.13}$$

In general, any normalized low-pass filter can be applied. The most frequently used consists of a volume-averaged top-hat filtering introduced by Deardorff [42] and extended

for non-uniform grids by Schumann [151].

$$\overline{\phi(x,y,z,t)} = \frac{1}{\Delta^3}\int_{x-\Delta x}^{x+\Delta x}\int_{y-\Delta y}^{y+\Delta y}\int_{z-\Delta z}^{z+\Delta z}\phi\left(x',y',z',t\right)dx'dy'dz'. \tag{3.14}$$

The LES filter size, Δ, represents the averaged filter length, $\Delta = (\Delta x \Delta y \Delta z)^{1/3}$.

Transport of Mass

Applying Favre-filtering to the equation of mass conservation (Eq. 2.1) yields the continuity equation for LES (Eq. 3.15), which can be solved in terms of filtered quantities.

$$\frac{\partial\overline{\rho}}{\partial t} + \frac{\partial(\overline{\rho}\widetilde{u_i})}{\partial x_i} = 0 \tag{3.15}$$

Transport of Momentum

The Navier-Stokes equations for LES (Eq. 3.16) are obtained by filtering the momentum equations 2.2:

$$\frac{\partial(\bar{\rho}\widetilde{u_i})}{\partial t} + \frac{\partial(\bar{\rho}\widetilde{u_i}\widetilde{u_j})}{\partial x_j} = -\frac{\partial\overline{p}}{\partial x_i} + \frac{\partial\widetilde{\tau_{ij}}}{\partial x_j} + \frac{\partial\left(\overline{\rho}\tau_{ij}^{sgs}\right)}{\partial x_j}. \tag{3.16}$$

Thereby, $\widetilde{\tau_{ij}}$ represents the resolved deviatoric stress tensor:

$$\widetilde{\tau_{ij}} = 2\overline{\mu}\left[\widetilde{S_{ij}} - \frac{1}{3}\widetilde{S_{kk}}\delta_{ij}\right], \tag{3.17}$$

where $\widetilde{S_{ij}}$ represents the filtered strain rate tensor:

$$\widetilde{S_{ij}} = \frac{1}{2}\left(\frac{\partial\widetilde{u_j}}{\partial x_i} + \frac{\partial\widetilde{u_i}}{\partial x_j}\right). \tag{3.18}$$

The last term on the right-hand-side of Eq. 3.16 is the residual stress tensor. It accounts for the momentum flux due to sub-grid motions and is called the sub-grid scale (SGS) stress tensor:

$$\tau_{ij}^{sgs} = \widetilde{u_i}\widetilde{u_j} - \widetilde{u_i u_j}. \tag{3.19}$$

Sub-grid Stress Modeling

The SGS stress tensor τ_{ij}^{sgs} appears in an unclosed form and needs to be modeled. The following paragraphs introduce the sub-grid scale modeling approaches applied within this work.

Eddy Viscosity

Boussinesq's eddy viscosity approximation assumes that the effects of the small scales on the flow are similar to those of the molecular viscosity. Accordingly, the sub-grid term τ^{sgs}, which accounts for these effects can be retrieved by defining a turbulent viscosity, ν_t. Hence, the sub-grid stress is modeled as:

$$\tau_{ij}^{sgs} - \frac{1}{3}\tau_{kk}^{sgs}\delta_{ij} = 2\nu_t\left[\widetilde{S_{ij}} - \frac{1}{3}\widetilde{S_{kk}}\delta_{ij}\right] = \nu_t\left(\frac{\partial\widetilde{u_j}}{\partial x_i} + \frac{\partial\widetilde{u_i}}{\partial x_j}\right) - \frac{2}{3}\nu_t\frac{\partial\widetilde{u_k}}{\partial x_k}\delta_{ij}. \tag{3.20}$$

Introducing the effective viscosity $\nu_{eff} = \nu + \nu_t$, the filtered Navier-Stokes equations (Eq. 3.16) can be rewritten as:

$$\frac{\partial\bar{\rho}\widetilde{u_i}}{\partial t} + \frac{\partial\bar{\rho}\widetilde{u_i}\widetilde{u_j}}{\partial x_j} = -\frac{\partial\overline{P}}{\partial x_i} + 2\overline{\rho}\nu_{eff}\left[\widetilde{S_{ij}} - \frac{1}{3}\widetilde{S_{kk}}\delta_{ij}\right]. \tag{3.21}$$

The pressure parameter $\overline{P}$ is introduced to incorporate the trace of the sub-grid stress tensor (Eq. 3.22). The pressure correction scheme is applied to determine the value of the pressure parameter, $\overline{P}$, so that the conservation of mass is satisfied, whilst the physical pressure, $\overline{p}$, remains unknown.

$$\overline{P} = \overline{p} - \frac{1}{3}\rho\tau_{kk}^{sgs} \tag{3.22}$$

Smagorinsky Model

In order to solve the momentum equation (Eq. 3.21), the turbulent viscosity, ν_t, needs to be closed. The closure introduced by Smagorinsky [152] relates the turbulent viscosity to the LES filter length Δ and to the strain rate tensor $\widetilde{S_{ij}}$ as:

$$\nu_t = (C_s\Delta)^2\,|\widetilde{S}|, \tag{3.23}$$

with

$$\left|\widetilde{S}\right| = \sqrt{2\widetilde{S_{ij}}\widetilde{S_{ij}}}. \tag{3.24}$$

The the constant C_s is a model parameter, which is referred to as the *Smagorinsky constant*. A major drawback of this approach is the dependency of the constant on the flow region. While Lilly [115] proposed a value of $C_s = 0.173$, Piomelli et al. [134] suggested a value of $C_s = 0.065$ for a channel flow. Indeed, significant variations in the considered flow region have been identified. In particularly, a reasonable value for C_s in a channel flow is 0.2, while a value of 0.065 is more appropriate near walls.

Germano Dynamic Procedure

The dependency of the Smagorinsky constant on the location within the flow field is

overcome by applying an additional test filtering to determine the local constant value. This method, referred to as the *Germano Dynamic Procedure* [65], relies on the fact that the correct value of C_s is expected to yield the same amount of turbulence, no matter what the filter size. Thus, Germano applied a test filter to the already filtered field , $\widehat{*}$, using a filter size Γ larger than the filter size Δ. Similar to the decomposition of the correlation term $\widetilde{u_i u_j}$ (Eq. 3.19), introduced for the filtered Navier-Stokes equations 3.16, a fine structure $\tau_{ij}^{sgs,\Gamma}$ resulting from the double filtering is defined as a residual term between the unknown correlation term $\widehat{\widetilde{u_i u_j}}$ and its resolved part $\widehat{\widetilde{u}}_i \widehat{\widetilde{u}}_j$:

$$\tau_{ij}^{sgs,\Gamma} = \widehat{\widetilde{u}}_i \widehat{\widetilde{u}}_j - \widehat{\widetilde{u_i u_j}}. \tag{3.25}$$

Applying the test filter to the sub-grid stress $\tau_{ij}^{sgs,\Delta}$ yields:

$$\widehat{\tau_{ij}^{sgs,\Delta}} = \widehat{\widetilde{u}_i \widetilde{u}_j} - \widehat{\widetilde{u_i u_j}}. \tag{3.26}$$

Combining Equations 3.25 and 3.26 gives the Germano identity, Eq. 3.27:

$$L_{ij} = \tau_{ij}^{sgs,\Gamma} - \widehat{\tau_{ij}^{sgs,\Delta}} = \widehat{\widetilde{u}}_i \widehat{\widetilde{u}}_j - \widehat{\widetilde{u_i}\widetilde{u_j}}. \tag{3.27}$$

Applying the eddy viscosity approach, Eq. 3.20, and the Smagorinsky approximation of turbulent viscosity, Eq. 3.23, to both sub-grid stresses yields:

$$\tau_{ij}^{sgs,\Delta} - \frac{1}{3}\tau_{kk}^{sgs,\Delta}\delta_{ij} = 2C_g\Delta^2|\widetilde{S}|\left[\widetilde{S_{ij}} - \frac{1}{3}\widetilde{S_{kk}}\delta_{ij}\right] = 2C_g m_{ij}^{sgs,\Delta}, \tag{3.28}$$

$$\tau_{ij}^{sgs,\Gamma} - \frac{1}{3}\tau_{kk}^{sgs,\Gamma}\delta_{ij} = 2C_g\Gamma^2|\widetilde{S}|\left[\widetilde{S_{ij}} - \frac{1}{3}\widetilde{S_{kk}}\delta_{ij}\right] = 2C_g m_{ij}^{sgs,\Gamma}, \tag{3.29}$$

where the Germano parameter, $C_g = C_s^2$, has been substituted with the Smagorinsky constant, C_s. Thus, the Germano identity, Eq. 3.27, can be rewritten as:

$$L_{ij} - \frac{1}{3}L_{kk}\delta_{ij} = 2C_g M_{ij}, \tag{3.30}$$

where

$$M_{ij} = \widehat{m_{ij}^{sgs,\Delta}} - m_{ij}^{sgs,\Gamma}. \tag{3.31}$$

Equation 3.30 is an overdetermined system of equations, with five independent components since the trace is zero. Lilly [116] proposed solving this system by a least-square approach, which leads to the following formula for the Germano parameter:

$$C_g = \frac{M_{ij}L_{ij}}{2M_{kl}M_{kl}}. \tag{3.32}$$

Accordingly, the Germano procedure may lead to negative values of C_g. This is inconsistent with the Smagorinsky model and a clipping is applied (Eq. 3.33) to restrict C_g to positive values.

$$C_g = max\left(0., \frac{M_{ij}L_{ij}}{M_{kl}M_{kl}}\right) \tag{3.33}$$

Scalar Transport

Filtering the scalar transport equation (Eq. 2.5) yields the transport equation for LES:

$$\frac{\partial(\bar{\rho}\widetilde{\phi})}{\partial t} + \frac{\partial\left(\bar{\rho}\widetilde{\phi}\widetilde{u_i}\right)}{\partial x_i} = \frac{\partial}{\partial x_i}\left(\bar{\rho}\widetilde{D_\phi}\frac{\partial\widetilde{\phi}}{\partial x_i} + \bar{\rho}F^{sgs}_{\phi,i}\right) + \widetilde{\omega_\phi}, \tag{3.34}$$

where the convection term, $\widetilde{\phi u_i}$, is separated into its resolved part $\widetilde{\phi}\widetilde{u_i}$ and a fine-structure scalar flux term $F^{sgs}_{\phi,i}$.

$$\widetilde{\phi u_i} = \widetilde{\phi}\widetilde{u_i} - F^{sgs}_{\phi,i} \tag{3.35}$$

Modeling of the Sub-grid Scale Scalar Flux

The fine structure scalar flux term, $F^{sgs}_{\phi,i}$, in Eq. 3.34 is unknown and must be modeled. Similar to the modeling of the SGS momentum flux, turbulence is assumed to contribute to mixing in the same way as an additional diffusion. Thus, the sub-grid scalar transport due to turbulence is approximated with an *eddy diffusivity* approach, which is similar to the eddy viscosity approach. Therefore, a *turbulent diffusivity*, $D_{\phi,t}$, is introduced to relate the sub-grid flux to the scalar gradient, $\frac{\partial\tilde{\phi}}{\partial x_i}$, as:

$$F^{sgs}_{\phi,i} = D_{\phi,t}\frac{\partial\tilde{\phi}}{\partial x_i}. \tag{3.36}$$

Introducing Eq. 3.36 into Eq. 3.34 yields:

$$\frac{\partial(\bar{\rho}\widetilde{\phi})}{\partial t} + \frac{\partial\left(\bar{\rho}\widetilde{\phi}\widetilde{u_i}\right)}{\partial x_i} = \frac{\partial}{\partial x_i}\left(\bar{\rho}\left(\widetilde{D_\phi} + D_{\phi,t}\right)\frac{\partial\widetilde{\phi}}{\partial x_i}\right) + \widetilde{\omega_\phi}. \tag{3.37}$$

Within the CFD code, the diffusion coefficient $D_{\phi,t}$ is retrieved through the Schmidt number, Sc, which defines the ratio of momentum transport due to viscosity to the scalar transport due to diffusion. In the same sense, a turbulent Schmidt number, Sc_t, is intro-

duced for comparing the fluxes due to turbulence:

$$Sc = \frac{\nu}{D_f} \approx \frac{\tilde{\nu}}{\widetilde{D_f}} \quad ; \qquad Sc_t = \frac{\nu_t}{D_{f,t}}. \tag{3.38}$$

The laminar Schmidt number, Sc, is accepted as 0.7. A range of values were applied for the turbulent Schmidt number of mixture fraction, from $Sc_t = 0.4$ in [137] $Sc_t = 0.7$ in [22], [94] and [45]. Following [94, 45] a constant value of $Sc_t = 0.7$ has been used throughout this work. The source term, $\widetilde{\dot{\omega}_\phi}$, represents the spatially filtered source term of scalar, ϕ and needs to be modeled for chemical reactions. The next section presents the modeling approaches used within this work.

3.2 Combustion Modeling

The fundamentals of reaction kinetics, ignition and combustion regimes were presented in Section 2.3. The chemical reaction of simple fuels, such as methane, CH_4, involves numerous chemical species and a wide range of time scales. Hence, the direct resolution of kinetics mechanisms is restricted to simple fundamental configurations such as laminar flames. Combustion modeling is required to simulate technical systems. This section presents the modeling approaches used within this work. For a more complete discussion on modeling approaches, please refer to Poinsot and Veynante [139].

3.2.1 Equilibrium Chemistry

Equilibrium chemistry is a simplified combustion modeling approach, where the effects of chemical kinetics are neglected. For constant pressure system, the chemical composition space at equilibrium is determined by minimizing of the free enthalpy. Since the thermodynamic properties of the mixture at equilibrium only depend on the mixture fraction, modeling turbulent combustion consists of modeling turbulent mixing, with the difference that the density of the mixture does not follow the law for non-reactive mixing between two feeds but is an equation of state derived from the thermodynamic properties at equilibrium. Although this combustion modeling was not used in this work, a numerical method for solving chemical equilibrium was used to compute the steady state subsequent to autoignition.

3.2.2 Flamelet Approach

In 1975, Williams [184] first suggested that turbulent flames can be represented by an ensemble of laminar flames, assuming that turbulent structures are not able to disturb

the inner structure of the thin reacting layers. These laminar flames are called flamelets and usually refer to non-premixed combustion. The flamelets are embedded in the turbulent field, which is assumed to exhibit a Kolmogorov length scale larger than the flame thickness. Hence, this approach is, in principle restricted to turbulent reacting flows with a Karlovitz number smaller than one. This section is based on the book by Peters [131], who is probably the most prominent developer of the flamelets concept.

According to the description of non-premixed combustion in Section 2.3.3, flamelets are located on the iso-surfaces of stoichiometric mixture fraction $f = f_{st}$. Neglecting compressibility, the balance equation of species mass fraction, x_α, transport is obtained from Eq. 2.5 and reads for a given species α:

$$\rho\frac{\partial x_\alpha}{\partial t} + \rho u_i\frac{\partial x_\alpha}{\partial x_i} = \frac{\partial}{\partial x_i}\left(\rho D_\alpha\frac{\partial x_\alpha}{\partial x_i}\right) + \dot{\omega_{x_\alpha}}. \tag{3.39}$$

According to Peters [131], this equation can be expressed in a coordinates system (f, f_2, f_3), which combines mixture faction and spatial coordinates. The mixture fraction coordinate f is normal to the flame surface (or the stoichiometric iso-surface), while the spatial coordinates $(f_2, f_3) = (x_2, x_3)$ are tangential to this surface. Hence, the coordinates transformation rules read:

$$\frac{\partial}{\partial x_1} = \frac{\partial f}{\partial x_1}\frac{\partial}{\partial f}, \tag{3.40}$$

$$\frac{\partial}{\partial x_2} = \frac{\partial}{\partial f_2} + \frac{\partial f}{\partial x_2}\frac{\partial}{\partial f}, \tag{3.41}$$

$$\frac{\partial}{\partial x_3} = \frac{\partial}{\partial f_3} + \frac{\partial f}{\partial x_3}\frac{\partial}{\partial f}. \tag{3.42}$$

In thin laminar flamelets the species balance equations are dominated by diffusion fluxes in f direction. Hence, applying the coordinates transformation to Eq. 3.39 yields:

$$\rho\frac{\partial x_\alpha}{\partial t} - \rho D_\alpha\left(\frac{\partial f}{\partial x_i}\frac{\partial f}{\partial x_i}\right)\frac{\partial^2 x_\alpha}{\partial f^2} = \dot{\omega_{x_\alpha}}. \tag{3.43}$$

Introducing the rate of scalar dissipation χ as:

$$\chi = 2D_k\left(\frac{\partial f}{\partial x_i}\frac{\partial f}{\partial x_j}\right), \tag{3.44}$$

the well-known *flamelet equation* [131] is retrieved:

$$\rho\frac{\partial x_\alpha}{\partial t} - \rho\frac{\chi}{2}\frac{\partial^2 x_\alpha}{\partial f^2} = \dot{\omega_{x_\alpha}}. \tag{3.45}$$

High reaction rates are found in thin flames, where the mixture fraction gradient is high, as well as the resulting diffusion. However, for high values of χ, strong diffusion may transport so many radicals away from the thin reacting zone, that the flame is quenched. Lower scalar dissipation rates correspond to wider flames. For asymptotic low values of χ, no flame is observed anymore, while the assumption of thin flames tends to become invalid.

Since chemical time scales are small, the accumulation rate $\rho\frac{\partial x_\alpha}{\partial t}$ in Eq. 3.45 can be neglected in most cases. The subsequent *steady flamelet equation* reads:

$$-\rho\frac{\chi}{2}\frac{\partial^2 x_\alpha}{\partial f^2} = \dot{\omega_{x_\alpha}}. \tag{3.46}$$

Applying a reaction mechanism, the set of equations (Eq. 3.46) for a given value of scalar dissipation rate can be integrated over the mixture fraction f. Hence, the species mass concentrations x_α can be retrieved in the turbulent reacting flow as a function of f and χ only. Thus, instead of solving the full set of species balance equations within the turbulent reacting flow, the full chemistry can be integrated in advance and stored in a look-up table as a comprehensive set of parameters f and χ.

However, the thermodynamic properties provided by the steady flamelet library are restricted to a domain of scalar dissipation rates issuing steady flamelets. This domain corresponds to the stable burning branch of the S-shaped curve (Figure 3.1) and does not cover the whole range of scalar dissipation rates found in technical systems. Hence, for scalar dissipation rates beyond the quenching limit, no steady flamelet can be calculated. The thermodynamic properties can be retrieved by interpolation to the pure mixing or extinction limit. In order to better account for the effects of local extinction and re-ignition in the turbulent flame brush, unsteady flamelets can be used. Thus, an *equivalent strain rate* was introduced by Cuenot et al. [36], for describing a fictitious dissipation rate that represents the evolution of a quenching flamelet, and incorporates the memory of the flame structure of the steady flamelet at critical dissipation rate. Pierce and Moin [132] and Ihme et al. [81] revisited the scalar dissipation concept using a progress variable to account for the local ignition and extinction. Figure 3.1 shows the maximal temperature across a methane-air reacting layer obtained by Pierce [133] for both steady burning flames and for the unstable branch of highly strained extinguishing flamelets.

3.2.3 Flamelet Generated Manifolds

Similar to the flamelet method, the *Flamelet Generated Manifolds* (FGM) model represents the reacting composition space using a comprehensive set of precomputed one-

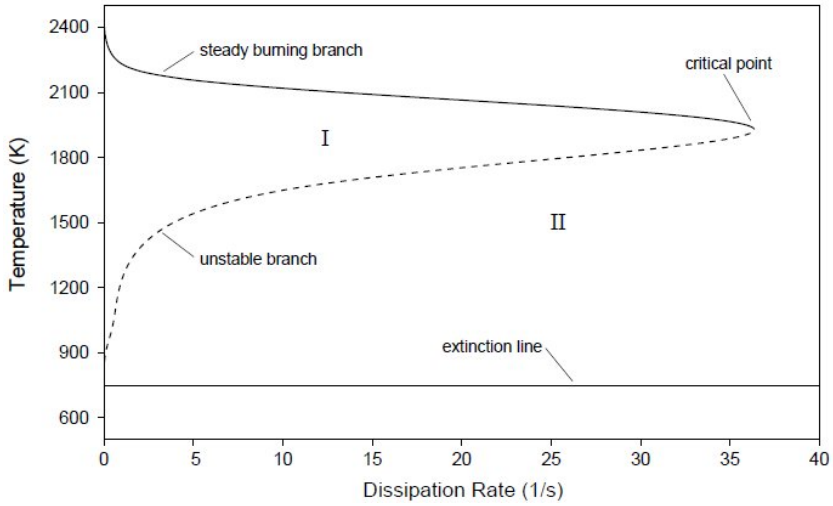

Figure 3.1: S-shaped curve of the combustion of non-premixed methane-air mixing layer exhibiting the steady burning branch, the unstable branch and the pure mixing or extinction limit. (Reproduced from [133], 750K air, 300K methane, 3.8 atm).

dimensional flamelets. Whereas the standard flamelet concept relies on the resolution of the detailed chemistry of a range of strained mixing layers between fuel and oxidizer according to the flamelet equation (Eq. 3.46), de Goey and Boonkkamp [40, 41] proposed to describe the reacting composition space using a set of one-dimensional free propagating premixed flames. A brief presentation of the FGM model is given in the following paragraphs. For more details, please refer to the work by van Oijen [171].

According to van Oijen [171], a premixed flame is defined as the region of space, where a scalar variable assumes values between $c_u = 0$ in the unburned gases and $c_b = 1$ in the burned gases. The subscripts u and b denote unburned and burned state, respectively. A suitable progress variable Y can be chosen as any strictly monotonic increasing linear combination of species mass fractions, Eq. 3.47.

$$Y = \sum_{\alpha} b_\alpha Y_\alpha, \tag{3.47}$$

where b_α denote the weighting factor of species α. The value of the progress variable at equilibrium is noted Y_{eq}. Hence, a normalized progress variable c is defined as:

$$c = \frac{Y}{Y_{eq}}. \tag{3.48}$$

The resolution of premixed flames is based on the resolution of a set of transport equations for enthalpy and for involved chemical species. Therefore, the flames are considered

in steady-state and solved over a one-dimensional grid, which is more refined in the inner reaction layer (Section 2.3.4). Steady-state is ensured by adjusting the inflow velocity of fresh gas to the value of the computed laminar flame velocity, s_L, and by defining a criterion for locating the inner reaction layer in the refined grid region. For instance, the flame point corresponding to a temperature increase of $200K$, $T = T_0 + 200K$, is commonly set at the beginning of the refined grid ($x = 0$). The steady-state equation for mass conservation reduces to:

$$\rho_0 u = \rho_u s_L = \dot{m} = const., \tag{3.49}$$

where $\dot{m}$ is the constant mass flux and ρ_0 the density of the fresh gas. The steady-state transport equation for species α reads:

$$\dot{m}\frac{\partial Y_\alpha}{\partial x_i} - \frac{\partial}{\partial x_i}\left(\rho D_\alpha \frac{\partial Y_\alpha}{\partial x_i}\right) = \dot{\omega_{Y_\alpha}}. \tag{3.50}$$

The steady-state enthalpy equation reads:

$$\dot{m}\frac{\partial h}{\partial x_i} - \frac{\partial}{\partial x_i}\left(\frac{\lambda}{c_p}\frac{\partial h}{\partial x_i}\right) = -\sum_\alpha h_\alpha \dot{\omega_{Y_\alpha}} - \sum_\alpha \rho Y_\alpha U_\alpha \frac{\partial h}{\partial x_i}. \tag{3.51}$$

In this equation, the term $\sum \rho Y_\alpha U_\alpha \frac{\partial h}{\partial x_i}$ represents the enthalpy flux induced by species diffusion fluxes and is small compared to the other terms, see [156] for more details. The set of species and elementary reactions, as well as all thermodynamic properties are provided by a kinetics mechanism, such as the GRI3 mechanism for methane [153]. Since species' binary diffusion coefficients are also provided by kinetics mechanisms, complex differential diffusion may be accounted for. However, it is common practice to consider constant Lewis numbers, Eq. 2.25, for hydrocarbons fuels, with the exception of hydrogen flames, since the effect of the higher diffusivity of the small hydrogen atoms may be significant for hydrogen combustion.

Within this work, premixed flamelets have been calculated using the one-dimensional laminar flamelet code Chem1D [33], with constant Lewis numbers. Steady state is enforced by setting a criterion for defining a fixed flame position within the one-dimensional computational grid. The standard criterion was applied. It sets the flame point at a temperature 200 K higher than the temperature on the fresh gas side at the grid origin. At this location a more refined grid is applied to solve the inner reaction layer, as presented in Section 2.3.4.

For a given mixture fraction, f, the flamelet solution consists of a set, ψ_f, of thermodynamic properties of the chemical composition space, such as density and temperature, and of the respective chemical source terms as a function of the coordinate x:

$$\psi_f = (\rho, T, Y_\alpha, \dot{\omega_\alpha})_f = \psi_f(x). \tag{3.52}$$

Defining a progress variable, Y, as a linear combination of species mass fractions, for example, $Y = CO_2 + CO$, which is strictly monotonic increasing over the computational domain, a bijection into the progress variable domain $[Y_u, Y_b]$ can be established (Eq. 3.53). Thus, the flamelet solution, ψ_f, can be remapped as a function of the progress variable, Y, or for convenience purposes, as a function of the normalized progress variable, c:

$$\psi_f(x) \;\mapsto\; \psi_f(Y) \;\mapsto\; \psi_f(c). \tag{3.53}$$

Premixed flamelets can be solved over a range of mixture fractions within the lean and rich flammability limits, f_l and f_r, respectively. Hence, calculating a comprehensive set of flamelets allows the description of laminar premixed combustion chemistry for any flammable mixtures. The pre-computed flamelets are therefore stored in a two-dimensional look-up table, Eq. 3.54, or FGM table, for further use in the numerical calculation.

$$\psi_{FGM} = \psi(f, c). \tag{3.54}$$

This two-dimensional look-up table describes the composition space of laminar flames within the flammability limits. The FGM method has been validated for application to non-premixed configurations, for instance by Vreman et al. [173] for the Sandia flame D and F, in the context of turbulent combustion (Section 3.3). For describing the composition space for non-flammable mixtures a linear extrapolation was applied. In this work, the species mass fractions, the progress variable, the temperature and density inverse are also supposed to follow a linear law. This extension method results in inconsistencies, that are assumed to be moderate in the investigated cases. Ketelheun et al. [95, 96, 129] proposed an improved extrapolation method.

A similar method can be applied to describe the composition space of autoigniting configurations, as presented in Section 3.2.4. Hence, the modeling of turbulence-chemistry interaction is presented for both reaction types in section 3.3.

3.2.4 Autoignition

This section presents a method for describing the composition space of autoigniting configurations applying a progress variable approach. The method is based on the com-

putation of constant pressure autoigniting homogeneous reactors, also referred to as well-stirred reactors. The presentation of modeling approaches for autoignition is restricted in this section to the approach that has been used in this work. For more information on modeling approaches for autoignition, refer to the works by Brandt [21] and by Bikas [13].

Autoignition of Methane

The principles of methane autoignition according to the book of Law [108] are presented here. For methane, the ignition delay time t_{ign}, also called the induction time, has been empirically correlated by Tsuboi and Wagner [169] based on shock tube measurements in argon over the temperature range of 1200 to 2100 K:

$$t_{ign} = 2.5 \times 10^{-15} exp(26700/T)[CH_4]^{0.32}[O_2]^{-1.02}, \tag{3.55}$$

where t_{ign} is in seconds $[s]$, while the species molar concentrations $[CH_4]$ and $[O_2]$ are given in $[mol/cm^3]$. The delay decreases with increasing temperature. The positive effect of pressure on the induction process is indicated by the negative value sum of the concentrations exponents. The positive exponent for the methane concentration indicates the inhibitive effect of methane in the induction process, which can be explained by the elementary reaction involving CH_4 and H that competes with the chain-branching step of H [108].

The autoignition of methane consists of a sequence of elementary reactions, in which the hydrogen content of the original fuel molecule, CH_4, is progressively reduced to CH_3 and CH_3O, then to CH_2O, HCO, and finally to CO and CO_2 [108]. Prior to thermal runaway, the low-temperature oxidation of methane is governed by the rate of radical accumulation, according to two following initiation steps:

$$CH_4 + M \rightleftharpoons CH_3 + H + M \tag{3.56}$$

$$CH_4 + O_2 \rightleftharpoons CH_3 + HO_2 \tag{3.57}$$

The initiation step (3.56) is a large activation-energy, unimolecular reaction. This step can be favored over step (3.57) at high temperatures. Depending on the dominating initiation step, further elementary reactions involving CH_4 participate in further radical growth. Subsequently, the methyl radicals produced react with molecular oxygen through two reaction channels:

$$CH_3 + O_2 \rightleftharpoons CH_3O + O \tag{3.58}$$

$$CH_3 + O_2 \rightleftharpoons CH_2O + OH \tag{3.59}$$

Channel (3.59) appears to be a chain-carrying step, while channel (3.58) leads to the formation of CH_3O and chain branching. Hence, the relative contributions of the two channels to the overall rate constant, called branching ratio, is crucial in the process of methane ignition.
As the radical pool grows, the following reaction becomes the dominant step for methyl oxidation close to ignition:

$$CH_3 + HO_2 \rightleftharpoons CH_3O + OH \tag{3.60}$$

The highly active radical CH_3O is then converted to formaldehyde rapidly via:

$$CH_3O + M \rightleftharpoons CH_2O + H + M \tag{3.61}$$

$$CH_3O + O_2 \rightleftharpoons CH_2O + HO_2 \tag{3.62}$$

Subsequently, formaldehyde reacts with OH and O_2 to form the highly active formyl radical, HCO.

$$CH_2O + OH \rightleftharpoons HCO + H_2O \tag{3.63}$$

$$CH_2O + O_2 \rightleftharpoons HCO + HO_2 \tag{3.64}$$

Similarly to CH_3O, the formyl radical is consumed by the reactions:

$$HCO + M \rightleftharpoons H + CO + M \tag{3.65}$$

$$HCO + O_2 \rightleftharpoons CO + HO_2 \tag{3.66}$$

After ignition, the further conversion of CO to CO_2 is facilitated by the presence of the element hydrogen via the following reaction:

$$CO + OH \rightarrow CO_2 + H \tag{3.67}$$

The progressive reduction of the hydrogen content of the original fuel molecule is particularly noteworthy in understanding the kinetics of autoignition. Another route through which the size of the fuel molecule is increased should be also mentioned here. This route initiated a radical termination step between two methyl radicals CH_3, producing C_2 molecules consisting of two carbon atoms, such as C_2H_6 and C_2H_5, while the original fuel molecule consists of only one carbon atom. The influence of C_2 chemistry becomes important for rich mixtures, as the concentration of CH_3 radicals increases. In the same way, larger molecules consisting of three or four carbon atoms are formed, though the concentrations of larger molecules are small and their effects on the overall reaction response are negligible.

Kinetic Modeling of Autoignition

As described in the previous section, the autoignition of methane can be decomposed into elementary reactions. This set of elementary reactions together with the corresponding set of thermodynamic properties, constitute a comprehensive kinetic model. The comprehensive set of reactions can be solved analytically or used as a basis for applying mathematical reduction methods to generate simplified kinetics schemes. Surrogate fuels reproducing selected aspects of practical fuels containing higher hydrocarbons, such as diesel fuel and kerosene, are generally applied for developing chemical kinetic mechanisms. The chemical pathway involved in the reaction of high hydrocarbons is much more complex than for methane. Kinetics mechanism models also exist for such fuels, but they are usually optimized for a restricted domain of application and are under continuous development.

Kerosene surrogate fuels have been investigated, for example, in [78] and [34]. Honnet et al. [78] performed experimental and numerical investigations with a surrogate fuel made up of 80% n-decane and of 20% 1,2,4-trimethylbenzene by weight and mimicking among others the critical conditions of autoignition of kerosene in non-premixed flows. In particular, they could predict the air stream temperature at autoignition with good accuracy at low strains, assembling two mechanisms for n-decane and 1,2,4-trimethylbenzene. In the context of partially premixed, prevaporized kerosene spray combustion, Chrigui et al. [34] applied a chemical kinetic mechanism for dodecane, which is another surrogate fuel commonly used for kerosene, and investigated the influence of the degree of evaporation on temperature profiles.

Within this work, the autoignition of methane has been analytically solved using a kinetics mechanism from the Gas Research Institute of Berkeley University. Version GRI-3.0 was been applied. It is available in Chemkin format and can be downloaded from their website [153]. The mechanism is a compilation of 325 elementary chemical reactions, including C_1 to C_3 species and associated rate coefficient expressions and thermochemical parameters for the 53 species involved in them [153]. The mechanism was optimized to provide the best possible representation of natural gas flames and ignition. The optimization is based on a multitude of reliable experimental data [63]. The procedure involves a heuristic process based on exercised judgment, as well as mathematical optimization procedures, such as the genetic algorithm [53]. It has to be noted that the condition for which the mechanism was optimized are limited by availability of reliable optimization targets [153]. For ignition, the optimized domain is restricted to pressure lower than 20 *bar* and temperature higher than 1350 K [21].

Progress Variable Definition

From the description of the autoignition of methane it is possible to identify key species that are involved in the progressive reduction of the hydrogen content of the original CH_4 molecule. In particularly, the initiation steps lead to the formation of methyl CH_3, which can be seen as an indicator of the initiation. Further, the increase of the concentration of formaldehyde CH_2O is known to be an indicator of the induction process until consequent heat release and subsequent ignition are reached.

To couple the thermochemical properties of autoignition to the CFD code an indicator of the progress of autoignition needs to be defined. Similar to the FGM method presented in Section 3.2.3, a transported progress variable should allow access to the chemical state of each cell and to the chemical source term within the CFD code. As for the description of premixed flames using a progress variable approach, the choice of an appropriate progress variable should satisfy several requirements. The requirements for autoignition, as identified, for example, in [21] or [183], include the following points:

- Monotonicity with time should be guaranteed over the range of mixture fractions. The injectivity of the progress variable into the chemical composition space ensures the unicity of the chemical state corresponding to a progress variable value. Hence, the full set of thermochemical properties are defined through the specification a progress variable value.
- The progress variable should be definable and normalizable between 0. for the fresh gas to 1. for the reacted equilibrium state, over the range of mixture fractions.
- The progress variable should display a proper sensitivity to all stages involved in the autoignition process from the fresh gas to the equilibrium steady state. In particular, it should be possible to describe the concentration and the rate of formation of the radicals, including the build up of methyl, CH_3, from the fresh gas through the initiation step to the accumulation of formaldehyde prior to ignition and finally to the equilibrium state. This requirement is essential, not only for numerical stability, but also for capturing the ignition delay time within the CFD code.

The progress variable applied in this work includes the concentration of these radicals. The complete definition of the progress variable is presented further in Section 5.1.2, together with the justification and validation of the progress variable choice, based on numerical results.

Similarities with FGM Formalism

As detailed in Section 3.2.3, FGM is based on the resolution of a set of steady-state premixed flames on a one-dimensional computational grid, over a range of mixture fractions. The thermochemical properties are analytically solved along the flame front and the solution can be expressed as a function of the coordinate x (Eq. 3.52). Defining a suitable progress variable, Y, the flamelet solution, ψ_f, is remapped as a function of a normalized progress variable, c (Eq. 3.53). Finally, the set flamelets are integrated into a two-dimensional look-up table, Eq. 3.68, or FGM table, for further use in the numerical calculation.

$$\psi_{FGM} = \psi(f, c). \tag{3.68}$$

Similarly, a set of autoigniting homogeneous reactors are solved analytically over a range of mixture fractions. Nonetheless, autoignition of homogeneous reactors is resolved in time and performed in a zero-dimensional grid. Hence, the thermochemical properties during autoignition can be expressed as a function of time t:

$$\psi_{AI,f} = (\rho, T, Y_\alpha, \dot{\omega_\alpha})_{AI,f} = \psi_{AI,f}(t). \tag{3.69}$$

Hence, defining a progress variable, Y, according to the requirements previously described, the solution is remapped as a function of a normalized progress variable, c (Eq. 3.70).

$$\psi_{AI,f}(t) \;\mapsto\; \psi_{AI,f}(Y) \;\mapsto\; \psi_{AI,f}(c). \tag{3.70}$$

Finally, the set of solutions of autoigniting reactors are integrated into a two-dimensional autoignition look-up table (Eq. 3.71), for further use in the numerical calculation in the same manner as the FGM table.

$$\psi_{AI} = \psi(f, c). \tag{3.71}$$

Thus, the FGM formalism can be applied to the calculation of autoigniting configurations based on the pre-computation of autoigniting homogeneous reactors. In both cases, the thermochemical mixture properties can be accessed within the CFD code by solving a transport equation for the progress variable.

$$\frac{\partial(\rho Y)}{\partial t} + \frac{\partial\left(\rho Y u_i\right)}{\partial x_i} = \frac{\partial}{\partial x_i}\left(\rho D_Y \frac{\partial Y}{\partial x_i}\right) + \dot{\omega_Y}. \tag{3.72}$$

Following the definition of the progress variable, Eq. 3.47, the progress variable source term is defined as:

$$\dot{\omega_Y} = \sum_\alpha b_\alpha \dot{\omega_{Y_\alpha}}. \tag{3.73}$$

where α denotes the species included in the composition of the progress variable.

In the framework of turbulent combustion, the time-averaged, respectively spatially-filtered transport equation needs to be solved:

$$\frac{\partial(\bar{\rho}\widetilde{Y})}{\partial t} + \frac{\partial\left(\bar{\rho}\widetilde{Y}\widetilde{u}_i\right)}{\partial x_i} = \frac{\partial}{\partial x_i}\left[\bar{\rho}\widetilde{D_Y}\frac{\partial\widetilde{Y}}{\partial x_i} - J_i^Y\right] + \widetilde{\dot{\omega}_Y}, \tag{3.74}$$

where the progress variable flux due to unresolved turbulent motion, J_i^Y, is closed in the same manner as for a general scalar, Eq. 3.11 and Eq. 3.37, for RANS and LES, respectively. The time-averaged, respectively spatially-filtered, progress variable source term $\widetilde{\dot{\omega}_Y}$ needs to be closed to account for the effects of turbulence-chemistry interaction (Section 3.3).

3.2.5 Forced Ignition

Ignition in aero-engines in terms of ignition phases and their characterization was detailed in Section 1.2.2. In Section 1.3, the current knowledge of forced ignition and the numerical methods for ignition processes, including spark models, were reviewed. The initiation of a flame kernel through energy deposition was presented in Section 2.3.2. From this, it appears that forced ignition involves a multitude of processes, from the initiation of a kernel of flame to the flame stabilization within the whole combustion system. Hence, the choice of a modeling approach in investigating forced ignition phenomena is closely related to the ignition process or processes that are the focus of the investigation. Thus, energy deposition models are required for investigating the effects of spark energy or spark duration, as well as arc tracking models for investigating the effects of the turbulent flow on the formation of a flame kernel [50, 164, 38].

Within this work, the probabilistic convection and growth of an established kernel of flame are the focus. Hence, time-resolved simulations have been performed. The statistical convection of kernels as well as the flow conditions over the kernel surface are investigated by monitoring Lagrangian particles that are representative of ignition events. The computational particles are seeded into the turbulent inert flow. Hence, the effects of thermal expansion due to combustion on the flow are not considered. The great advantage of this method is that it allows the monitoring of multiple ignition events simultaneously and therefore performing statistical analysis based on ensemble averaging. The method has been applied in the context of spark ignited methane-air jet experimentally investigated by Ahmed and Mastorakos [5]. The modeling is further presented in detail in Section 5.2, together with the results.

Ignition is initiated by a region of fully burned gases centered at the spark location. This region is representative for an established flame kernel. It will interact with the turbulent flow and lead to ignition by flame propagation over its surface. The generation of the kernel is instantaneous and no spark energy is considered. These approximations are consistent with the approach consisting in investigating the interaction of the turbulent flow with an established flame kernel. Indeed, in a sufficiently large kernel, the heat release due to combustion is higher than the spark energy. This approach has been applied for calculating ignition sequences with LES, for example in [167]. For performing LES of ignition, other investigations applied a hot jet [16] or a source term in the energy equation [104, 105, 162].

3.3 Modeling Turbulence-Chemistry Interaction

As presented in Section 3.1, the modeling of turbulent flows using RANS or LES implies the resolution of averaged or filtered values rather than instantaneous ones. In particularly, unclosed source terms, $\widetilde{\dot{\omega}_\phi}$, appear in the transport equations of scalar, ϕ, in RANS and in LES context, Eq. 3.11 and Eq. 3.34, respectively. These unclosed terms in the averaged or filtered balance equations are closed through resolved variables or model approaches. However, the resolution of the mean or filtered chemical source term for a progress variable is not straight forward due to the non-linearity of chemical reactions. Thus, modeling approaches are applied to determine this term, based on the laminar chemical kinetics and the resolved or time averaged quantities.

A variety of combustion models have been proposed to account for the effect of turbulence on combustion. For detailed information, consult the books of [131] and [139] or the reviews by [88] and [14]. In the following paragraphs two combustion models are introduced. First, the Eddy-Break-Up approach is presented. Second, a probability density function model with progress variable approach is presented. This method is applied to couple the thermochemical properties that have been solved analytically for laminar configurations in a preprocessing step to the turbulent flow. All investigations documented in this work have been performed applying this last modeling.

3.3.1 Eddy Break-Up Model

Based on the argument that chemical reaction rate is controlled by mixing processes, Spalding [159] introduced a RANS closure for the turbulent mean reaction rate of the progress variable Y, $\widetilde{\dot{\omega}_Y}$, following an eddy break-up (EBU) approach. Thus, $\widetilde{\dot{\omega}_Y}$ is ex-

pressed as:

$$\widetilde{\dot{\omega}_Y} = C_{EBU}\bar{\rho}\frac{\sqrt{\widetilde{Y''^2}}}{t_{EBU}}, \tag{3.75}$$

where t_{EBU} represents a turbulent mixing time which can be calculated as $t_{EBU} = k/\varepsilon$ and $\sqrt{\widetilde{Y''^2}}$ the variance of the progress variable. Assuming thin premixed flames and subsequently a bimodal distribution of burned and unburned fuels, the variance reads: $\widetilde{Y''^2} \approx \widetilde{Y}(1-\widetilde{Y})$

The model can be extended to account for finite rate chemistry replacing the constant C_{EBU} by an Arrhenius approach. Defining a sub-grid scale mixing time based on the sub-grid scale turbulent energy, the EBU approach can be extended to LES. An extended version of the EBU model, including two-step finite-rate chemistry for combustion of methane, was investigated (Section 4.1.3). Although this idea has not been further followed in the frame of ignition, the EBU model is introduced here for illustration purposes.

3.3.2 Probability Density Function Approach

The basic idea of the probability density function (PDF) approach is to perform averaging based on the statistical distribution of a comprehensive set of controlling parameters. Indeed, for a turbulent premixed flame satisfying the conditions of the Shvab-Zeldovich formalism, each infinitesimal probability, $P(f,c)dfdc$, of a couple of mixture fraction and progress variable, (f,c), corresponds a reaction rate, $\omega_Y(f,c)$. The index Y here is used for denoting the non-scaled progress variable. Indeed, while the thermochemical properties derived from pre-computed flames are stored in a look-up table using a normalized progress variable, c, a transport equation is solved for the non-scaled progress variable, Y. The scaling factor, Y_{eq}, is stored in the table. Thus, knowledge of the density weighted joint PDF of mixture fraction and progress variable, $\widetilde{P}(f,c)$, at a space-time coordinate yields a statistical distribution of the reaction rate $\dot{\omega_Y}$, based on pre-computed laminar premixed flames, that can be integrated to obtain the mean reaction rate.

$$\dot{\omega_Y} = \dot{\omega_Y}(f,c) \tag{3.76}$$

$$\widetilde{\dot{\omega_Y}} = \int_{f,c} \dot{\omega_Y}(f,c)\widetilde{P}(f,c)dfdc \tag{3.77}$$

The case of a turbulent premixed flame has been described for illustration purpose. Nonetheless, PDF-modeling is a general method that can be applied for multiple variables. The advantage of this statistical description is to provide a closure for the mean or filtered reaction rate based on pre-computed flames. However, the joint-PDF still needs

to be closed. Therefore, two different approaches are commonly applied. PDF can be explicitly calculated by resolving a PDF-transport equation. On the other hand, presumed distribution form can be assumed. Although the method of transported PDF is more accurate, especially when strong turbulence chemistry effects are expected, the method of presumed PDF is popular for technical applications thanks to the low computational cost. In the following, the method of presumed PDF is presented with more detail. More information concerning PDF methods can be found in the book by Pope [140] and in the review by Haworth [75].

Presumed PDF

A presumed probability density function is defined by the first statistical moments of the distribution and an analytical function defines the form. Generally the first and second moments, or mean and variance, are used. The usual distribution functions used for representing presumed form consist of simple Dirac distributions, Gaussian distributions and, most frequently, distributions defined by a β-function. The use of β-functions is detailed further in this section. To represent a joint PDF of multiple variables, a further assumption for separating the variables is applied.

Hence, in the context of the FGM model, the joint PDF, $\widetilde{P}(f,c)$, is first approximated by assuming statistical independency between the mixture fraction and the normalized progress variable, Eq. 3.78. Indeed these variables are uncorrelated in the limit of infinitely fast chemical reaction.

$$\widetilde{P}(f,c) = \widetilde{P}(f) \times \widetilde{P}(c|f) \approx \widetilde{P}(f) \times \widetilde{P}(c) \tag{3.78}$$

Second, the form of each PDF is defined. Within this work, a β-distribution has been applied to define the distribution of the mixture fraction, while both Dirac (δ) and β-distributions have been used to describe the progress variable distribution. Thus, the joint PDF, $\widetilde{P}(f,c)$, is assumed as:

$$\widetilde{P}(f,c) \approx \widetilde{P}_{\beta,\widetilde{f},\widetilde{f''^2}}(f) \times \widetilde{P}_{\beta \text{ or } \delta,\widetilde{c},\widetilde{c''^2}}(c), \tag{3.79}$$

where the variance, defined by: $\widetilde{f''^2} = \widetilde{f^2} - \widetilde{f}^{\,2}$, is used for parametrizing the distribution form.

The β-distribution was introduced by Borghi [17] for describing mixing. It is parameterized by two shape parameters, a and b as:

$$\widetilde{P}(f) \approx \widetilde{P}_{\beta,\widetilde{f},\widetilde{f''^2}}(f) = \frac{1}{B(a,b)} f^{a-1}\left(1-f\right)^{b-1}. \tag{3.80}$$

The parameters a and b are functions of the values of mean and variance, such as:

$$a = \widetilde{f}\gamma, \tag{3.81}$$

$$b = \left(1-\widetilde{f}\right)\gamma, \tag{3.82}$$

where

$$\gamma = \frac{\widetilde{f}\left(1-\widetilde{f}\right)}{\widetilde{f''^2}} - 1. \tag{3.83}$$

The density function is normalized by the β-function, B, which reads:

$$B(a,b) = \int_0^1 f^{a-1}\left(1-f\right)^{b-1} df \tag{3.84}$$

Finally, the mean value of a scalar ϕ is calculated according to:

$$\widetilde{\phi}(\widetilde{f},\widetilde{f''^2},\widetilde{c},\widetilde{c''^2}) = \int_{f,c} \phi(f,c)\widetilde{P}_{\widetilde{f},\widetilde{f''^2}}(f)\widetilde{P}_{\widetilde{c},\widetilde{c''^2}}(c)df\,dc. \tag{3.85}$$

The β-distribution forms a family of continuous probability distributions, which allows the description of near-bimodal distributions representative of flows with high levels of non-premixedness as well as bell-shaped distributions that are more or less peaked and representative for flows with more or less high level of premixedness, as displayed in Figure 3.2.

A Dirac distribution has also been applied for the progress variable. Following the idea of Bray et al. [25], the statistical distribution is defined by the probabilities of encountering unburned, burned or an intermediate state. This intermediate state corresponds to the mean $\widetilde{c}$. The probabilities are defined so as to retrieve the first and second statistical moments:

$$P(0) = \frac{\sigma}{\widetilde{c}}, \tag{3.86}$$

$$P(\widetilde{c}) = 1 - \frac{\sigma}{\widetilde{c}(1-\widetilde{c})}, \tag{3.87}$$

$$P(1) = \frac{\sigma}{(1-\widetilde{c})}, \tag{3.88}$$

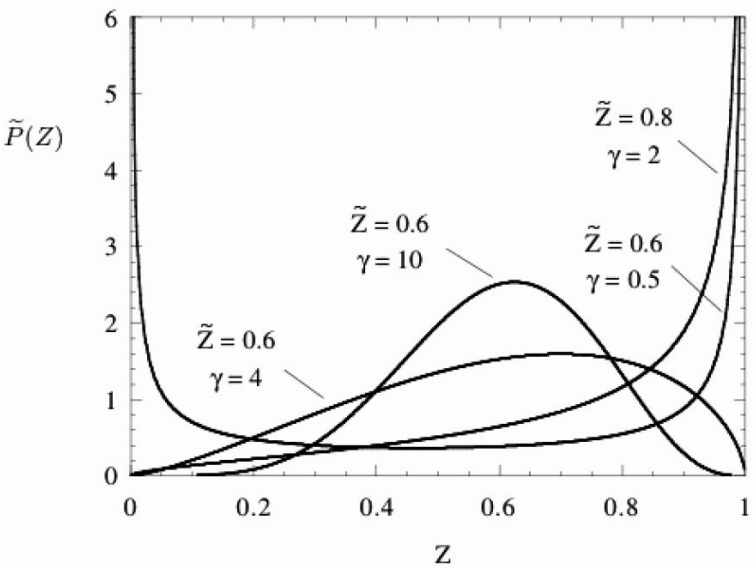

Figure 3.2: Shapes of the presumed PDF following a β-distribution of scalar Z in [131]

where $\sigma = \sqrt{\widetilde{c''^2}}$ is the standard deviation.

Hence, knowing the form of the PDF distribution, it is possible to apply the integration procedure described in Eq. 3.77 for pre-computing the averaged thermochemical properties corresponding to any given flow conditions, that are defined by the means and variances of the two controlling variables $(\widetilde{f}, \widetilde{f''^2}, \widetilde{c}, \widetilde{c''^2})$. By varying these four parameters, the ensemble of statistical flow conditions encountered in a two-inlets configuration can be mapped. Thus, a pre-computed four-dimensional look-up table is calculated to access the averaged thermochemical properties for turbulent reactive flows. While the two-dimensional FGM look-up table was introduced in Section 3.2.3 for laminar configurations, the four-dimensional FGM look-up table for turbulent reactive flow is formally defined as:

$$\widetilde{\psi}_{FGM} = \widetilde{\psi}(\widetilde{f}, \widetilde{f''^2}, \widetilde{c}, \widetilde{c''^2}). \tag{3.89}$$

For more complex probability distributions, the integration of sub-grid terms based on a presumed form may be inaccurate. Comparison of presumed PDF and transported PDF was performed, for example by Kuehne et al. [103] using a hybrid LES/Monte-Carlo transported-PDF approach for simulating a non-premixed bluff-body stabilized CH_4/H_2 flame.

The four values, $\widetilde{f}$, $\widetilde{f''^2}$, $\widetilde{c}$ and $\widetilde{c''^2}$, necessary for presuming the PDF form are obtained from the modeled balance equations of $\widetilde{f}$ and $\widetilde{f''^2}$ and of the non-scaled variables $\widetilde{Y}_c$ and

$\widetilde{Y_c''^2}$. According to the filtered balance equation Eq. 3.37 these equations read:

$$\frac{\partial(\bar{\rho}\widetilde{f})}{\partial t} + \frac{\partial\left(\bar{\rho}\widetilde{f}\widetilde{u}_i\right)}{\partial x_i} = \frac{\partial}{\partial x_i}\left(\bar{\rho}\left(\frac{\nu}{Sc} + \frac{\nu_t}{Sc_t}\right)\frac{\partial\widetilde{f}}{\partial x_i}\right), \tag{3.90}$$

$$\frac{\partial(\bar{\rho}\widetilde{f''^2})}{\partial t} + \frac{\partial\left(\bar{\rho}\widetilde{f''^2}\widetilde{u}_i\right)}{\partial x_i} = \frac{\partial}{\partial x_i}\left(\bar{\rho}\left(\frac{\nu}{Sc} + \frac{\nu_t}{Sc_t}\right)\frac{\partial\widetilde{f''^2}}{\partial x_i}\right) - 2\bar{\rho}\widetilde{N_f}, \tag{3.91}$$

$$\frac{\partial(\bar{\rho}\widetilde{Y_c})}{\partial t} + \frac{\partial\left(\bar{\rho}\widetilde{Y}_c\widetilde{u}_i\right)}{\partial x_i} = \frac{\partial}{\partial x_i}\left(\bar{\rho}\left(\frac{\nu}{Sc} + \frac{\nu_t}{Sc_t}\right)\frac{\partial\widetilde{Y}_c}{\partial x_i}\right) + \widetilde{\dot{\omega}_Y}, \tag{3.92}$$

$$\frac{\partial(\bar{\rho}\widetilde{Y_c''^2})}{\partial t} + \frac{\partial\left(\bar{\rho}\widetilde{Y_c''^2}\widetilde{u}_i\right)}{\partial x_i} = \frac{\partial}{\partial x_i}\left(\bar{\rho}\left(\frac{\nu}{Sc} + \frac{\nu_t}{Sc_t}\right)\frac{\partial\widetilde{Y_c''^2}}{\partial x_i}\right) - 2\bar{\rho}\widetilde{N_Y} + 2\widetilde{Y_c'\dot{\omega}_Y'}, \tag{3.93}$$

where $\widetilde{\dot{\omega}_Y'}$ is the chemical source term. It is pre-computed according to Eq. 3.85 and stored in the look-up table. The variance source term due to chemical reaction $\widetilde{Y_c'\dot{\omega}_Y'}$ is decomposed into $\widetilde{Y_c'\dot{\omega}_Y'} = \widetilde{Y_c\dot{\omega}_Y} - \widetilde{Y}_c\widetilde{\dot{\omega}_Y}$. The term $\widetilde{Y_c\dot{\omega}_Y}$ is needed. It also pre-computed according to Eq. 3.85 and stored in the look-up table. $\widetilde{N_f}$ and $\widetilde{N_Y}$ are the scalar dissipation rates of f and Y_c. Each term is the sum of a resolved and a sub-grid part:

$$\widetilde{N_f} = \widetilde{N_{f\,res}} + \widetilde{N_{f\,sgs}}, \tag{3.94}$$

$$\widetilde{N_Y} = \widetilde{N_{Y\,res}} + \widetilde{N_{Y\,sgs}}. \tag{3.95}$$

The resolved terms read:

$$\widetilde{N_{f\,res}} = -\left(\frac{\nu}{Sc} + \frac{\nu_t}{Sc_t}\right)\frac{\partial\widetilde{f}}{\partial x_i}\frac{\partial\widetilde{f}}{\partial x_i}, \tag{3.96}$$

$$\widetilde{N_{Y\,res}} = -\left(\frac{\nu}{Sc} + \frac{\nu_t}{Sc_t}\right)\frac{\partial\widetilde{Y}_c}{\partial x_i}\frac{\partial\widetilde{Y}_c}{\partial x_i}. \tag{3.97}$$

The sub-grid terms are modeled assuming a linear relaxation of the variance within the sub-grid [106, 113].

$$\widetilde{N_{f\,sgs}} = \frac{\nu_t}{\Delta^2}\widetilde{f''^2}, \tag{3.98}$$

$$\widetilde{N_{Y\,sgs}} = \frac{\nu_t}{\Delta^2}\widetilde{Y_c''^2}. \tag{3.99}$$

The term $\frac{\Delta^2}{\nu_t}$ represents a characteristic mixing time scale. Within the CFD code, the scaled control variables are retrieved according to the scaling rules described by Landenfeld

[106]:

$$\widetilde{c} \approx \widetilde{\left(\frac{1}{Y_{eq}}\right)} \widetilde{Y}_c, \tag{3.100}$$

and

$$\widetilde{c''^2} \approx \widetilde{\left(\frac{1}{Y_{eq}}\right)}^2 \left(\widetilde{Y_{eq}''^2} + \widetilde{Y_c''^2} - 2\sqrt{\widetilde{Y_{eq}''^2}}\sqrt{\widetilde{Y_c''^2}} \right). \tag{3.101}$$

The terms $\widetilde{(1/Y_{eq})}$, $\widetilde{(1/Y_{eq})}^2$ and $\widetilde{Y_{eq}''^2}$ are pre-computed according to Eq. 3.85 and stored in the look-up table.

In the context of RANS calculations, the modeled equations are alomost identical. The only difference is that the unresolved scalar dissipation rate is obtained using ε/k as a characteristic mixing time scale.

The code also allows the solution of a balance equation for the scaled progress variable $\tilde{c}$ and its variance $\widetilde{c''^2}$. However, the implementation does not include additional terms that result from the mixture fraction dependency of the progress variable value at equilibrium Y_{eq}. A discussion about the use of both methods is given in Section 5.1.4.

The major advantage of applying presumed PDF is the possibility of performing the integration of a look-up table in a pre-processing step and to directly retrieve all thermo-chemical properties during the CFD calculations from the values of four parameters that define the local statistical properties within the turbulent reactive flow. When applying FGM modeling to non-premixed or partially premixed configurations, it should be kept in mind that diffusion in mixture fraction space is not accounted for in the libraries of premixed laminar flamelets and homogeneous autoigniting reactors.

4 Numerical Treatment

The purpose of this chapter is to describe the details of the numerical treatments applied within this work. The numerical implementation of differential equations is based on the partition of the computational domain into smaller volumes of finite size. The CFD code PRECISE-UNS used within this work is described in Section 4.1. In particular, Section 4.1.3 summarizes the main contributions of the author to the code development and validation. Dealing with flow simulations, the *Finite Volumes Method* is generally used to express the governing equations in a discretized formulation within a computational cell. This method, which is applied within PRECISE-UNS, is introduced in Section 4.2.1. The partitioning of the computational domain as an unstructured mesh is described in Section 4.1.1. Sections 4.2.2 and 4.2.3 present the approximation of convective and diffusive fluxes, respectively. The numerical treatment applied for the analytical resolution of premixed flames was introduced in the previous section together with the respective modeling descriptions (Section 3.2.3). Section 4.5.2 introduces the numerical treatment used for the analytical resolution of autoigniting homogeneous reactors, as well as the numerical set-up used for computing autoignition.

4.1 CFD Code PRECISE-UNS

As mentioned in the introduction, Section 1.2.1, lean burn combustion concepts imply complex air-fuel mixing and therefore complex combustor geometries. The meshing of such geometries with multiple block structures is laborious. Thus, it was decided within Rolls-Royce to develop an unstructured code, PRECISE-UNS (*Predictive-System for Real Engine Combustors - Unstructured*). Since 2007, the code has been developed in collaboration with the institute Energy and Power Plant Technology (EKT) of Darmstadt University. It is a finite volumes CFD code for low-Mach number flows. The code is based on Dolfyn, an open-source code written in Fortran90. The original CFD code is owned by the consultancy company *Cyclone Fluid Dynamics BV* and can be downloaded from the website: `www.dolfyn.net`. Dolfyn is an unstructured code. It means that it can deal with numerical grids that are not necessarily structured, unlike the current Rolls-Royce in-house code for combustion PRECISE-MB (*Predictive-System for Real Engine Combustors - MultiBlocking*). The code is parallelized using MPI (Message Passing Interface)

environment and ParMETIS, an MPI-based parallel library for grid partitioning. All the simulations presented in this work were performed using the CFD code PRECISE-UNS.

4.1.1 Unstructured Computational Grid

Unlike structured meshes that consist of block structures of hexahedral cells with Cartesian coordinates, unstructured computational grids consist of a juxtaposition of polyhedral cells. Thus, unstructured meshes are more flexible and can be generated automatically, using methods such as *advancing front method* or *Delaunay triangulation*. See [150], [165] or [26] for more information on grid generation.

However, Cartesian indexation of the cells is not possible. The storage of the grid consists of several lists, a list of cells and a list of faces, among others. These lists are generated by a preprocessing program, which is able to read geometry input files compatible with the commercial CFD code StarCD. The lists are then concatenated into a geometry data file (**.geo*), that can be read by the CFD code. Although the cells do not have Cartesian coordinates as in structured meshes, the indices of both cells neighboring a face are stored within the face list. Hence, the values of the scalars are explicitly retrieved to evaluate the convective and diffusive fluxes in each cell (Sections 4.2.2 and 4.2.3).

4.1.2 Solving the Linear System of Equations

After a linear system of equations has been defined through the discretization of the system of differential equations, the next step consists of setting up a matrix corresponding to the linear system. Since only neighboring cells are directly coupled within the discretized equations, only a few terms are non zero within the matrix. Using structured mesh, the system results in a multi-diagonal matrix. This property can be used to improve the convergence rate. For example, the Stone's approach of the *incomplete lower-upper* (ILU) method [61] provides an efficient solver for seven-diagonal matrices.

Using unstructured mesh yields a sparse matrix without recognizable structures. Although such matrices are not representative of grid geometries, *algebraic multigrid* (AMG) methods allow the enhancement of the convergence rate. The method is based on a hierarchy of grids with different levels of refinement. These grids are constructed directly from the system matrix and do not have any geometrical meaning. Within the calculations, HYPRE [80], an open-source package for solving large, sparse linear systems of equations on massively parallel computers was applied in combination with an AMG method. More precisely, a four-level multigrid V-cycle coupled with an iterative Gauss-Seidel procedure

was used to solve the pressure correction equation (see section 4.4). To solve the easier equations for scalar transport, a *bi-conjugate gradient square stabilized* (Bi-CGSTAB) algorithm, as proposed by H.A. van der Vorst [170], was applied. More information concerning numerical methods for linear algebra can be found in [27, 61, 73, 150].

4.1.3 Code Development and Validation

Since 2007, various validation works have been carried out, some of which have been documented in masters theses conducted at EKT TU Darmstadt [97, 26, 66, 128]. Within the frame of the code development for this work, efforts have been focused on the following points.

- First, a two-steps finite-rate chemistry EBU model for combustion of methane (Section 3.3.1) was implemented into PRECISE-UNS. The original model, as avalaible in PRECISE-MB, was extended with an enthalpy equation. The underlying idea is twofold. Firstly, it introduces the possibility of accounting for heat exchange with the evaporating spray. Secondly, spark energy deposition can be modeled as a source term in the enthalpy equation. Hence, further extension of the approach to reduced chemistry models with limited steps numbers would possibly allow the simulation the kernel growth. The two versions of the model, with and without enthalpy equation, could be successfully verified. Therefore the coaxial jet swirl combustor configuration of Spadaccini et al. [158], also investigated with LES and a progress variable approach in [136], was simulated with PRECISE-MB and PRECISE-UNS. Although, comparison of the results attests to proper implementation, the capability of the approach to accurately capture the physics involved in the generation of a flame kernel or in the interaction between a flame front and an evaporating spray was doubted. Hence, the EBU approach was not further considered in the frame of ignition.

- The FGM combustion model (Section 3.2.3) was extended and validated for capturing autoignition phenomena. It includes the definition of a new progress variable and of a new repartition of the nodes in the look-up table, the transport of non-scaled progress variable and the scaling rules between scaled and non-scaled progress variables. This work is presented in Section 5.1.

- The validation of LES for non reactive flows has been principally performed within a master's thesis. Applying the Smagorinsky model (Section 3.1.3), Breitenberger [26] investigated the following cases on both tetrahedral and Cartesian grids: (i) the temporal kinetic energy decrease of a Taylor Green Vortex, (ii) the turbulent flow induced by a secondary motion within a square duct and (iii) the air/air jet

experimentally investigated by Ahmed [2]. To verify the implementation of Germano dynamic procedure (Section 3.1.3), this sub-grid stress modeling was applied later on to the square duct and to the air/air jet, both on hexahedral grids.

- To validate combustion LES with FGM modeling, simulations of Sandia Flame D were performed. These results are not presented in this work, since these simulations are not directly related to ignition. Preliminary investigations including a systematical study of density jump transport, and some results of Sandia Flame D have been documented in a master's thesis [128].

- Parallelized modules for forced ignition monitoring have been implemented and applied: (i) to monitor the evolution of ignited kernels and (ii) to monitor Lagrangian particles and the flow conditions surrounding these particles that are representative of convected flame kernels (Section 5.2.3).

4.2 Discretization in Space

4.2.1 Finite Volume Method

As introduced in Section 2.1 the general balance equation for an arbitrary scalar ϕ is expressed in a localized formulation as:

$$\frac{\partial(\rho\phi)}{\partial t} + \frac{\partial\left(\rho\phi u_i\right)}{\partial x_i} - \frac{\partial}{\partial x_i}\left(\rho D_\phi \frac{\partial\phi}{\partial x_i}\right) = \dot{\omega}_\phi, \tag{4.1}$$

where the terms represent the accumulation rate, the convective term, the diffusive term and the source term. In a control volume δV, the balance equation reads:

$$\int_{\delta V} \frac{\partial(\rho\phi)}{\partial t} dV + \int_{\delta V} \frac{\partial\left(\rho\phi u_i\right)}{\partial x_i} dV - \int_{\delta V} \frac{\partial}{\partial x_i}\left(\rho D_\phi \frac{\partial\phi}{\partial x_i}\right) dV = \int_{\delta V} \dot{\omega}_\phi dV. \tag{4.2}$$

Applying Gauss' theorem convective and diffusive terms are expressed as fluxes over the control surface $S = \partial\left(\delta V\right)$, of the volume δV as:

$$\int_{\delta V} \frac{\partial(\rho\phi)}{\partial t} dV + \int_{S} \rho\phi u_i n_i dS - \int_{S} \rho D_\phi \frac{\partial\phi}{\partial x_i} n_i dS = \int_{\delta V} \dot{\omega}_\phi dV, \tag{4.3}$$

where n_i denotes the normalized surface normal vector.

In a control volume with a number of N_{faces} planar faces, the surface integrals are expressed as sums of convective (C), and diffusive (D) fluxes over the faces f. The finite

volume balance equation reads:

$$\int_{\delta V} \frac{\partial(\rho\phi)}{\partial t} dV + \sum_{f=1}^{N_{faces}} F_{f,C} - \sum_{f=1}^{N_{faces}} F_{f,D} = \int_{\delta V} \dot{\omega_\phi} dV. \tag{4.4}$$

4.2.2 Convective Fluxes

The convective fluxes in Eq. 4.4 are approximated as:

$$F_{f,C} \approx \rho_f \phi_f u_f S_f. \tag{4.5}$$

Thereby, the surface integral is evaluated using the midpoint rule:

$$\int_{S_f} \phi dS \approx \phi_f S_f. \tag{4.6}$$

The surface S_f of face f is a fixed geometry parameter. The values of density ρ_f, ϕ_f and normal-velocity u_f are not available at the face center and are obtained by interpolation from the neighboring cells. Therefore, different discretization methods are available within the CFD code.

Central Differencing Scheme (CDS)

The central differencing scheme (CDS) is a straight forward convection scheme, which consists of a linear interpolation of the value of a scalar ϕ_f at face center from both neighboring control volumes. Hence, knowing the scalar values at the centers of neighboring cells (P) and (N), the approximation of ϕ_f on an equidistant grid results in:

$$\phi_f = \frac{\phi_P + \phi_N}{2}. \tag{4.7}$$

On a non-equidistant, grid an interpolation parameter λ_f is available as a geometry parameter for performing linear interpolation:

$$\lambda_f = \frac{x_f - x_P}{x_N - x_P}, \tag{4.8}$$

$$\phi_f = \lambda_f \phi_N + (1 - \lambda_f)\phi_P. \tag{4.9}$$

For non-smooth grids, the face center and the centers of the neighboring control volumes are not necessarily on a line, as represented in Figure 4.1. The linear interpolation of ϕ_f is performed at the location of point x'_f. However, the approximation of ϕ_f is corrected

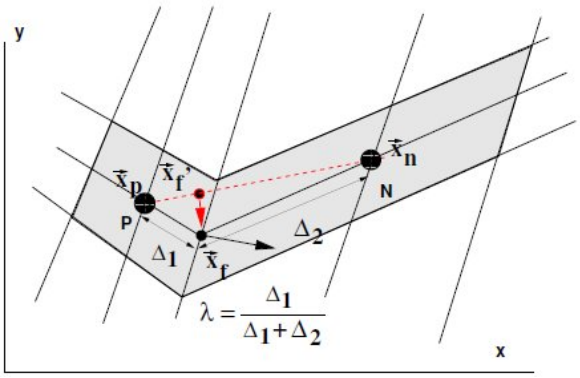

Figure 4.1: Linear interpolation at face center on a non-orthogonal grid, with gradient-based correction, see [102]

evaluating the gradient of ϕ_f at the location of x'_f and considering the vector $\overrightarrow{x'_f x_f}$, which is known. The CDS convection scheme is second order accurate and attention has to be paid to possible numerical oscillations. In particular, the generation of an initial LES turbulent flow field may be difficult with CDS.

Upwind Differencing Scheme (UDS)

The upwind differencing scheme (UDS) is a first order accurate convection scheme. The term "upwind" refers to the weighting that is applied when approximating a scalar value at the face center. Indeed, the face value is simply approximated as being equal to the value at the upstream control-volume center. The UDS convection scheme does not induce oscillations and is numerically stabile. However, the low order truncation error results in a rather large artificial reduction of the scalar gradients and smoothing of the scalar fields. This phenomenon acts as an additional artificial diffusion and is referred to as numerical diffusion. Since combustion in general is driven by diffusion processes, the UDS convection scheme is not likely to give accurate results. Within turbulent calculations, numerical diffusion has a damping, stabilizing effect and tends to laminarize the flow. This effect may be beneficial for convergence. Hence, in this work a blending of 90% CDS and 10% UDS was applied to generate an initial flow field before switching to 100% CDS.

Convection of Bounded Scalars

The use of the central differencing method as second order convection scheme for bounded scalars, such as mixture fraction and progress variable, may induce oscillations leading to local scalar values that are not consistent with the physical meaning of these scalars. To prevent this numerical phenomenon, a convection scheme that respects scalar boundedness has been applied. This convection scheme is called MinMod. It relies on

the definition of a convective boundedness criterion which is calculated on each face for each scalar. It considers the scalar gradient on the upstream side and compares it to the scalar difference on both neighboring points of the face divided by the distance between these two points. Following the local value of this criterion, second order CDS is applied where oscillations can be excluded, a blending between CDS and the first order bounded scheme UDS is applied at locations of moderate tendency for oscillations, while UDS is applied where the criterion indicates an oscillatory behavior.

4.2.3 Diffusive Fluxes

The diffusive fluxes in Eq. 4.4 are approximated as:

$$F_{f,D} \approx \rho D_\phi \left[\frac{\partial \phi}{\partial x_i}\right]_f n_{i,f} S_f. \tag{4.10}$$

To evaluate the scalar gradients $\left[\frac{\partial \phi}{\partial x_i}\right]_f$ on the faces f, the gradients are first appromixated at the cell centers by considering the scalar values at the neighboring cell centers and following a least mean square procedure. The scalar gradients are then interpolated on the faces f, as in Eq. 4.9.

$$\left[\frac{\partial \phi}{\partial x_i}\right]_f = \lambda_f \left[\frac{\partial \phi}{\partial x_i}\right]_N + (1-\lambda_f)\left[\frac{\partial \phi}{\partial x_i}\right]_P. \tag{4.11}$$

4.3 Advancing in Time

4.3.1 Time Integration

To approximate the accumulation rate in Eq. 4.4 two implicit methods are available. Using an *Implicit Euler Method* the time derivative $\frac{\partial \phi}{\partial t}$ is evaluated at the next time level t_{n+1} as:

$$\left.\frac{\partial \phi}{\partial t}\right|_{n+1} \approx \frac{\phi^{n+1} - \phi^n}{\Delta t}, \tag{4.12}$$

where Δt represents the time-step. The time derivative can also be approximated by differencing a parabola forced through solutions at three time levels t_{n-1}, t_n and t_{n+1} [61]. This method, referred to as *Three Time Levels Method* (TTL) reads:

$$\left.\frac{\partial \phi}{\partial t}\right|_{n+1} \approx \frac{3\phi^{n+1} - 4\phi^n + \phi^{n-1}}{2\Delta t}. \tag{4.13}$$

Both available schemes are implicit and require iteration at each time-step. However, the density is calculated explicitly at each iteration within a time-step following the mixing or combustion model. The implicit Euler scheme is first order accurate, while the three time levels scheme is second order accurate in time. Within LES calculations, both schemes can be blended to smooth the flow field while generating an initial field. However, second order (pure TTL scheme) was preferred for preventing excessive damping of high frequencies.

4.3.2 Time-Step Stability Constraint

Regarding stability, the CFL number (*Courant-Friedrichs-Lewy Number*) represents the general stability criteria for discretization schemes. It is defined as:

$$CFL = \frac{u \cdot \Delta t}{\Delta x}, \tag{4.14}$$

where u is mean convection speed, Δt the time-step and Δx the control volume length. The CFL number illustrates how many control volumes a given scalar is propagated through within a time-step. For example, the explicit Euler time integration method is known to be stable for CFL numbers below one. Implicit schemes, such as the TTL scheme, are in general unconditionally stable, but the time integration error rises significantly for CFL numbers bigger than one. Moreover, the code is not fully implicit as the density integration follows a semi-explicit scheme - see Section 4.4. For these reasons, calculations are restricted to a CFL number below one. This criteria results in a limitation of the time-step. The CFL number is evaluated locally. The location with the maximum CFL number determines the admissible time step. Typically, the maximum CFL number is reached in regions with high velocity flow and small control volume sizes, such as a region surrounding a flow inlet.

4.4 Pressure-Velocity Coupling

In the assumption of low Mach Number flows, the absolute value of the pressure does not appear in the governing equations. Only the pressure gradient influences the flow as a force. However, the pressure field can be calculated indirectly using mass conservation law, once a pressure level is determined at a reference location. The method is referred to as SIMPLE method (*Semi-Implicit Method for Pressure Linked Equation*). It was published by Patankar [130] and is widely used for incompressible flows. The procedure consists of guessing the pressure field and applying a correction loop to guarantee mass conservation. Therefore pressure and velocities are first splitted into prediction $.^*$ and correction $.'$ parts, as:

$$p = p^* + p' \tag{4.15}$$

and

$$u_i = u_i^* + u_i'. \tag{4.16}$$

These splitting expressions are introduced into the discretized momentum equations and yield three relationships between pressure and velocity correction terms [61, 150]. Introducing these relationships into the discretized mass conservation equation yields a pressure correction equation that can be solved to determine the correction term p', see [61, 150]. The SIMPLE procedure is summarized as follows:

1. Use the pressure field at previous time step as an approximation for pressure p^*,
2. Solve the momentum equations to compute an intermediate velocity field u_i^*,
3. Compute the mass fluxes at the cell faces,
4. Solve the pressure correction equation providing the correction term p',
5. Correct the mass fluxes at the cell faces,
6. Correct the velocities at cell centers $u_i = u_i^* + u_i'$,
7. Update pressure $p = p^* + p'$,
8. Repeat steps two to seven until convergence of the time-step.

The ".*" mark indicates that the mass conservation is not achieved at this stage.

Within the code PRECISE-UNS, pressure and velocities are evaluated at the same location. For such co-located variable arrangements, the use of simple linear interpolation would not permit elimination of alternating velocity and pressure fields. Thus, the technique introduced by Rhie and Chow [145] was applied within step 3 to interpolate the velocities at the face centers. Hence, the coupling of pressure and velocities fields is ensured for co-located arrangements within the pressure correction loop. More information on the pressure correction equation, the SIMPLE procedure and the Rhie and Chow interpolation technique can be found in [61, 150].

4.5 Numerical Treatment of Autoignition

Section 3.2.4 introduced the chemical reaction of methane autoignition, as well as its modeling with kinetics mechanism. The requirements for an adequate progress variable have also been described. Here, the computation of the autoignition of a homogeneous methane-air mixture is presented for illustration purposes. This section is dedicated to the analytical resolution procedure and to the setting-up for autoignition.

4.5.1 Advancing in Time

In perfectly stirred reactors the scalars distribution is homogeneous; there are no gradients and no scalar transport due to convection or diffusion. Hence, the transport equation for a species α Eq. 3.39 reduces to the sole concentration accumulation rate balanced by the chemical source term:

$$\rho \frac{\partial Y_\alpha}{\partial t} = \dot{\omega_{Y_\alpha}}. \tag{4.17}$$

The numerical resolution is achieved by applying a Newton iterative method involving the Jacobi matrix J relative to the source term and defined as:

$$J_{i,j} = \frac{\partial \dot{\omega_{Y_i}}}{\partial Y_j}. \tag{4.18}$$

Using vectorial notations, Eq. 4.17 can be rewritten in a discretized form, following a forward Euler method:

$$\rho \frac{Y^{t+\Delta t} - Y^t}{\Delta t} \approx \dot{\omega_Y}(t + \Delta t). \tag{4.19}$$

Recognizing that

$$\dot{\omega_Y}(t + \Delta t) \approx \dot{\omega_Y}(t) + J(t) \left(Y^{t+\Delta t} - Y^t \right), \tag{4.20}$$

and injecting this expression into the discretized equation yields:

$$\left(\frac{\rho}{\Delta t} I - J \right) \left(Y^{t+\Delta t} - Y^t \right) \approx \dot{\omega_Y}(t), \tag{4.21}$$

where I is the identity matrix. Hence, the composition space at time $t + \Delta t$ is obtained explicitly as:

$$Y^{t+\Delta t} = Y^t + A^{-1} \dot{\omega_Y}(t), \tag{4.22}$$

where A^{-1} is the inverse of matrix $\left(\frac{\rho}{\Delta t} I - J \right)$.

The numerical resolution is performed using a dedicated code called *Ignite*. It should be noted that this had never been applied before, although it has been provided. An adaptive time stepping is applied in combination with the Newton iterative method. The code is written in Fortran and widely makes use of Chem1D libraries [33]. In particular, the composition space at equilibrium is obtained using the *equil* routine of Chem1D. The computation of the thermodynamic properties at equilibrium relies on the minimization of the Gibbs free energy. It is a standard problem in optimization, referred to as constrained minimization. The method applied for solving this problem consists of a Newton iteration procedure. More information concerning the numerical procedure for solving the equilibrium can be found in [71].

4.5.2 Setting-Up Autoignition Computations

Although the numerical code for homogeneous reactors *Ignite* was provided, it had never been used before. To start with the code, a methane-air mixture with a mixture fraction of 0.045, at 900 K and 40 bar was considered. Figure 4.2 shows the curves of the scaled progress variable, the scaled methane concentration and temperature. An ignition delay of 152 ms was obtained. It is defined as the time for which the temperature reaches 950 K = 900 K + 50 K. The logarithmic scales for progress variable and fuel should be noted. It demonstrates the exponential nature of autoignition. Applying the empirical law given by Eq. 3.55 yields a delay time of 13.5 ms. The difference of one order of magnitude does not undermine the code implementation. Indeed, the pressure and temperature conditions are outside the domain of trust of both the empirical law and the GRI mechanism. The predicting capability of the code is demonstrated in Section 5.1.4.

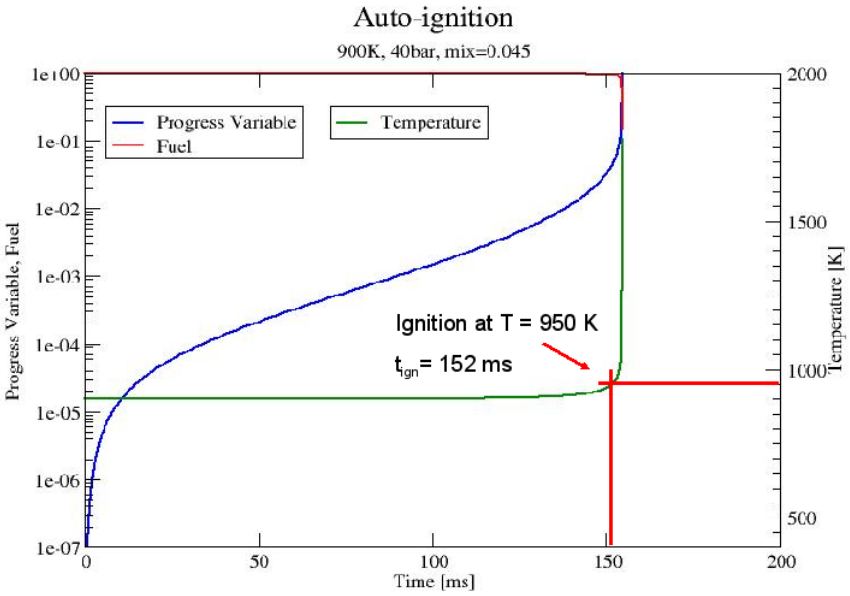

Figure 4.2: Autoignition of a methane-air mixture (mixture fraction=0.045, 900 K, 40 bar). Blue curve shows the exponential growth of the scaled progress variable, red is for the scaled fuel concentration and green for temperature.

To apply FGM formalism to autoignition, the results are saved as a function of the progress variable, according to Eq. 3.70. Therefore, the progress variable was defined as the sum of the concentrations of carbon monoxide and dioxide, as in [48]. Chemical equilibrium is first calculated to define the maximum value of the progress variable. A grid that is based on the scaled progress variable is then defined for storing the results

during the calculation. Within the code, this is implemented as two embedded loops. The external loop is run through as many times as storage nodes are defined. The internal loop consists of small computational time steps that are adaptively defined to guarantee a given convergence criteria. The progress variable node values are used as breaks for the internal loop.

Figure 4.3 displays this grid, where 50 storage nodes are distributed logarithmically from $10.^{-15}$ to 1 (green curve). The x-axis shows the external iterations steps from 1 to 50. The red curve displays the total time in a linear scale in ms, while the blue curve shows the physical time between two storage nodes (external loop) in a logarithmic scale in ms. The time steps displayed here only represent the physical time between two storage nodes. They do not influence the accuracy of the computation, since each step consists of much smaller computational time steps.

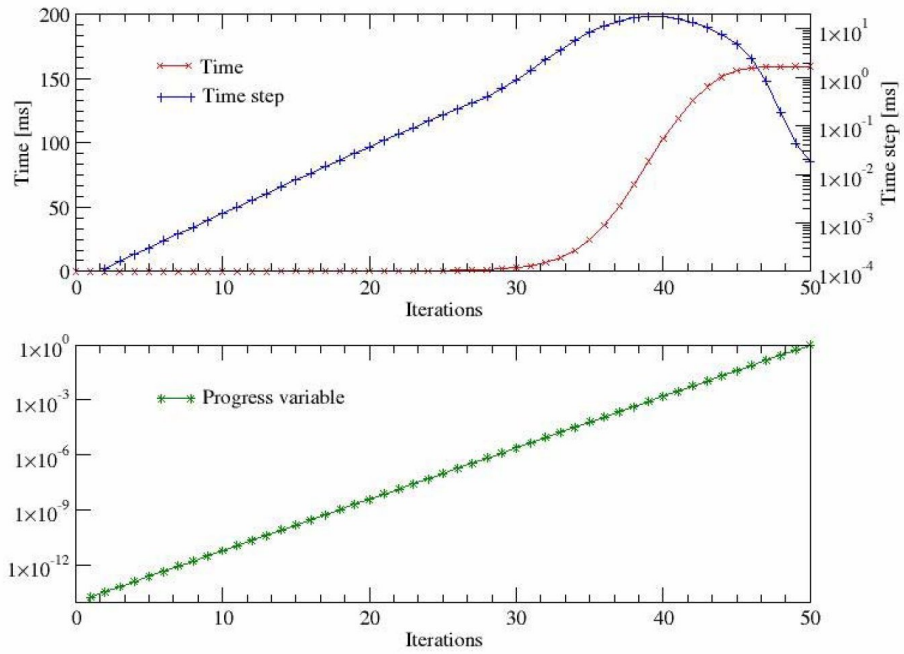

Figure 4.3: Adaptive time-stepping and storage grid

From Figure 4.3, it can be recognized that, for this example, the domain of scaled progress variable $c < 10^{-7}$ is not significant (iteration steps smaller than 30). Indeed, the physical time spent in this domain of extremely low product concentrations is extremely short. Hence, it is not necessary to store the thermochemical state in this domain. The computational time is not affected by the definition of the lowest progress variable value

to store, since the computation is started from a progress variable value of 0 and internal time-steps are defined adaptively and independently of the node values.

Although the storage size for one-dimensional autoigniting reactors is small, a more efficient storage grid was defined for further investigations. The domain of progress variable: $10^{-7} < c < 0.1$, corresponding to the build-up of radicals, was mapped with a geometric distribution of 100 nodes. The domain of progress variable: $0.1 < c < 1$, corresponding to heat release and thermal expansion, was linearly mapped with 100 nodes. Hence, interpolation errors during the integration of the look-up table could be reduced to a minimum for both phenomena. The choice of the progress variable, that was further applied, is discussed in the preliminary investigations to the autoigniting jet in Section 5.1.2. The integration of the look-up table for capturing the particularities of autoignition is also discussed.

5 Applications

This chapter presents the results obtained with two model burner configurations. Section 5.1 is dedicated to autoignition. A turbulent methane-air jet flame autoigniting in a hot coflow is considered to evaluate the autoignition prediction capability of the model in inhomogeneous and turbulent mixtures using RANS calculations. This study also aims to investigate the method's potential to model forced ignition as a heat deposition, resulting in local autoignition of the mixture. Section 5.2 focuses on LES of forced ignition. A spark ignited methane-air jet configuration was investigated. The results consist of a statistical analysis of ignition probability and simulations of unsteady ignition events.

5.1 Autoigniting Non-Premixed Jet

The effects of turbulence on autoignition in inhomogeneous mixtures is a fundamentally important topic and crucial for the development of low NOx combustion systems, such as lean premixed pre-vaporized gas turbines. Modeling of simulated autoignition in turbulent flows, as presented in Section 3.2, is applied to a lifted methane jet flame autoigniting in a hot coflow, as experimentally investigated by Cabra et al. [29]. The modeling couples the detailed chemistry of autoigniting homogeneous reactors (Section 3.2.4) with a progress variable approach derived from the FGM model (Section 3.2.3) and with a turbulence-chemistry interaction modeling based on presumed PDF (Section 3.3).

While the configuration has been the focus of numerical investigations using both LES (Domingo et al. [48], Jones and Navarro-Martinez [90]) and RANS (Gordon et al. [69]), only a few detailed parametric numerical studies designed to improve understanding and control of the autoignition process have been conducted (e.g. Michel et al. [124]).

Gordon et al. [69] investigated the stabilization mechanism of an autoigniting flame based on transport budgets of chemical species. Whereas propagating flames are stabilized by diffusion through the flame front, they found that ignition as a result of diffusion along the streamline is negligible compared to convection and reaction contributions. Thus, they demonstrated that the flame is stabilized by autoignition. The study here investigates the potential for modeling with tabulated chemistry, based on autoigniting homogeneous

reactors, to account for the stabilization mechanism of an autoigniting lifted flame. The methodology, once successful, will then be applied to LES. Modeling of forced ignition as a heat deposition resulting in local autoignition of the mixture could then be considered.

The burner and the configurations investigated are detailed in Section 5.1.1. Section 5.1.2presents the preliminary investigations: (i) the computation of the detailed chemistry of autoigniting homogeneous reactors, (ii) the definition of an adequate progress variable, (iii) the coupling with the CFD code, and (iv) the set-up for modeling turbulence chemistry interaction.
The investigated cases and the numerical set-up for CFD calculations are presented in Section 5.1.3. The results for the jet configuration are presented and discussed in Section 5.1.4. Section 5.1.5 contains conclusions on the model's capability in accounting for the effects of turbulence on autoignition in inhomogeneous mixtures.

5.1.1 Configuration

The Vitiated Coflow Burner

The Vitiated Coflow Burner The model burner was designed at the University of California, Berkeley for investigating flames stabilized in combustion products. The burner is referred to as the Vitiated Coflow Burner (VCB) and is described in details on the Berkeley website [11]. It has a central jet and a coflow issuing through a perforated plate. Figure 5.1 displays a picture of the burner built at Berkeley. Experiments with hydrogen-nitrogen [28] and methane-air [29] jets have been performed. A replica of this burner has been constructed at the University of Sydney and investigated, particularly in [68, 69, 70]. Although a spray nozzle can be seen on the picture, a gaseous fuel jet was used in this work.

The fuel jet has an inner diameter of $d_j = 4.57\ mm$ and an outer diameter of 6.35 mm. The coflow diameter is 210 mm and the nozzle exit height above the perforated plate surface is 70 mm. A water-cooled collar surrounds the coflow. It delays the entrainment of ambient air into the coflow region. The brass plate is perforated with 2200 holes of 1.58 mm diameter. Each of these holes acts as a flame holder for a lean premixed hydrogen-air jet flame. The hot vitiated coflow is generated by the reaction products of these flames.

Methane-Air Jet Experimental Set-up

Figure 5.2(a) shows a schematic of the configuration using a methane-air jet. Figure 5.2(b) is a picture of a lifted methane jet flame. The reacted coflowing gas allows the

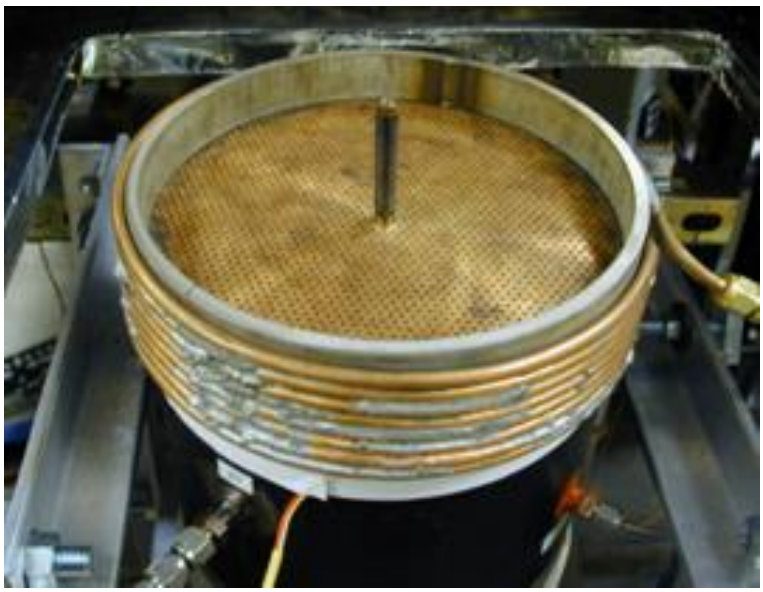

Figure 5.1: The Berkeley vitiated coflow burner, fitted with a spray nozzle [11].

investigation of stabilized flames in combustion products in a wide range of conditions. In particular, it introduces the possibility of autoignition as a stabilization mechanism.

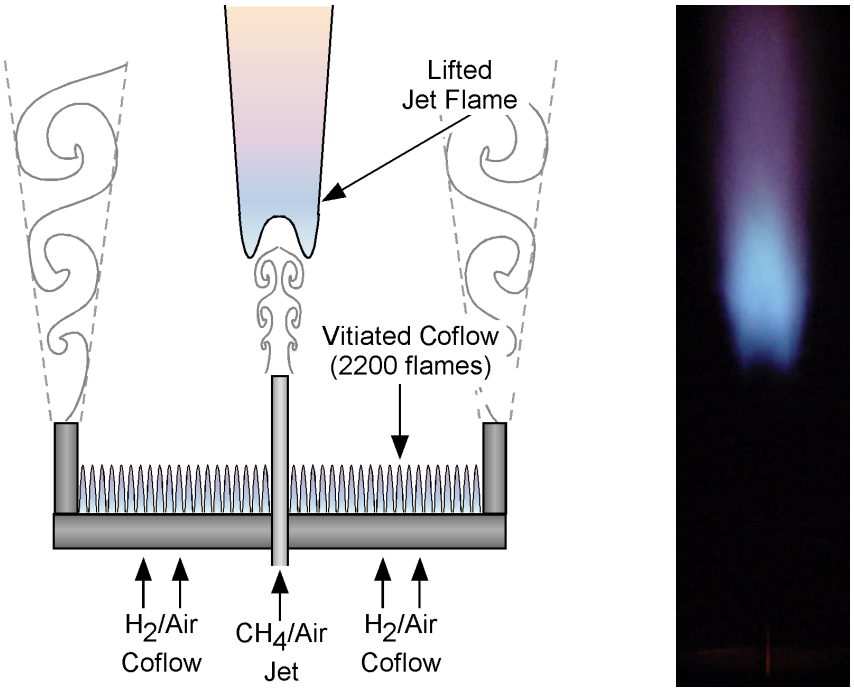

Figure 5.2: (a) Schematic of the VCB with a methane-air jet [11]. (b) Picture of an autoigniting methane flame [11].

Cabra et al. [29] performed multiscalar point measurements from combined Raman-Rayleigh-LIF experiments for a base-case methane-air jet. The jet consists of a mixture of 33% CH_4 and 67% air by volume. The bulk velocity of the fuel jet was $V_{jet} = 100\ m/s$. The vitiated coflow consists of reaction products of a lean premixed H_2-air flame with an equivalence ratio of $\phi = 0.4$. The coflow bulk velocity of $V_{coflow} = 5.4\ m/s$ was determined from measured flow rates. Details of experimental conditions for the base case are listed in Table 5.1.

Base case [29]	Jet	Coflow
Re	28000	23300
d [mm]	4.57	210
V [m/s]	100	5.4
T [K]	320	1350
X_{O_2}	0.15	0.12
X_{N_2}	0.52	0.73
X_{H_2O}	0.0029	0.15
X_{CH_4}	0.33	0.0003

Table 5.1: Base-case conditions for the autoigniting methane-air jet [11, 29]

The lifted height was sensitive to the inflow parameters. It was measured with a simple digital imaging system in both [29] and [69], using visible chemiluminescence as a flame front indicator (Figure 5.2(b)). Cabra et al. [29] measured the liftoff height against the jet velocity, coflow velocity and the coflow temperature. Gordon et al. [69] investigated liftoff height against coflow temperature, using the Sydney replica of the burner. Although they obtained consistent results for sensitivity, a significant difference in the absolute height was measured. However, this result is in the range of the absolute accuracy of the thermocouples used for measuring the coflow temperature, which is up to 4% (50 to 60 K). Moreover, the flame base was stable for low lifted height, while it became fluttery with increasing height.

The temperature and species profiles were uniform across the hot coflow [29]. Since the flow field of interest is unaffected by mixing with ambient air, the jet configuration can be computationally treated as a two-stream problems. Hence, the FGM formalism for autoignition in two-stream turbulent configurations is used.

5.1.2 Preliminary Investigations

Section 3.2 describes, how the FGM model can be applied to autoignition, based on the computation of the autoignition of homogeneous reactors. Section 4.5.2 introduces

the computation set-up. In this section, preliminary investigations are presented. They consist of the two following points:

- Computation of the detailed chemistry of autoigniting homogeneous reactors relevant to the burner configuration. This points includes the definition of an adequate progress variable, that is able to reproduce the different stages of autoignition and includes the comparison of ignition delays to the results in [29].
- The integration of the results into an adequate look-up table and subsequent coupling with the CFD code.
- Ignition delays are calculated for a set of autoigniting homogeneous reactors and compared to the results from detailed chemistry.

Detailed Chemistry of Autoignition

The autoigniting flamelets were calculated in a constant pressure perfectly-stirred reactor, using the GRI-3.0 mechanism [153] for methane, over a range of autoigniting mixture fractions. The method described in Section 4.5.2 was applied in the initial setting-up of the computations. After consideration of the chemical species concentrations, the role of the following species was recognized: CH_3, CH_2O, HO_2, CO and CO_2. More precisely, the initiation of autoignition was characterized by the predominance of the concentration of CH_3 among the species that were originally not present in the mixture. This result is consistent with the initiation described by the two steps Eq. 3.56 and Eq. 3.57. Further on in the induction process, the radicals CH_2O and HO_2 could be identified as predominant (Section 3.2.4). Just before ignition, the concentration of CO increases. Finally, full oxidation of the fuel results in the decrease of these intermediate species and the increase of CO_2, conforming to the hierarchical carbon chain described in Section 3.2.4.

In order to reproduce the chemical stages in autoignition, the progress variable has been defined as the sum of the concentration in mol/g (or $Kmol/Kg$ using SI units) of these radicals and combustion products:

$$Y_c = [CH_3] + [CH_2O] + [HO_2] + [CO] + [CO_2]. \tag{5.1}$$

In mapping the whole domain of mixture fraction found in the jet, the calculations should be performed for a range of mixture fractions including very lean mixtures. For equivalence ratios less than 0.1, the heat release is less than 50 K. Hence, a new ignition criterion should be defined for determining the autoignition delay. In [29], ignition was considered as reached at a heat release of 50% of the total heat release. In this work, a new ignition criterion based on 50% of the progress variable was preferred for coding

convenience. For mixture fractions allowing a temperature increase higher than 50 K, it was verified that both criteria, $T_{ign} = T + 50\ K$, and, $c_{ign} = 0.5$, yield very close results for ignition delays. This is due to the steep curve of the reaction once ignition is achieved. Thus, it is reasonable to compare results obtained with $c_{ign} = 0.5$ with those in [29], based on a heat release of 50%.

On the other side of the mixture fraction range, more cold fuel results in a lower mixing temperature for the non-reacted gas. Consequently, ignition more delayed. Computational time is increased. No low limit value of the mixing temperature can be directly derived to determine if a mixture will autoignite or not. However, it was found that autoignition could be computed for increasing mixture fractions until the corresponding non-reacted mixing temperature reaches values typically in the order of 860 K.

Figure 5.3 shows the ignition delay against equivalence ratio, ϕ, in a log-log scale. The red curve displays the results calculated by Cabra et al. [29] for a coflow temperature T_c of 1350K, also using the GRI3 mechanism but with a different code. The green and the blue curves display the delays calculated with the 0-D integration code (IGNITE) for coflow temperatures of 1350 K and 1430 K, respectively. For an equivalence ratio, $\phi > 0.01$, the delays are in good agreement with results in [29]. These results corroborate that the new code Ignite has been correctly implemented. For very lean mixtures, $\phi < 0.01$, differing definitions of ignition, 50% heat release versus $c = 50\%$, are expected to yield discrepancies in ignition delays. For both coflow temperatures, the ignition delays are at a minimum at lean mixtures, while the delay increases with an increasing proportion of cold fuel. The layers with an equivalence ratio between 0.01 and 0.1 are the most reactive, with delays of 5 to 6 ms for $T_c = 1350\ K$ and 2 to 3 ms for $T_c = 1430\ K$. However, the temperature increase due to combustion is less than 50 K for $\phi < 0.1$.

As in [69], other kinetics mechanisms in Chemkin format were tested. It was not possible to predict ignition delays using skeletal mechanism [87]. Delays were reasonably well predicted in the domain of near stoichiometric mixture fractions using the Smooke mechanism [155]. However, this mechanism yields ignition delays that were too long (one order of magnitude) for an equivalence ratio of 0.1.

Look-up Table Setting and CFD Coupling

Prior to the CFD computations of autoigniting reactors, a four-dimensional look-up table was integrated. Special attention was paid to the distribution of points in the look-up table. The following paragraphs introduce: (i) the node distribution for the mixture

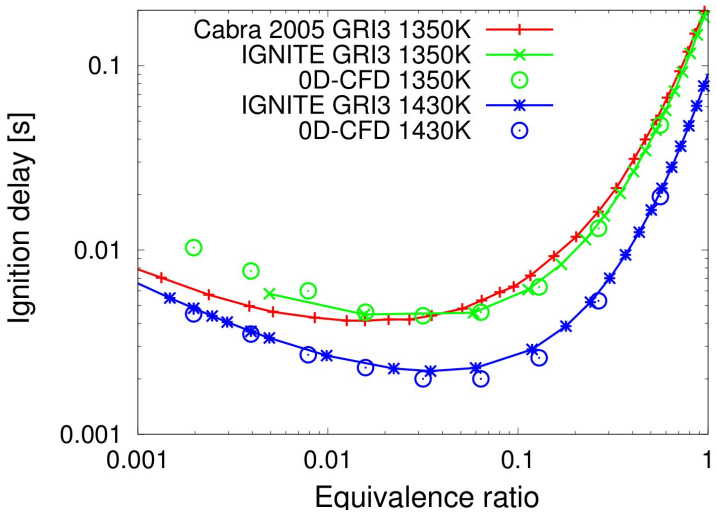

Figure 5.3: Ignition delay against equivalence ratio in a log-log scale.

fraction, (ii) the node distribution for the progress variable, and (iii) the node distributions and scaling rules for the variances.

As displayed in Figure 5.3, the most reactive layers are very lean to lean: $0.01 < \phi < 0.1$. This domain of mixture fraction is expected not to play an important role in combustion of methane at ambient temperatures. Hence, a linear distribution of the mixture fraction nodes is generally applied for FGM in PRECISE-MB. A new nodes distribution with better refinement in the domain of lean mixtures was applied to reduce interpolation errors in the domain of the most reactive layers. Therefore, the method introduced in [183] was followed. A variable η is defined as:

$$\eta = \frac{f_s}{f_s + f}, \tag{5.2}$$

where $f_s = 0.17$ is the stoichiometric mixture fraction. An equidistant grid for η results in a grid for mixture fraction f that is dense near stoichiometry and in lean regions. The nodes with the lower and higher mixture fraction values correspond to an equivalence ratio of 0.01 and to the limit of autoignition described previously, respectively.

The nodes distribution should also be modified for the progress variable. Indeed, the exponential nature of autoignition was demonstrated in Section 4.5.2. Because of these results, a grid with a geometric distribution for the domain $10.^{-7} < c < 0.1$ and a linear distribution for the domain $0.1 < c < 1$ was applied, in a similar way to the node distribution applied for storing the autoignition flamelets.

The variances of mixture fraction and progress variable are necessary to describe the turbulence-chemistry interaction. The standard settings were used for both variances. It consists of an equidistant grid for the variables $\widetilde{f''^2}^{1/2.5}$ and $\widetilde{Y_c''^2}^{1/1.2}$.

Within the CFD code, explicit functions are applied to directly access the interpolation nodes within the look-up table. Hence, new distribution functions were implemented for the mixture fraction and progress variable.

Reproduction of Ignition Delay with CFD

To validate the model's capability to predict ignition delay, the time dependent behavior was computed with PRECISE-UNS in homogeneous reactors for coflow temperatures of 1350 K and 1430 K. A look-up table with 25, 25, 15 and 15 nodes for mixture fraction, progress variable and both variances combined, respectively, was first computed. The CFD results are displayed in Figure 5.3. For $\phi > 0.01$, the ignition delay is well reproduced. For leaner mixtures, the progress variable source term is extrapolated linearly. As the induction process is essentially exponential, the delay for very lean mixtures increases linearly with decreasing ϕ in the log-log scale. For $T_c = 1350\ K$, this results in an overestimation of the delay time, while the extrapolation does not introduce noticeable discrepancies for $T_c = 1430\ K$. Since the temperature increase due to combustion is negligible for such lean mixtures, it is assumed that it does not influence the CFD results.

These preliminary results demonstrate the model's capability to reproduce ignition delays for homogeneous reactors. In the following section, a turbulent jet is investigated.

5.1.3 Numerical Set-Up

The numerical set-up and investigated cases are described in this section. The main objective is to simulate a lifted flame and investigate the liftoff height and its sensitivity to the coflow temperature, as performed in [69] using transported PDF. Thus, the investigated cases were chosen. Hence, a coflow temperature of 1355 K is chosen as base case (Table 5.2. Emphasis is also put on a configuration with a coflow temperature of 1430 K.

Making use of the axi-symmetry of the configuration, the computational domain was defined as a quasi two-dimensional mesh. The implementation of the finite volume methods requires three-dimensional computational domains. In this case, an orthogonal mesh was generated. A sector of 8 angle degrees with 3 cells in radial direction was considered. The mesh contains 460 cells in the axial direction and 115 in the radial one, which approximates 160,000 cells. A section is displayed in Figure 5.4. The horizontal lower line

represents the configuration's axis. The computational domain has been chosen as in [69]. The coflow inlet is located 70 mm below the jet inlet. The radial extent is 91.4 mm.

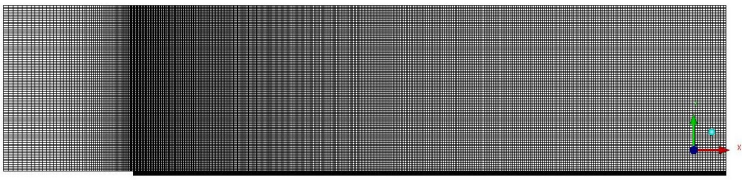

Figure 5.4: Quasi-2D orthogonal mesh with 460 cells in the axial direction and 115 in the radial direction

Calculations were preformed both with a progress variable, defined as a scaled value $\tilde{c}$, and as a non-scaled value $\widetilde{Y}_c$, using RANS and $k-\varepsilon$ model. The effects of both treatments are discussed in Section 5.1.4. In a non-scaled progress variable, both β and δ presumed PDF have been applied The results are also discussed in Section 5.1.4.

The boundary conditions were chosen as per [69] (Table 5.2). Uniform velocity profiles were considered. Since FGM modeling does not account for heat exchange, at least in the case of two-stream flows, heat transfer with the steel fuel tube should be neglected here, whereas it was considered in [69].

Inlet boundaries base-case [69]	Jet	Coflow
V [m/s]	100	5.3
T [K]	320	1355
k $[m^2s^{-2}]$	150	0.11
ε $[m^2s^{-3}]$	66050	5.6

Table 5.2: Inlet boundaries for the base-case configuration investigated here and in [69]

5.1.4 Results and Discussion

First, radial profiles of mixture fraction and temperature are compared to the experiment. Secondly, the stabilization mechanism of the lifted flame is analyzed. The treatment of the progress variable as a scaled or non-scaled value is discussed. Then, the sensitivity to the coflow temperature is presented for both Dirac and β-PDF and compared to experiments. Finally, a conclusion about the method's capability is drawn.

Mixture Fraction and Temperature Fields

Figure 5.5 displays radial profiles of mean and root mean square deviation (rms) values of mixture fraction (left) and of temperature (right). The experimental results are given in [29] for a coflow temperature of 1350 K. For this temperature, an average liftoff height of 35 d was found by digital imaging of the luminous flame base. In the work here, ignition location was defined as the most upstream location with a temperature increase higher than 50 K compared to mixing temperature. Using a non-scaled progress variable and a β-PDF for both mixture fraction and progress variable, lifted flames were obtained for coflow temperatures of 1355 K and 1430 K, with liftoff height of 49 d and 35 d, respectively. The radial profiles are compared to those from experimental results.

The mixture fraction is predicted quite well until an axial position of 40 d. At this location, the experimental configuration is ignited, as it is in the 1430 K case as well. A temperature increase can be noticed at a radial position of 2 to 5 d, where near stoichiometric mixtures are found. For 1430 K, a temperature increase can only be noticed at a radial position of about 6 d, in the region of lean mixture fraction, including most reactive layers, while for 1355 K ignition is not yet reached.

Further downstream, a clear temperature increase is observed in lean mixtures for both simulations. However, the flame propagation towards rich mixtures on the jet axis is not correctly reproduced. This inaccuracy is directly related to the computation of the library of homogeneous autoigniting reactors, since no diffusion is accounted for. After ignition, the propagation of reaction across a mixing layer is complex. For a hydrogen-air constant-strain mixing layer, Mastorakos [118] demonstrated the presence of three reaction zones: one lean, one rich and one at stoichiometry. Hence, the advice in [118] is to simulate a laminar transient diffusion layer in either physical space or mixture fraction space, prior to investigating turbulent non-premixed autoignition. In the case here, the model's limitations are obvious and emphasis is put on the ignition in the most reactive layers and the subsequent stabilization mechanism. For the axial positions 50 d and 70 d, the radial profiles of mixture fraction are flatter than those in the experiment. The higher mixture fraction values for $r > 6$ d result in the higher equilibrium temperatures found in this region.

Fields of Chemical Species

The fields of progress variable are presented in mol/g for $T_c = 1355$ K in Figure 5.6(a), and for $T_c = 1430$ K in Figure 5.6(b). For qualitative considerations, the field of CO_2 for $T_c = 1430$ K in [69, 67] is displayed in Figure 5.6(c). At equilibrium the progress variable reduces to the specific mole number of CO_2 (Eq. 5.1). At the exception of the steeper

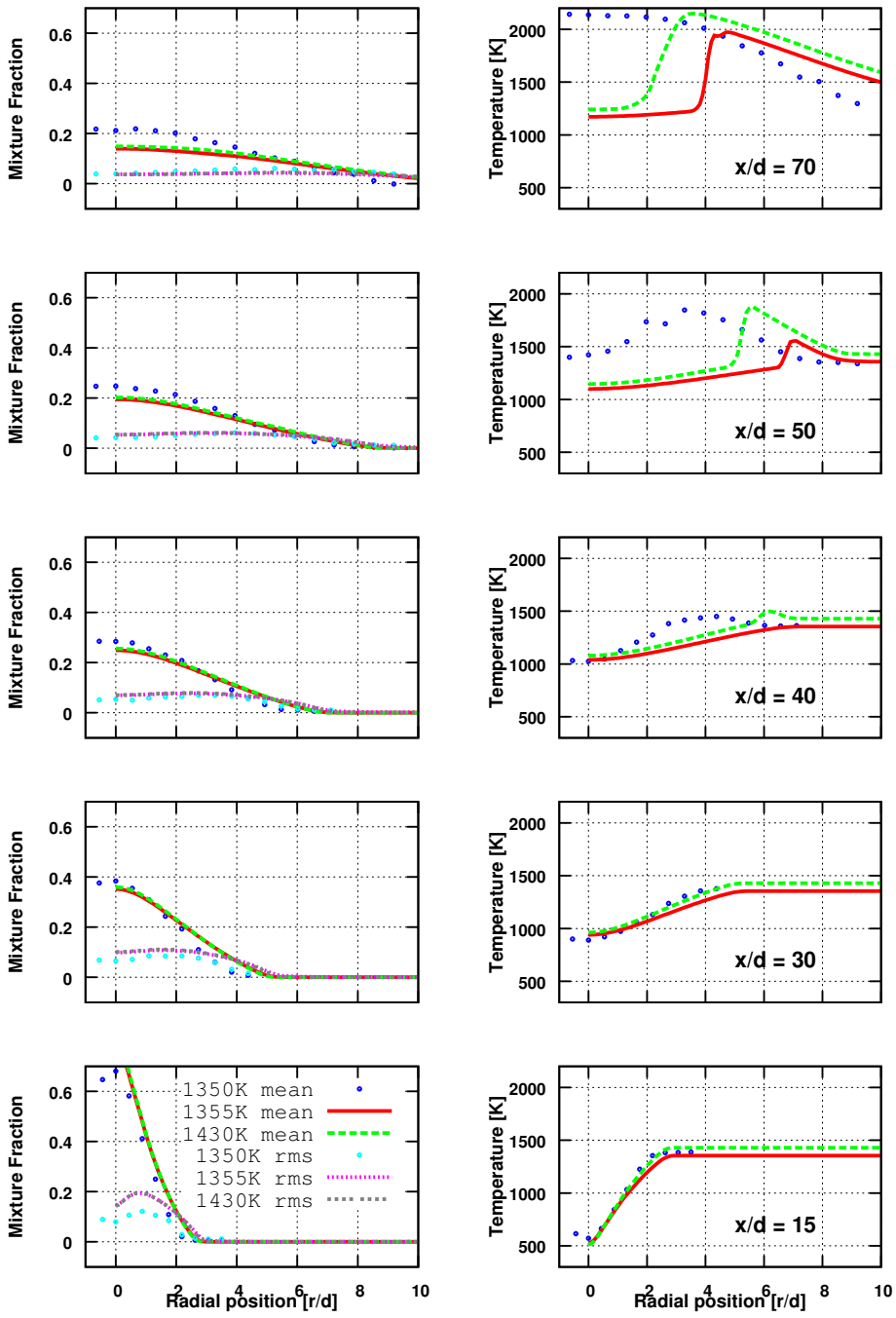

Figure 5.5: Radial profiles of (links) mixture fraction root mean square deviation and of (right) temperature, from experiment (points) with a coflow temperature of 1350 K [29] and numerical results (lines) for coflow temperatures of 1355 K and 1430 K.

flame front found in the inner cone, the results compare relatively well. The peak mass fraction of 0.088 g/g (0.00182 mol/g) is consistent with the value of 0.112 g/g found in [67].

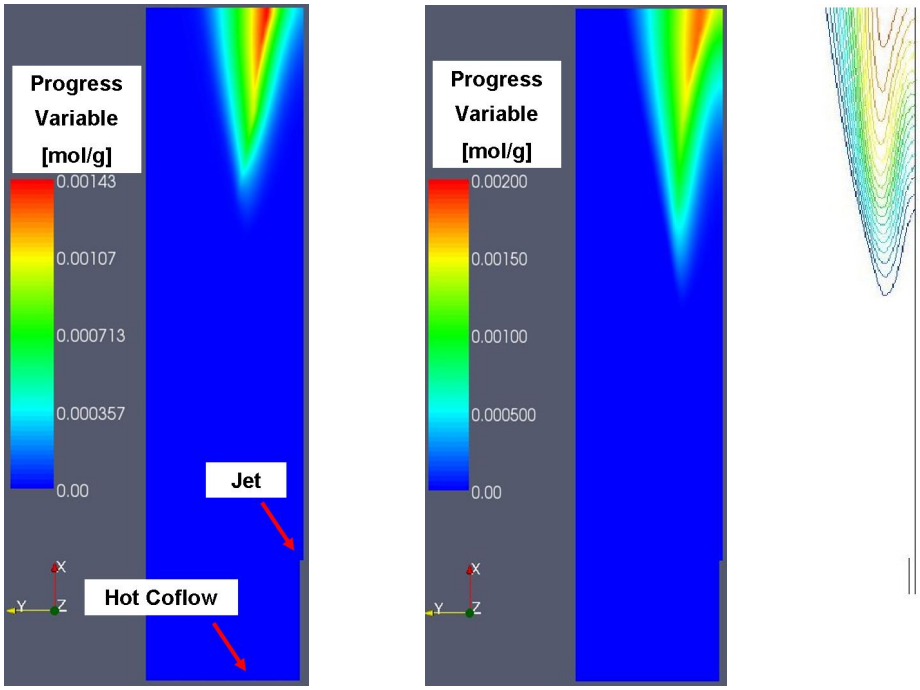

(a) (b) (c)

Figure 5.6: Field of progress variable Y_c in mol/g, for a coflow temperature (a) of 1355 K and (b) of 1430 K. (c) Field of CO_2 for the 1430 K case, showing a peak mass fraction of 0.112 g/g [67], or 0.00254 mol/g.

Figures 5.7(a) and (c) display the mass fraction fields of HO_2 and of CH_2O, respectively, for $T_c = 1430\ K$. Figures 5.7(b) and (d) display the mass fraction fields simulated in [69, 67]. In [69, 67], HO_2 is rapidly destructed after ignition. This is consistent with the results in [118] for a hydrogen-air mixing layer. In the investigations here, HO_2 is still found downstream of ignition, while the diffusion-reaction balance should dominate. As explained previously, this phenomenon is because diffusion is not considered in the modeling. However, the peak mass fraction of 1.9×10^{-5} g/g [67] is consistent with the mass fraction found before ignition, where diffusion in the streamline direction is negligible compared to convection and reaction ([69]). Similarly, the CH_2O peak mass fraction of 2.3×10^{-4} g/g [67] is consistent with the mass fraction found before ignition. Further downstream, the mass fraction is overestimated on the richer side, where a regime of flame propagation, characterized by diffusion-reaction is expected.

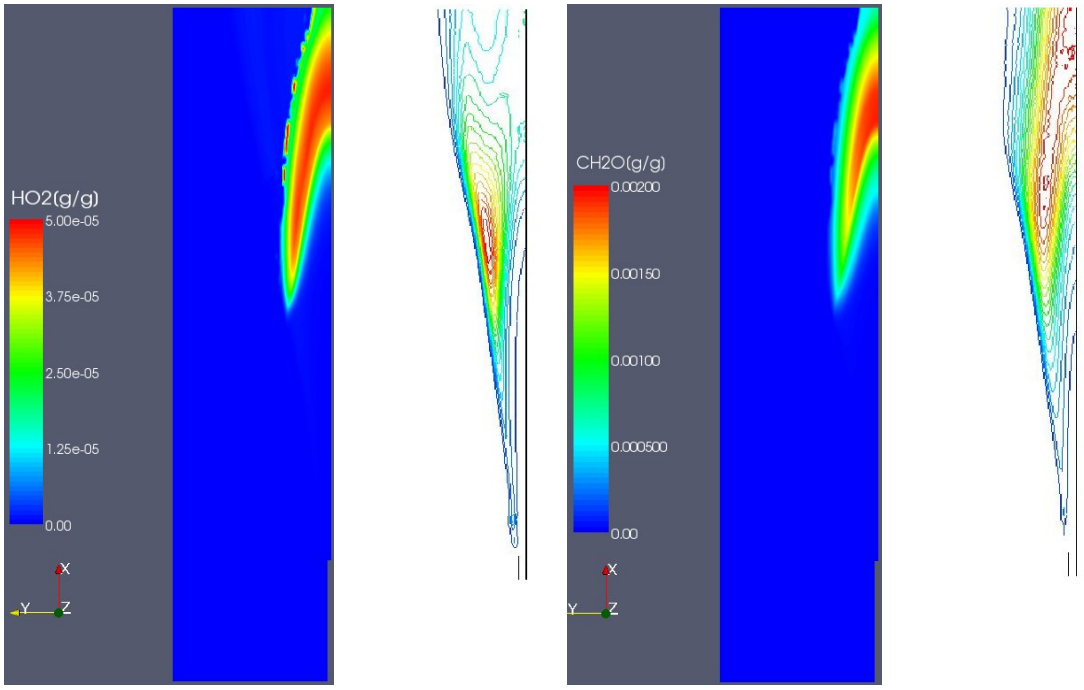

Figure 5.7: Fields of HO_2 concentration in g/g, for a coflow temperature of 1430 K (a) and (b) in [67] with a peak mass fraction of 1.9×10^{-5} g/g. Fields of CH_2O concentration in g/g, for a coflow temperature of 1430 K (c) and (d) in [67] with a peak mass fraction of 2.3×10^{-4} g/g.

Flame Stabilization

Gordon et al. [69] showed that axial diffusion is negligible in the flame base region in the transport budget of ignition precursors. It was demonstrated that the flame is stabilized by autoignition. The model's capability to account for the stabilization mechanism of an autoigniting lifted flame using tabulated chemistry based on autoigniting homogeneous reactors is investigating here. Therefore, the fields of the progress variable and of its source are displayed in Figures 5.8(a) and 5.8(b) for $T_c = 1355\ K$. The ignition location is represented by a star. It is defined as the most upstream point where the temperature increase due to chemical reaction reaches 50 K. The source field is shown in a log scale. It displays the slow nature of low temperature autoigniting processes accompanied by the build-up of a radical pool. The build-up leads to radicals and temperature runaway in the most reactive layers, followed by flame propagation towards the richer layers, where a significant increase in temperature and product species concentrations are observed.

To investigate the history of fluid elements along the streamline leading to ignition, the axial line passing through ignition location, $r = 7\ d$, is considered for $T_c = 1355\ K$. As

demonstrated in [69], this line is very similar to the streamline leading to ignition, giving insight into the history of the igniting fluid elements. Figure 5.9 displays the profiles of the equivalence ratio and residence time for $T_c = 1355\ K$ and for $T_c = 1430\ K$. The residence time t_r is defined as:

$$t_r(x) = \int_{25d}^{x} \frac{1}{v} dx', \tag{5.3}$$

where v is the local fluid velocity. Hence, t_r corresponds to the integrated residence time along the streamline. The equivalence ratio curves show that mixture fraction increases along the streamlines, as coflow fluid elements are convected and mixed with jet fuel. The locations of the most reactive layer, $0.01 < \phi < 0.1$, are reported on the curve of residence time. Thus, a residence time in this layer is displayed. For $T_c = 1355\ K$ a time of 5 ms is found. This time corresponds to the ignition delay in the most reactive layer as displayed in Figure 5.3. Similarly, a time of 3 ms is found for $T_c = 1430\ K$, which corresponds to the ignition delay in the most reactive layer.

At 39 jet diameters a source peak region is observed at very lean mixture fractions on the streamline leading to ignition. This source peak indicates that the mixture is reacting in the most reactive layers, whereas ignition is quenched where mixing with the cold jet is faster. A similar source field pattern is observed for $T_c = 1430\ K$, with a peak at 27 d. However, this source peak does not indicate the ignition location, since heat release in very lean regions is too low to ignite the colder rich regions. From an analysis of the experimental results of [29], Michel et al. [124] reported a PDF with bimodal distribution due to the mixing of burned lean mixtures with less reactive rich mixtures. In present study, the PDF of the progress variable takes a bimodal shape which is described by the β-PDF distribution. Thus, the high variance of the progress variable leads to a flame brush of 10 d before ignition is reached at 49 d. For $T_c = 1430\ K$ ignition is located at 35 d and corresponds to a flame brush of 7 d Such a flame brush is consistent with the results in [67], as it corresponds to the extent of the region of high HO_2 mass fraction displayed on Figure 5.7(b). Although statistically independent control variables were assumed, the bimodal shape of the progress variable results in a realistic flame brush prior to ignition.

Progress Variable Treatment

The previous section demonstrated the significance of mixing of lean reactive mixtures with richer less reactive ones in predicting flame stabilization. The scaled progress variable is a convenient marker for defining the state of a reactive mixture. However, additional terms appear in the transport equation. As pointed out in [24], these terms are often neglected in modeling studies. Investigations using a scaled progress variable demonstrated that this simplification is not valid for the configuration here. Although it was possible

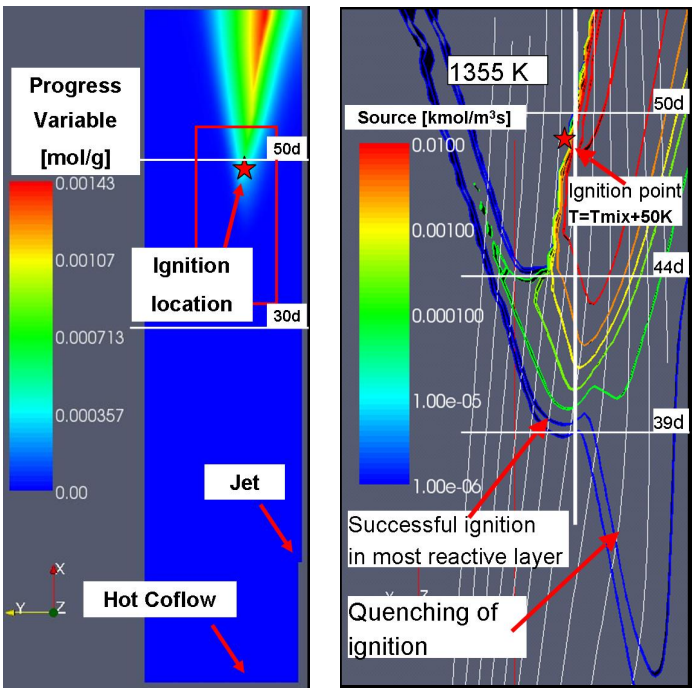

(a) (b)

Figure 5.8: (a) Field of progress variable in mol/g for $T_c = 1355\ K$ showing ignition location. (a) Field of progress variable source term in $kmol/m^3s$, ,magnification of the region around the ignition location.

to obtain a lifted flame, the stabilization mechanism was not realistic. In particular, the transport of the scaled progress variable without considering the functional dependency of the norm Y_{eq} on mixture fraction resulted in too high values of the progress variable, where partly reacted very lean reactive fluid was mixed with less lean fresh fluid. Thus, the transport of scaled progress variable did not allow the quenching of ignition to be captured, as displayed in Figure 5.8(b).

Sensitivity Analysis

The sensitivity of the liftoff height to changes in the coflow temperature was investigated in [29] and [69]. Although consistent results were obtained for sensitivity, discrepancies were found in the absolute value of the liftoff height due to inaccuracy in the measurement of the coflow temperature using thermocouples. The experimental and numerical results in [69] are presented in Figure 5.10. Computations have been performed for a β- and a Dirac-PDF. Coflow temperatures of 1355 K and 1430 K were applied for the β-PDF and of $T_c = 1355,\ 1380,\ 1405$ and 1430 K for the Dirac function (Section 3.3.2). For the β-PDF, liftoff was obtained, while the sensitivity was underestimated. The Dirac-PDF distribution did not allow correct reproduction of the bimodal nature of the ignition

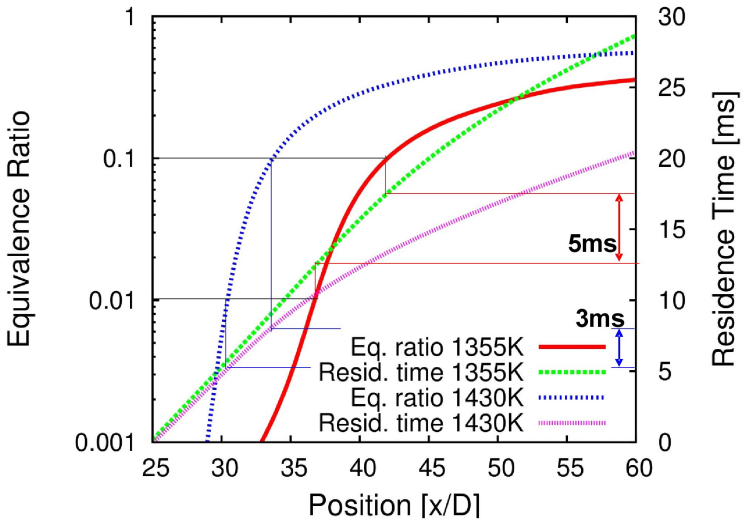

Figure 5.9: Equivalence ratio and integrated residence time on the axial line $r = 7\ d$, representing the ignition line.

process. Thus, the quenching of very lean mixtures by mixing with less lean fresh fluid was underestimated and ignition occurred at a more upstream location.

5.1.5 Conclusions

FGM modeling is a low computational cost approach and therefore particularly interesting for simulating technical configurations. For investigating the potential of this method for capturing autoignition based on precomputed homogeneous reactors, some code developments and preliminary investigations were performed, before simulating an autoigniting methane-air jet.

The following preliminary investigations were performed to apply FGM formalism to autoignition.

- The code *Ignite*'s capability to reproduce ignition delays for homogeneous reactors was demonstrated for methane using GRI3 mechanism, within the conditions of the vitiated coflow burner.
- A progress variable was defined, as it can account for the stages of ignition of methane.
- New nodes distribution functions were defined for the mixture fraction and progress variable to account for the specifics of autoignition in terms of most reactive layers and exponential growth of the progress variable. The new distribution functions

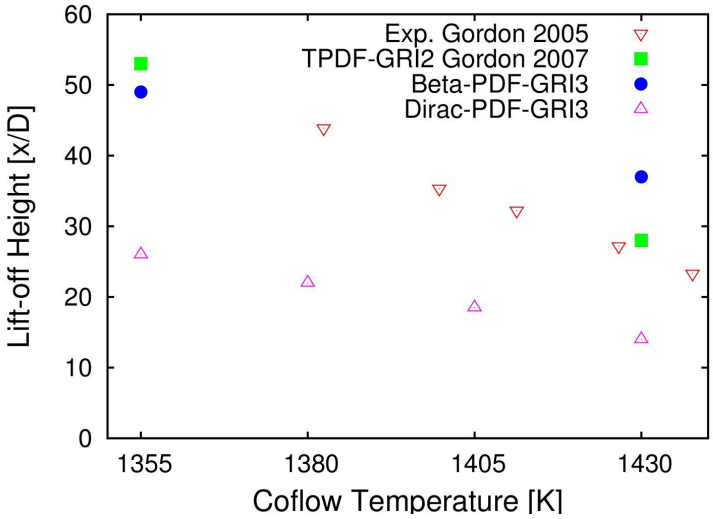

Figure 5.10: Sensitivity of liftoff height to coflow temperature. Experimental and numerical results in [69]. Numerical results using β-PDF and Dirac-PDF.

were implemented into the CFD code. The thermochemical properties of precomputed autoigniting reactors were then tabulated according to these nodes distributions, using β-PDF for mixture fraction and both β-PDF and Dirac-PDF for progress variable.

- To conclude the preliminary investigations, homogeneous autoigniting reactors were simulated applying the CFD code. Ignition delays were reproduced over a wide range of mixture fraction.

Thus, the implementation of the modeling was verified and the capability of predicting autoignition in homogeneous reactors was demonstrated.

The capability of the modeling to account for turbulence chemistry interaction in partially premixed configurations was investigated, while simulating an autoigniting methane-air jet. A lifted flame was obtained for the different parameters that have been applied. The transport of a scaled progress variable without considering the functional dependency of the norm Y_{eq} on mixture fraction was found to not allow the proper description of the mixing of partly reacted very lean reactive fluid with less lean fresh fluid. Thus, only the use of a non-scaled progress variable allowed the capture of the quenching of ignition through fast mixing.

The comparison of temperature profiles with experimental results and the comparison of fields of chemical species with previous investigations using transported PDF with detailed chemistry demonstrated the inability of the modeling to account for reaction

front propagation within a mixing layer, once ignition has been reached. This inaccuracy can clearly be attributed to the neglect of diffusion while computing homogeneous reactors.

At the flame base, diffusion along the streamline leading to ignition was found to be negligible compared to convection and reaction contributions in [69]. In this region, the modeling performed relatively satisfactorily using β-PDF. Quenching of ignition through fast mixing was identified as decisive in capturing flame stabilization. It could be related to the residence time of a fluid element in the most reactive layer, that is shorter than ignition delay. The liftoff height absolute level was correct, while the sensitivity with the coflow temperature was underestimated. Applying β-PDF, the bimodal shape of the progress variable results in a realistic flame brush prior to ignition, even though statistically independent control variables were assumed.

In conclusion, the use of modeling using homogeneous reactors should be limited to cases where neglecting diffusion compared for convection and reaction contributions is acceptable. Due to this limitation, neither simulations using LES nor modeling of forced ignition as a local autoignition phenomenon resulting from heat deposition, were attempted. To extend the model to diffusion in mixture fraction space, the computation of unsteady strained mixing layers is recommended. The modeling of the joint PDF of mixture fraction and progress variable is difficult when applying the FGM model. Transported PDF methods should be able to better capture the averaged source term, but are more costly. Intermittency effects, such as fluttering of the flame base or spotty ignition, could become significant in some parameters. In this case, LES should be considered.

5.2 Forced-Ignited Non-Premixed Jet

This section presents two new methodologies based on LES and on statistical analysis of flow, mixing, turbulent flame speed and ignition events, for predicting the probability of igniting a turbulent non-premixed jet flame with a localized spark. Both methods are applied to a methane-air jet experimentally investigated by Ahmed and Mastorakos [5]. Background information concerning forced ignition of non-premixed mixtures, turbulent jet, propagation and stabilization of jet flames, as well as a description of the configuration are given in Section 5.2.1. The modeling approaches are presented in Section 5.2.3. The results are discussed in Section 5.2.4. Conclusions are given in Section 5.2.5.

Simulations of ignition sequences using LES and FGM modeling were attempted. The favored directions of flame propagation within the numerical grid indicated an inaccuracy

in the prediction of the turbulent flame speed over the flame kernel surface. Thus, these simulations are not documented in this work.

5.2.1 Background

The probabilistic nature of spark ignition in a turbulent non-premixed jet flame has been demonstrated in [15, 154]. The authors measured the flammability factor, P_F, and experimentally investigated the probability of generating a sustainable kernel, P_{ker}. The flammability factor, P_F, is defined as the probability of encountering a mixture fraction within the flammability limits, f_{lean} and f_{rich}.

$$P_F = \int_{f_{lean}}^{f_{rich}} P(f)df. \tag{5.4}$$

They showed that these probabilities are similar on the jet axis ($P_{ker} \approx P_F$), and that the region of stochastical flammability ($P_F > 0$) is wider than the zone where the mean mixture fraction has flammable values.

Ahmed et al. have further investigated the probability of successful ignition for different gaseous non-premixed turbulent configurations. The authors provided detailed information on ignition probability and transient behavior of ignited kernels for jets [5], counterflows [4] and recirculating flames [3]. They showed the existence of regions, that are favorable to flame kernel initiation, but where the generated kernels frequently fail to propagate to regions of stoichiometric mixture and low velocity flow, where the flame can stabilize (P_{ker} high, but P_{ign} low). They also showed that in some flows, P_F may not be equal to P_{ker}, probably due to locally excessive strain, but in the jet this is normally the case. Hence, the transition from a stratified charge kernel to a stratified or partially premixed propagating flame is a key process in successful ignition, and localized strain effects that quench kernels may not be very large for the ignition of a jet flame.

A conceptually similar effort, aimed to predict whole-flame ignition probability by considering the motion of virtual flame elements in a flow field provided by an inert RANS solution, was attempted by Richardson [147] with good results compared to the experiment. Non-Premixed jet flames have been reviewed in the context of forced ignition in [2] and [147].

As the dynamics of the evolving process depend on the scales of time-dependent turbulent motion, methods that are spatially and time-resolved like LES are required. A review on reactive LES and their applications to forced ignition was given in Section 1.3.2.

From the simulations of ignition sequences using LES [16, 105, 168, 162, 172], it could be recognized that:

- the time-resolved calculation of an ignition sequence requires high computational resources, to such an extent that the exploitation of time-resolved events is excluded for performing statistical analysis, such as for predicting the experimentally-observable ignition probability.
- The transient behavior of a flame kernel is determined by the history of the flow field encountered at the kernel surface.

The evolution of ignition kernels is mainly determined by large scale flow structures that are present in the turbulent flow field at ignition time. Hence, the blow-out of successful generated flame kernels, as observed in [5], can be determined by the turbulent flow field at ignition time. Modeling approaches are proposed in Section 5.2.3.

5.2.2 Configuration

The configuration studied here consists of a turbulent methane-air jet experimentally investigated in [5] and simulated in [105]. Figure 5.11 shows a schematic diagram of turbulent jet burner with spark electrodes. A 5 mm diameter jet of fuel (70% of methane and 30% of air by volume) with a bulk velocity of 12.5 m/s issues into a 200 mm diameter co-flow of air moving at $Uc = 0.1$ m/s. The Reynolds number of the jet is $Re_j = 2878$. The jet extends to 130 d downstream of the nozzle so that the internal flow is expected to exhibit a fully developed turbulent velocity profile. The first measured at first step the mean and fluctuating velocity components for a pure air jet. A pair of electrodes was positioned at various locations throughout the flow. A spark with an overall duration of 400 μs and a nominal electrical energy of 100 mJ with an electrode spacing of 1 mm and tip diameters of 0.1 mm was then used.

Following the spark, three main stages for the ignition and the subsequent flame propagation have been observed in [5] and [105] for a 25.5 m/s jet:

- radial flame kernel size linearly growing with time,
- downstream flame propagation and radial expansion; and finally
- tubular upstream flame propagation.

Figure 5.12 shows a sequence of high speed camera images of ignition followed by upstream flame propagation. All the experimental results are reported in detail in [5].

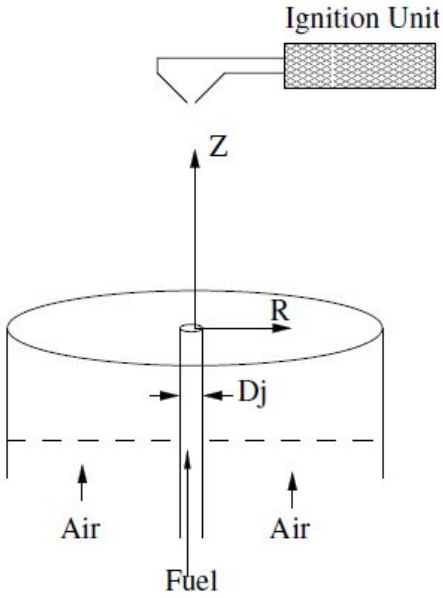

Figure 5.11: Schematic diagram of turbulent jet burner with the spark electrodes, reproduced from [5].

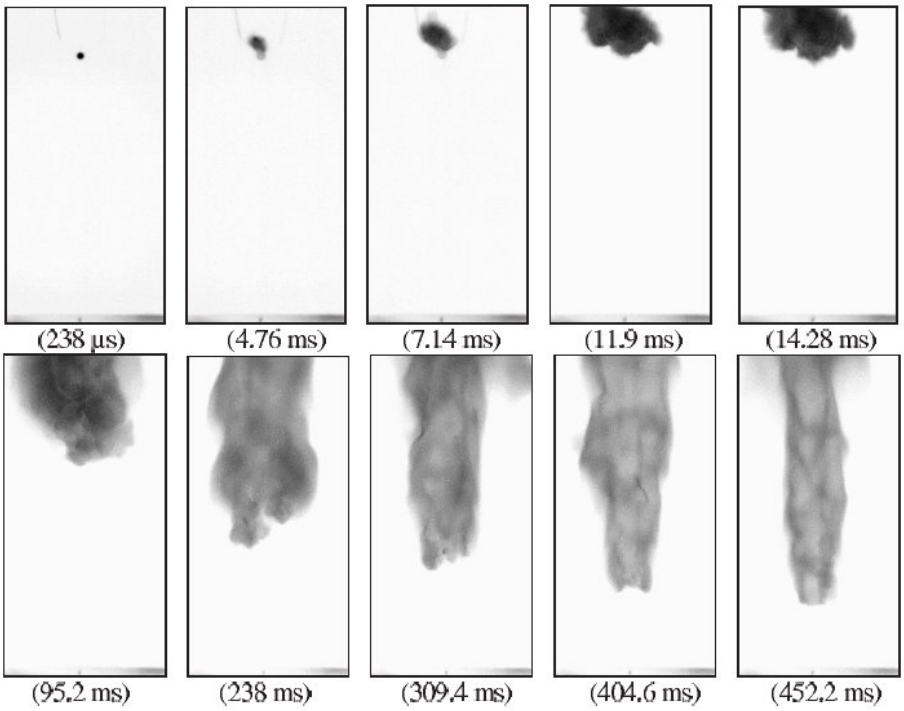

Figure 5.12: High speed camera images of ignition at $r/d = 0$, $z/d = 40$ followed by upstream flame propagation, 25.5 m/s jet.

5.2.3 Modeling Approaches

LES

A simple Smagorinsky model is employed to close the sub-grid scale (SGS) stress-tensor, τ_{ij}^r, with Lilly's formulation of Germano's dynamic procedure for the model coefficient [65]. In the filtered scalar equation, the diffusion coefficient is linked to viscosity via the Schmidt number for which a value $Sc = 0.7$ is assumed. This relates to gaseous mixing. An eddy diffusivity model is used for the SGS scalar flux, assuming a constant Schmidt number relationship between the turbulent diffusion coefficient and the turbulent viscosity, $Sc_t = 0.7$.

The SGS kinetic energy, k_Δ, was calculated from the turbulent viscosity, using Eq. (5.5), with $C_{yo} = 0.086$ according to [187]. The SGS velocity fluctuation, v'_Δ, is given by Eq. (5.6).

$$k_\Delta = {\nu_T}^2/(C_{yo}\Delta)^2 \tag{5.5}$$

$$v'_\Delta = \sqrt{2k_\Delta/3} \tag{5.6}$$

Simultaneous Monitoring of Multiple Ignition Events

The convection of flame kernels is retrieved by monitoring fluid particles representative of ignition events. The particles are seeded in the stationary inert flow and are tracked by a Lagrangian method. The effects of thermal expansion, due to the generation and growth of flame kernels, on the turbulent flow are not directly simulated. Although thermal expansion impacts on the turbulent flow, the probabilistic convection of a kernel is considered as being mainly determined by large scale structures that are already present in the non-ignited flow at ignition time. Thus, an adequate analysis of the stationary inert flow should allow the investigation of the probabilistic convection of ignited kernels.

According to observations in [5], the transition from a radially expanding kernel to a propagating flame capable of upstream displacement takes about 10 ms in case of successful ignition. During the first milliseconds following spark, the mixture conditions over the surface of the kernel can be considered as homogeneous, due to the small size of the kernel in the stratified mixture. Hence, the growth of the kernel during the first milliseconds results in an isotropic thermal expansion. The isotropic effect of thermal expansion is considered as not affecting the convection of the kernel centers. Thus, the center of a flame kernel is expected to follow the same movement as the corresponding fluid element would have followed in the non-ignited configuration. Therefore, the particles representative of ignition events are considered as they exactly follow the turbulent flow.

The kernel deformation due to heterogeneous flow conditions over the radially growing kernel are not considered in the modeling.

Hence, the monitoring of an ignition event is performed by tracking a Lagrangian particle within the LES of the stationary turbulent jet. Since the monitoring of an ignition event does not affect the stationary flow, it is possible to simultaneously monitor multiple ignition events originating at different locations and different instants. Finally, the monitoring of multiple ignition events allows statistical analysis of the convection of flame kernels based on ensemble averaging at a low computational cost. Indeed, the computational cost for performing this ensemble averaging is expected to scale with the computational cost required for performing a statistical analysis of the stationary configuration based on LES.

Moreover, the monitoring of flow properties encountered by spatially distributed particles allows the analysis of statistical conditions within the flow. On the large-eddy scale, the turbulent flame brush can be represented as a thick front propagating at speed $s_{\widehat{T}}$. In the context of premixed mixtures, correlations have been investigated to evaluate the turbulent flame speed [138, 82, 52]. Here, $s_{\widehat{T}}$, is determined at the LES filter size, using the sub-grid velocity fluctuations, as applied in [82], Eq. 5.7:

$$s_{\widehat{T}}/s_L = 1 + C\,(v'_\Delta/s_L)\,. \tag{5.7}$$

Although this model is basically devoted to premixed flames, the method is expected to provide a satisfying estimation of the turbulent flame speed in stratified-charge and partially premixed mixtures with high premixing level. A further restriction to the turbulent speed modeling regards the constant, C, which depends on the estimation of the sub-grid turbulent kinetic energy. Even though C can be adjusted through a dynamic procedure, as in [82], the uncertainties implied by mixture stratification effects, would potentially annihilate the benefits of the dynamic approach. Hence, C is considered as constant here. The determination of its level is discussed in Section 5.2.4.

To evaluate s_L, a 1-dimensional laminar flame code based on detailed chemistry is applied. As mentioned in Section 3.2.3, Chem1D code [33] is used with the GRI-3.0 mechanism for methane from Berkeley University [153]. A parabolic fitting function according to the method by Metghalchi and Keck [121] allows the determination of the local laminar flame speed, s_L, during calculation.

Two new methodologies are proposed for predicting the probability of igniting a turbulent non-premixed jet flame with a localized spark. These methods are introduced here

and further described in Section 5.2.4. In the first method, the probabilistic generation of a flame kernel and its convection are investigated conjointly. The probability of transition from a flame kernel to an upstream propagating flame is determined by analysis of the field of axial flame net displacement speed. This field is calculated by subtraction of the resolved axial flow velocity. Parts of the results for method 1 were published in [180].

In the second method, the axial flame net displacement speed is calculated over the upstream surfaces of flame kernels by subtraction of the resolved axial flow velocity. Thus, the probabilistic generation of a flame kernel and its convection are investigated conjointly together with the probability of transition from a flame kernel to an upstream propagating flame.

Numerical Set-Up

A block-structured mesh has been used and optimized for the simulation of ignition events. The total number of cells is 1.5×10^6. The minimal cell at jet outlet is $0.3 \times 0.3 \times 0.15\ mm^3$ while it is of $1.4 \times 0.65 \times 0.65\ mm^3$ on the jet axis at 50 d.

As inlet boundary conditions, a turbulent pipe flow is generated over a distance of 10 d, Figure 5.14. No special measures are taken to impose artificial turbulence on the inflow. For the co-flow, an inflow distance of 20 d is calculated, Figure 5.13.

Figure 5.13 shows a mesh section of the whole computational domain. Figure 5.14 shows a magnification of a mesh section on the 10 d long inlet tube. Figure 5.15 shows a magnification of a cross section of the mesh at the nozzle exit level.

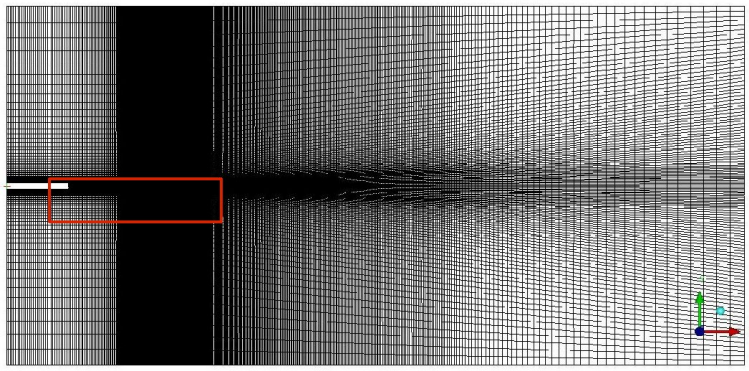

Figure 5.13: Mesh section of the whole computational domain. The red box shows the magnification region on the inlet tube, Figure 5.14.

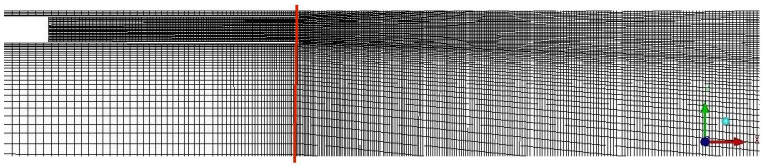

Figure 5.14: Magnification of a mesh section on the nozzle exit level showing the 10 d long inlet tube. The red line shows the cross section at the nozzle exit level, Figure 5.15.

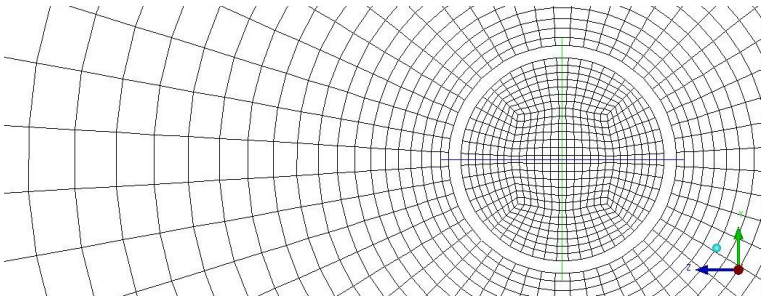

Figure 5.15: Magnification of a cross section of the mesh at the nozzle exit level.

Two cases for which experimental results are available were investigated. The first features an air-air jet mixture with a bulk velocity of 21 m/s. It is used to appraise the LES methodology. The second case consists of the methane-air jet with a bulk velocity of 12.5 m/s, as described in Section 5.2.2.

With respect to the Lagrangian particles tracking, a total amount of about 55,000 statistically independent particles are injected into the ignitable region of the non-ignited turbulent flow. Each particle is representative of an ignition event and their history is monitored over 20 ms. The possibility of upstream flame displacement is evaluated over the kernel surface. Therefore, a kernel diameter of 35 mm at 10 ms is considered, based on the visualization of [5]. The modeling applied to derive the probability of finding an upstream axial net velocity over the kernel surface is detailed in Section 5.2.4.

Figure 5.16 show the seeding of Lagrangian particles and their convection over a time period of 10 ms. The color show the equivalence ratio: red is 1.5, blue 0.5.

5.2.4 Results and Discussion

Turbulent flow field of air/air jet

An air-air jet mixture with a bulk velocity of 21 m/s was simulated to appraise the LES methodology. This configuration was also investigated in [5, 147, 105] for validation purpose. Figure 5.17 shows good agreement between Tieszen's empirical expression, Eq. 5.8,

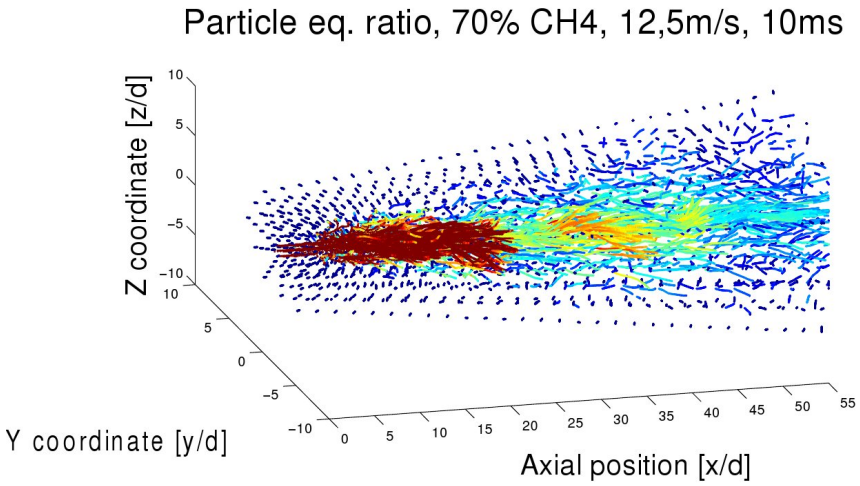

Figure 5.16: Lagrangian particles tracking, 10 ms, colors show equivalence ratio: red is 1.5, blue 0.5.

for mean axial velocity, U_m, in a self-preserving jet [166] and the LES prediction.

$$\frac{U_m}{U_j} = 11.8 \left(\frac{\rho}{\rho_0}\right)^{1/2} \left(\frac{r_0}{z}\right) exp\left[-93.7 \left(\frac{r}{z}\right)^2\right] \tag{5.8}$$

U_j is the jet velocity. The density is homogeneous for the air/air jet $\rho/\rho_0 = 1$. $r_0 = 0$ on the jet axis.

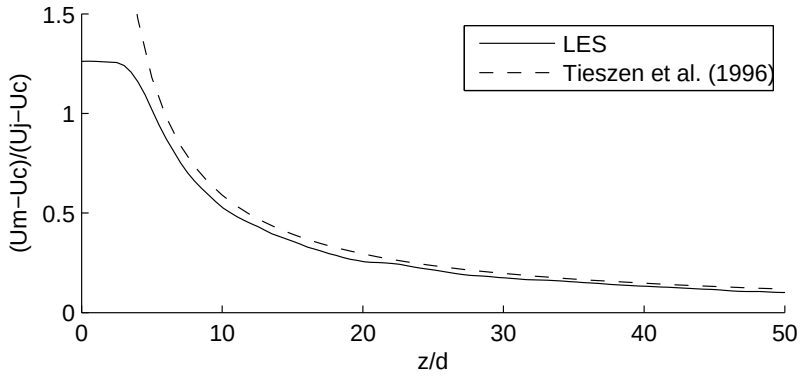

Figure 5.17: Mean axial velocity along the center line of jet for the air/air jet from LES and Eq. 5.8

Figure 5.18 (left) shows the radial distribution of the mean axial velocity, U, scaled by the respective values on the axis, U_m, for the air/air jet. Figure 5.18 (right) displays the radial distribution of the axial velocity fluctuation, U'. The red curves show the profiles according to the empirical rules by Wygnanski and Fiedler [186]. Typical jet self-similarity characteristics are obtained. For exposition purpose the experimental data [5]

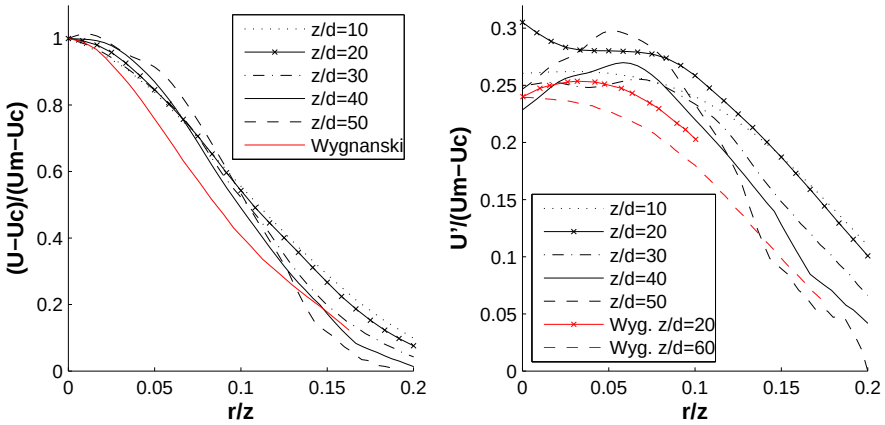

Figure 5.18: Radial distribution of the mean axial velocity (left), and of its fluctuation (right). 21 m/s air jet

are displayed in Figure 5.19. The mean values are in good agreement with the empirical rules, while the fluctuations are slightly overpredicted. This investigation demonstrates the prediction capability of the LES methodology, that was then used for further investigations.

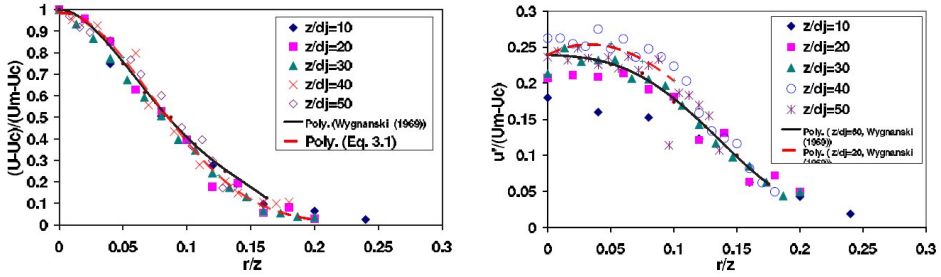

(a) (b)

Figure 5.19: Radial distribution of the mean axial velocity (a), and of its fluctuation (b) reproduced from [5] (Poly (Eq.3.1) means here Eq. 5.8) , 21 m/s air jet

Mixing field of methane/air jet

The results of the mixing field of the 12.5 ms methane/air jet are compared to empirical expressions by Richards and Pitts [146]. The correlation Eq. 5.9 is applied to provide an estimation of the mean mixture fraction as a function of the axial position, z, and of a non-dimensional radial coordinate, $\theta = \frac{r}{z-7.2\ r_{jet}}$. For fluctuations, the correlation Eq. 5.10 is applied.

$$\bar{f}(z,\theta) = \left(\frac{\rho_{jet}}{\rho_{air}}\right)^{1/2} \frac{9.52\ r_{jet}}{z - 7.2\ r_{jet}} exp\left(-59\ \theta^2\right). \tag{5.9}$$

$$f'(z,\theta) = \left(\frac{\rho_{jet}}{\rho_{air}}\right)^{1/2} \frac{9.52\ r_{jet}}{z - 7.2\ r_{jet}} \left[0.23 + 0.35\ \theta + 9.09\ \theta^2 - 116.48\ \theta^3 + 240.81\ \theta^4\right]. \tag{5.10}$$

Figure 5.20 shows the radial distributions of mean values and rms values of mixture fraction. The jet inner cone exists until an axial position of $z = 20\ d$. Further downstream, the mean values agree well with empirical law, while the rms values are slightly overpredicted.

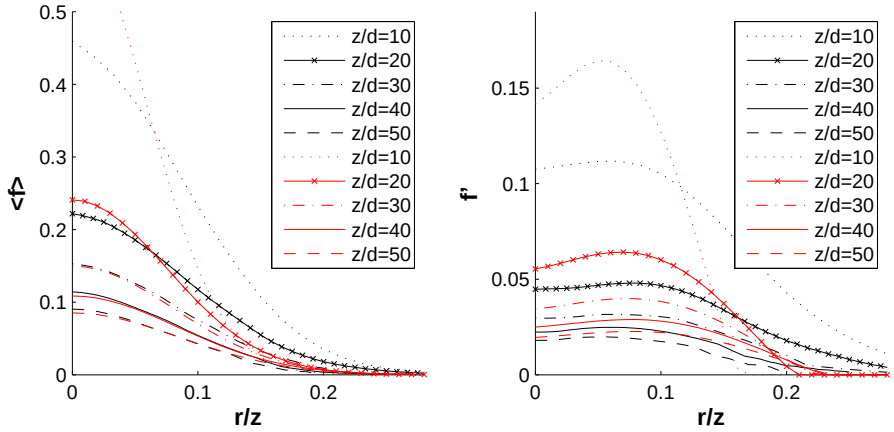

Figure 5.20: Radial distributions of mean mixture fraction (left) and mixture fraction rms (right). Black lines from LES. Red lines from [146].

Figure 5.21(a) shows isolines for equivalence ratios of 0.5, 1 and 1.5. The correlation by Richards and Pitts [146], Eq. 5.9 is applied for comparison (dashed line).

Figure 5.21(b) displays the probability of finding a flammable mixture called flammability factor, P_F. It is representative of the probability of generating a viable flame kernel, P_{ker}, in regions of moderate strain, which can be found in the downstream region ($z > 30\ d$) and are the focus of this study. This was calculated by time-integration of the realization of mixture fraction between the lean and rich flammability limits.

Flame stabilization region

According to observations in [5], the transition from a radially expanding kernel to a propagating flame capable of upstream displacement takes about 10 ms in case of successful ignition. This is the time required until the kernel reaches a width of about 7 d. At that time, the kernel surface reaches a flame stabilizing region, characterized by near-stoichiometric mixture and low velocity flow.

Figure 5.21(c) shows a scatter plot of the upstream flame speed on the axial direction, restricted to particles with radial positions between 2 and 4 d, at 4 time steps (0, 5, 10, 15 ms) of a 15 ms sequence, as well as the measured upstream speed [5]. The majority of the particles display negative values (i.e. would be convected downstream). However, flame wrinkling increases the flame propagation velocity and the overall upstream flame speed can be assessed from the particles with the highest velocities representative of the velocity of the leading part of the flame surface. Indeed, visualization of ignition events shows a "tongue-like" upstream propagation, with significant variations in the shape of the leading edge of the flame [5, 4, 3], which is consistent with the view that only a few particles can be responsible for overall successful upstream flame ignition.

The comparison to the experimental upstream speed provide a method to adjust the constant C, in Eq. 5.7, accounting for SGS flame wrinkling effects. Hence, a coefficient value of, $C = 2.5$, close to the value of 2.25 used in [138], is found to deliver maximum upstream speed consistent with experimental data.

A contour plot of upstream flame speed was generated considering only particles with upstream velocities, ($U_{up} > 0$). The flame stabilizing region, Figure 5.21(d), displays a tubular form with radial positions between 2 and 4 d. This agrees well with the observation of a tubular upstream flame propagation, see Figure 5.12. The level of the upstream speed is also in good agreement with the experimental data.

Probability of upstream flame displacement (method 1)

Considering the form of the stabilizing region and the upstream flame speed distribution in this region, it is possible to evaluate the probability of upstream flame displacement at any point. Outside the tubular stabilizing region the probability is found to be zero. Within the region, the probability is evaluated from the fraction of points with an upstream flame speed for a given axial position $P_1(z)$, which is derived from the scatter plot displayed on Figure 5.21(c).

The dashed line in Figure 5.22 shows the probability of upstream flame displacement inside the stabilizing region over axial position for a single point. A maximal probability close to 30% is reached within a range of axial positions between 28 and 35 d, where low flow velocities and near-stoichiometric mixture fractions are favorable for stabilization. Further downstream, increased mixing with the coflow results in leaner mixtures and lower flame speeds, so that the probability of upstream flame displacement decreases continuously and becomes zero at an axial position of 60 d.

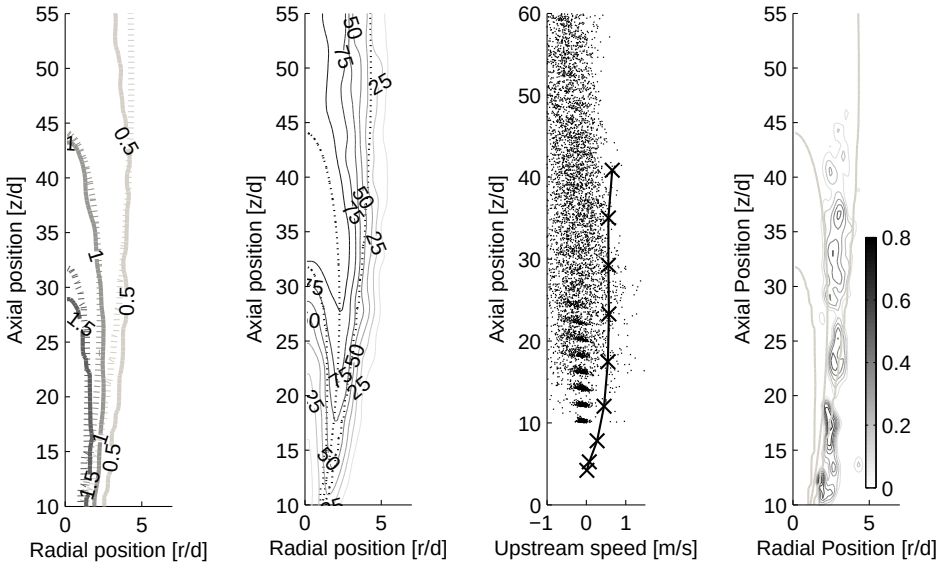

(a) (b) (c) (d)

Figure 5.21: (a) Mean mixture fraction fields after Richards' correlation [146] (dashed) and from LES. Isolines show equivalence ratio of 0.5, 1. and 1.5. (b) Flammability factor representative of the probability of successful kernel generation, P_{ker}. (c) Scatter plot of upstream flame speed and measured absolute flame speed in [5]. (d) Field of upstream flame speed [m/s], conditioned on particles with positive speed.

The probability of upstream flame displacement needs to be integrated over the surface of a flame kernel. This probability, $P_{up}(z, r_{ker})$, is expressed in Eq. 5.11, as a function of the axial position z and of a conceptual number, n_{surf}, of statistically independent locations on the contact surface between the kernel and the tubular region.

$$[1 - P_{up}(z, r_{ker})] = [1 - P_1(z)]^{n_{surf}} \tag{5.11}$$

On the jet axis, the surface of the kernel is in contact with the whole surface of the stabilizing ring. Assuming a distance of 1 d to determine the conceptual number of statistically independent locations yields $n_{surf} = \pi 7d/d \approx 22$. The continuous curve displayed on Figure 5.22 shows this integrated probability of upstream flame displacement over axial position for a 100% surface contact.

For an off-axis position, an analytical expression of the number n_{surf} is given by Eq. 5.12 as a function of the radial position of the kernel center, r_{ker}. Indeed, the number n_{surf} is obtained from the arc length of the tubular zone that is in contact with the flame kernel surface. This tubular zone, $3 < r/d < 4$, is displayed on Figure 5.23(b) in light gray, while the representative kernel disk is displayed in dark gray, with a diameter of 7 d, following

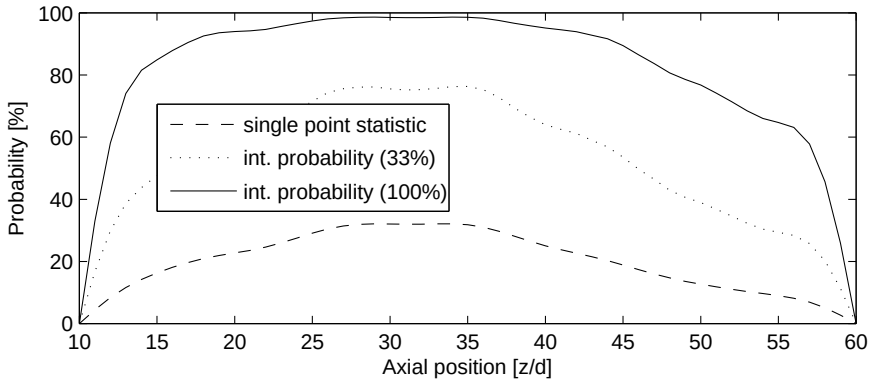

Figure 5.22: Probability of upstream flame displacement inside the stabilizing region over axial position. Results are shown for a single point and for a contact surface between the flame kernel and the stabilizing ring surface of 33%, respectively of 100% of the stabilizing ring surface.

the experimental observation in [5] of the kernel diameter at transition time to a stable propagating flame.

$$n_{surf}(r_{ker}) = \frac{\pi 7d}{d}\frac{1}{\pi} acos\left(\frac{|r_{ker} - d/2|}{7d}\right) \tag{5.12}$$

For a radial position at the center of a flame kernel of $r_{ker} = 4\ d$, 33% of the surface of the stabilizing ring is in contact with the kernel surface. The corresponding integrated probability of upstream flame displacement is displayed by the dotted line on Figure 5.22.

With respect to the probabilistic convection of the particles after 10 ms (Figure 5.23(a)), it is now possible to evaluate the probability that a flame kernel initiated at a given spark location, will encounter upstream flame displacement over its surface after 10 ms. Figure 5.24(c) shows the probability map of successful ignition, P_{ign}, where it refers to the probability of generating a kernel P_{ker} and of flame stabilization, $P_{up}(z, r_{ker})$, at the location where the kernel has been convected. The probability of ignition is calculated as a product of probabilities.

The predicted probability of ignition is qualitatively consistent with the experimental values, displayed on Figure 5.24(a), although numerical differences exist. Comparison to Figure 5.21(b) shows a lower probability for P_{ker} than for P_{ign}, in the downstream region ($z/d > 45$). It indicates that ignited kernels fail to stabilize. The statistical occurrence of lean ignited kernel blow-out events is delayed at an axial distance of 5 d on the jet axis, with respect to the experimental data. In this region, the radial decay is essentially

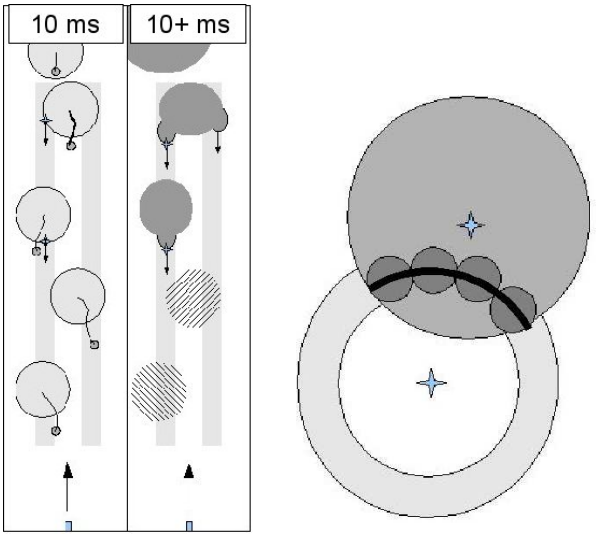

Figure 5.23: (a) Schematics of the simultaneous monitoring of Lagrangian particles representative for ignition events, showing five simultaneous events in the flammable zone, at two time steps: 10 ms (left) and a few ms later (right). Surfaces show two quenching events due to high strain (dashed), two successful transitions to upstream propagating flames in the tubular zone and one kernel blow-out event. (b) Schematic of the contact surface between the flame kernel (dark grey) and the tubular zone (fair grey), showing four conceptually independent locations at a distance of 1 d from each other (method 1).

obtained from the modeling used for integrating the probability over the contact surface and the trends are consistent with experimental data.

The axial delay in the prediction of the statistical occurrence of blow-out events can be attributed to the definition of the criterion for evaluating the possibility of upstream flame propagation. Indeed, the probability of upstream displacement is calculated as the fraction of points with an upstream flame speed. However, the effective upstream displacement of the flame front requires a flame speed that is strictly positive. Hence, by restricting the probability of upstream displacement to the fraction of points with a flame speed higher than a threshold value U_{th}, it is possible to account for this effect.

Figure 5.24(d) shows the probability map of successful ignition with a threshold speed of $U_{th} = 0.15\ m/s$. This threshold value sets the probability of successful ignition of 55% on the jet axis at an axial position of $z/d = 45$, as found experimentally. Applying this threshold speed, the probability of ignition is better predicted. In particular, the radial and axial trends of the statistical occurrence of flame blow-out are better predicted in the downstream region of the jet for $z > 40\ d$, where successfully generated kernels fail to stabilize. A residual probability of possible flame stabilization (less than 25%) is obtained

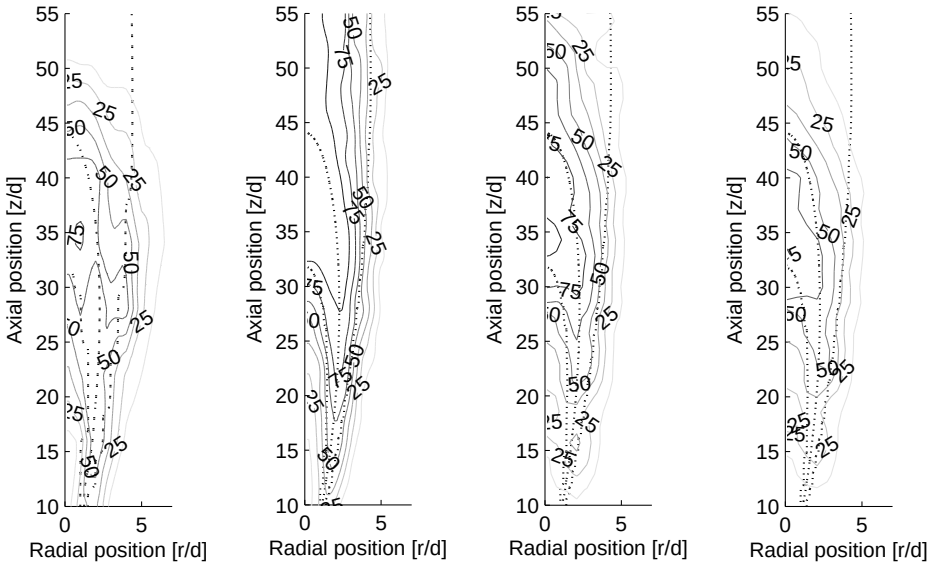

Figure 5.24: Maps of probability: (a) Experimental results for successful ignition, P_{ign}, in [5], (b) Flammability factor representative of the probability of successful kernel generation, P_{ker}, (c) Probability of successful ignition, P_{ign}, as probability of generating a kernel P_{ker} and of flame stabilization, $P_{up}(z, r_{ker})$ (method 1). (d) Probability of successful ignition, considering the probability of upstream flame speed higher than a threshold value of $U_{th} = 0.15\ m/s$.

on the jet axis in the range of $50 < z/d < 55$, whereas this probability should be zero in this domain. The region of high ignition probability is predicted correctly in terms of location and probability level. Hence, the use of a threshold speed for accounting for effective flame upstream displacement seems to be adequate modeling. However, this approach needs to be further investigated. In particular, better analysis of the statistical field of absolute flame speed should permit to improve the approximation of the probability of upstream speed over a contact surface. Instead of further developing this method, a more general approach was investigated.

Probability of upstream flame displacement (method 2)

The prediction of P_{ign} is improved by a more general method relying on the monitoring of the kernel surfaces that is able to account for the correlated properties of the mixture at spark location, the kernel convection and the conditions over the kernel surface. Figure 5.23(a) displays a schematic of the method for determining the possibility of upstream displacement. The axial flame net displacement speed is calculated over the upstream surfaces (half sphere) of flame kernels by subtraction of the resolved axial flow

velocity. Figures 5.25(b), (c) and (d) show the probability maps of successful ignition. This probability is now denoted $P_{ign} = P_{(f|U_{up}>U_{th})}$ and refers to the joint probability of kernel generation, $P_{ker} = P_f$, and of an upstream flame propagation speed, U_{up}, higher than defined velocity thresholds, $U_{th} \in [0.3; 0.4; 0.5\ m/s]$. These cut-off levels account for the effective upstream propagation of the flame surface part with the highest upstream speed, being only possible for a certain local upstream speed level.

The applied thresholds appear to have a strong influence on the estimation of successful stabilization. A cut-off level of $U_{th} = 0.3\ m/s$, Figure 5.25(b), delivers a probability of blow-out similar to the first monitoring method, Figure 5.24(c). A level of $0.4\ m/s$ predicts the behavior in the downstream lean flammable region relatively well for $z/d > 45$, while a much higher blow-out probability is obtained in this domain with $U_{th} = 0.5\ m/s$. The latter level better predicts the radial trend in the domain with $P_{ign} > 50\%$. In particular, it can be noticed that the probability slightly increases with the radius for $0 < r/d < 2$. In this region, lower premixedness level of the partially premixed mixture are found. Following this, it can be expected that a higher upstream speed threshold is required there.

The threshold values applied here are higher than for method 1. Method 2 is supposed to be more reliable, since the upstream propagation speed is evaluated on the kernel surface. In particular, the better prediction of the radial trends is a good indicator of better reliability of method 2. Moreover, the values are to be compared to the upstream speeds measured in [5]. The experimental speeds are nearly constant over the axial position range, $U_{up} \approx 0.6\ m/s$ for $17 < z/d < 40$. The results obtained with method 2 suggest that the leading part of the flame surface, at the location with the highest upstream speed is able to stabilize the flame front only if this local upstream speed reaches a level that is almost the speed of the established upstream propagating flame.

Effects of mixture fraction and velocity fluctuations

Lagrangian monitoring allows investigation the effects of mixture fraction and velocity fluctuations on ignition processes, that are essential in IC engines among others, as evidenced in [49].

Conditional statistics, such as the flammability factor conditioned on low velocities, as performed in [105] with a level of $5\ m/s$ to account for the quenching strain rate, are useful in the analysis of ignition processes. Using time-resolved particles monitoring, conditional statistics can be calculated as a postprocessing step and be extended to fluid element transport conditioned on mixture fraction and velocity at spark location.

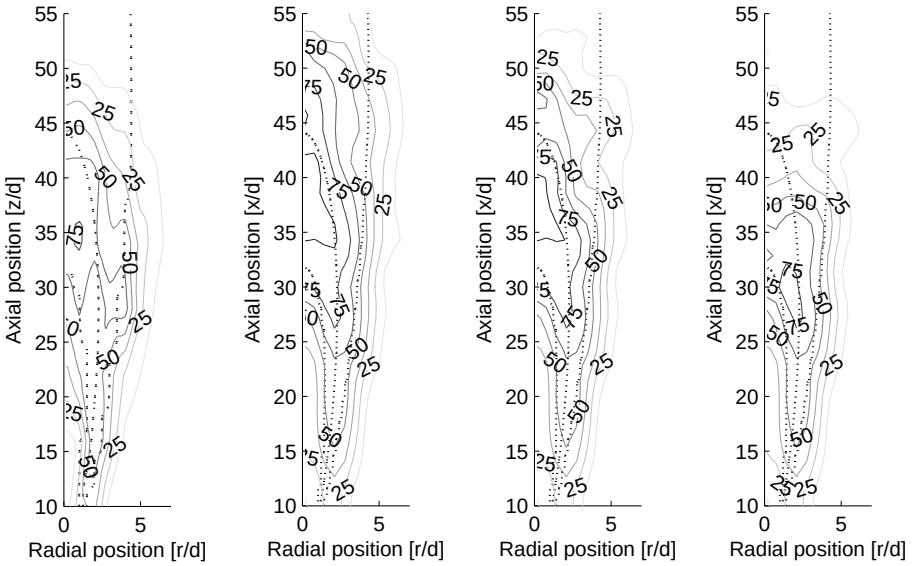

Figure 5.25: Maps of probability of ignition processes: (a) Experimental results for successful ignition, P_{ign}, in [5], (b) probability of successful ignition, P_{ign}, as joint probability of kernel generation and upstream propagating flame higher than 0.3 m/s (method 2), $P_{ign} = P_{(f|up>0.3\ m/s)}$, respectively (c) 0.4 m/s and (d) 0.5 m/s. Equivalence ratio isolines in [146].

To validate the method for intermittency effects, mixture-conditioned statistics have been investigated. Figure 5.26(a) shows the axial convection after 10 ms, $\widetilde{d_{10}z}$, of the center of kernels initiated on the jet axis, with $40 < z/d < 53$ and conditioned on flammable, lean and rich flammable mixtures, denoted respectively by the subscripts f, l and r. Values close to 3 d agree well with the observation of kernel downstream displacement before transition to an upstream propagating flame [5]. According to Figure 5.26(a), rich flammable mixtures are transported over a range of approximately 3.6 d, compared to 2.9 d for lean flammable mixtures. A consistent phenomenon has been observed on the axis for $25 < z/d < 35$, where the analysis of the flammability factor conditioned on low velocity levels revealed higher velocities for mixture fractions over the rich flammability limit than for flammable ones.

Figures 5.26(b) and (c) show the conditional upstream flame speeds, $\widetilde{U_{up}}$, over the kernel surface and the radial positions of the corresponding surface location, $\widetilde{r}$. No noticeable differences due to the conditioning on mixture fraction are found. Thus, the potential of the conditional statistics postprocessing to account for correlations between conditions at ignition location and over the surface of the convected flame kernels is demonstrated.

However, further investigations are required to validate the advantages inherent to this method.

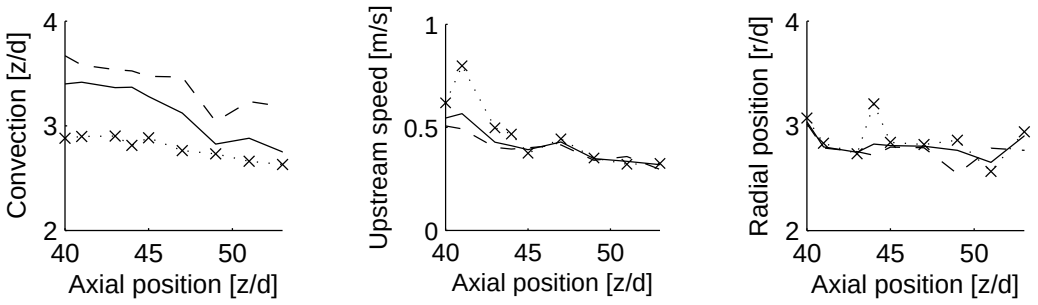

(a) (b) (c)

Figure 5.26: Mixture-conditioned statistics of ignition processes initiated on the jet axis: (a) conditional axial convection of kernel center before transition, $\widetilde{d_{10}z_f}$, $\widetilde{d_{10}z_l}$ and $\widetilde{d_{10}z_r}$, (b) conditional flame upstream speed, $\widetilde{U_{up|f}}$, $\widetilde{U_{up|l}}$ and $\widetilde{U_{up|r}}$, (c) conditional radial position of upstream flame surface point with highest upstream speed, $\widetilde{r_f}$, $\widetilde{r_l}$ and $\widetilde{r_r}$. Indices f : —, l : - x - and r : – – refer to flammable, lean and rich flammable mixtures.

5.2.5 Conclusions

Two methods that couple an LES for a jet to Lagrangian monitoring of fluid particles were developed and validated. They allow statistical analysis of the transition of a flame kernel to an upstream propagating turbulent flame, hence allowing a prediction of the overall flame ignition probability following a local spark.

The first method accounts for the probabilistic kernel generation and convection and for the probability of kernel blow-out at the corresponding location. The velocity and mixing fields were validated by using experimental measurements. The predicted region of possible upstream flame propagation, characterized by near-stoichiometric mixture and low velocity flow, compares well with the available experimental data regarding its form and upstream flame speed.

The second method accounts for the correlated effects of the three probabilistic processes of generation, convection and flow conditions over the flame kernel surface. The comparison of results to experimentally-determined ignition maps demonstrates that both methods are capable of accounting for the probabilistic blow-out of flame kernels and predicting reasonably well the locations in the jet having high ignition probability. Radial trends are better predicted with method 2.

A speed threshold for effective upstream propagation was used, that appears to be capable of predicting the possibility of transition to an upstream propagating flame once this threshold speed is determined. However, the thresholds found for method 1 and 2 have different values. The value found with method 2 is considered to be more reliable.

Correlation effects between mixture at ignition location and convection have been demonstrated. However, further investigations are required to validate the advantages inherent to this method.

The quenching of kernels due to high strain rates in the lower part of the jet has not been investigated here. Even though the effects of the thermal expansion on the flow have been neglected, the proposed method is capable of predicting the transition from a kernel to an upstream propagating flame. Comparisons of simulations of ignition events and non-ignited flow should allow to isolate these effects and improve the modeling. This method is intended to be applied to complex configurations, like gas turbines combustors and IC engines.

6 Conclusions and Future Work

Numerical modeling methods for predicting ignition processes were developed with the intention of supporting the design of current and future aero-engine combustors with advanced relight capability. Therefore, cost-effective approaches were designed and implemented into a new CFD code, PRECISE-UNS. The development of this new unstructured code was needed since advanced low-NO_x, lean-burn concepts imply complex air-fuel mixing and therefore complex combustor geometries, which are laborious to mesh with multi-block mesh structures.

The methods developed are dedicated to two different ignition processes. Firstly, a computationally time-efficient method was designed for simulating autoignition in turbulent non-premixed configurations. Secondly, a particularly cost-effective method for performing statistical investigations of spark ignition was developed.

Autoignition

Similar to FGM modeling, a method that relies on the resolution of the detailed chemistry of autoigniting homogeneous reactors was developed and used to simulate an autoigniting methane-air jet.

The implementation of the modeling was verified and the capability to predict autoignition in homogeneous reactors was demonstrated. Therefore, preliminary developments, implementations and validations were achieved.

- The code *Ignite*'s capability to reproduce ignition delays in perfectly-stirred reactors was demonstrated for methane, using the GRI3 mechanism in the conditions of the vitiated coflow burner.
- A progress variable was defined, as it can account for the stages of ignition of methane.
- The specifics of the thermochemical properties of autoigniting homogeneous reactors were identified and a dedicated chemistry tabulation was performed.
- Ignition delays were reproduced over a wide range of mixture fractions using the CFD code.

An autoigniting methane-air jet was simulated [179]. The stabilization mechanism of the lifted flame was identified as resulting from the quenching of ignition through fast mixing. The need to apply a non-scaled progress variable was pointed out. The interaction between slow chemistry and turbulent mixing yielded a realistic flame brush prior to ignition. The capability of this modeling to account for chemistry-turbulence interaction was demonstrated. However, the assumption of statistically independent control variables was contradicted in the VCB in [124].

Limitations of this modeling were identified. The inability to account for reaction front propagation within a mixing layer was demonstrated, as the chemistry look-up table does not account for diffusion. Modeling of forced ignition, as a local autoignition phenomenon resulting from heat deposition, was therefore not considered further.

For future works on autoignition, it would be of interest to tabulate diffusion, for instance using unsteady diffusion flamelets, as noted in [118, 48]. Once this has been achieved, modeling of forced ignition as a local autoignition phenomenon could be considered. Although it cannot be expected to accurately describe the thermochemical state within a spark, the potential of the spark modeling should be investigated, particularly the capability to account for spark energy effects.
In technical applications, autoignition phenomena are generally unsteady, whereas the VCB's lifted flame is stationary. Experimental model burners, such as [117], are needed to better understand the stochastical effects of mixture fraction and scalar dissipation on apparently randomly occurring autoignition kernels.

Forced Ignition

Two methods for performing statistical analysis of spark ignition events in non-premixed configurations have been developed and validated. The methods couple LES to Lagrangian monitoring of fluid particles and were applied to a spark-ignited, non-premixed methane-air jet [180, 181].

The monitoring of Lagrangian fluid particles seeded into the stationary inert flow enables the simultaneous analysis of multiple ignition events. Hence, the modeling allows ensemble averaging for prediction of the overall flame ignition probability following a local spark. Statistical analysis of transient phenomena is achieved in a very efficient manner, as the computational cost scales with the cost required to perform standard LES statistics of the inert turbulent configuration.

The first method accounts for the probabilistic kernel generation and convection and for the probability of kernel blow-out at the corresponding location. The second accounts for the correlated effects of the three probabilistic processes of generation, convection and flow conditions over the flame kernel surface.

The comparison of results to experimentally-determined ignition maps demonstrates, that both methods are capable of accounting for the probabilistic blow-out of flame kernels and for predicting the locations in the jet that have high ignition probability reasonably well.

For both methods, a speed threshold for effective upstream propagation was also used. The methods appear to be capable of predicting the possibility of transition to an upstream propagating flame, once threshold speed is determined. Method 2 better predicts the radial trends. Correlation effects between mixture at ignition location and convection were demonstrated. Quenching of kernels due to high strain rates in the lower part of the jet was not investigated. Further treatment of the simulation results could eventually account for this phenomenon.

For future work, further investigations and developments can be of interest. The modeling can be directly applied to other configurations, as long as experimental observations of kernel growth are available. In particular, the simulated jet should be investigated with different parameters, as performed in [5]. The other configurations investigated in [3] and [4] are also relevant.

Extension of the model to include the effects of the local turbulent flow properties on the radial kernel growth should be realizable without too much difficulty. Thus, the methods could be applied to further laboratory burners and technical applications without experimental observations of kernel growth.

Simulations of ignition sequences using LES and FGM modeling should be further attempted. Thorough preliminary investigations of flame propagation speed, as undertaken by Aschmoneit [6], are needed. Once turbulent flame speed can be predicted, attention should be paid to the thermal expansion that follows spark initiation and growth. Thorough analysis of the effects of thermal expansion on the transition from a kernel to a propagating flame could eventually allow derivation of generic rules. The effects of thermal expansion could then possibly be integrated into the modeling of simultaneous ignition events.

Bibliography

[1] S. K. Aggarwal. A review of spray ignition phenomena: present status and future research. *Progress in Energy and Combustion Science*, 24:565–600, 1998.

[2] S. F. Ahmed. *Spark Ignition of Turbulent Non-premixed Flames*. PhD thesis, Cambridge University, 2006.

[3] S. F. Ahmed, R. Balachandran, T. Marchione, and E. Mastorakos. Spark ignition of turbulent non-premixed bluff-body flames. *Combustion and Flame*, 151:366–385, 2007.

[4] S. F. Ahmed, R. Balachandran, and E. Mastorakos. Measurements of ignition probability in turbulent non-premixed counterflow flames. *Proceedings of the Combustion Institute*, 31:1507–1513, 2007.

[5] S. F. Ahmed and E. Mastorakos. Spark ignition of lifted turbulent jet flames. *Combustion and Flame*, 146(1-2):215 – 231, 2006.

[6] K. Aschmoneit. Private communication. February 2010.

[7] D. R. Ballal and A. H. Lefebvre. Influence of flow parameters on minimum ignition energy and quenching distance. *Proceedings of the 15th International Symposium on Combustion*, pages 1473–1481, 1974.

[8] D. R. Ballal and A. H. Lefebvre. Ignition and flame quenching of quiescent fuel mists. *Proceedings of the Royal Society of London*, 364:277–294, 1978.

[9] D. R. Ballal and A. H. Lefebvre. A general model of spark ignition for gaseous and liquid fuel-air mixtures. *Proceedings of the 18th International Symposium on Combustion*, 18(1):1737–1746, 1981.

[10] G. K. Batchelor. *The Theory of Homogeneous Turbulence*. Cambridge University Press, 1953.

[11] Berkeley VCB website. URL `www.me.berkeley.edu/cal/vcb/index.htm`. April 2010.

[12] F. Biagioli. Stabilization mechanism of turbulent premixed flames in strongly swirled flows. *Combustion Theory and Modelling*, 10(3):389–412, 2006.

[13] G. Bikas. PhD thesis, RWTH Aachen, 2001.

[14] R. W. Bilger, S. B. Pope, K. N. C. Bray, and J. F. Driscoll. Paradigms in turbulent combustion research. *Proceedings of the Combustion Institute*, 30:21–42, 2005.

[15] A. D. Birch, D. R. Brown, and M. G. Godson. Ignition probability in turbulent mixing flows. *Proceedings of the 18th Combustion Symposium*, pages 1775–1780, 1981.

[16] M. Boileau, G. Staffelbach, B. Cuenot, and T. Poinsot. LES of an ignition sequence in a gas turbine engine. *Combustion and Flame*, 154:2–22, 2008.

[17] R. Borghi. Turbulent combustion modeling. *Prog. Energy Combust. Sci.*, 14:245–292, 1988.

[18] R. Borghi. On the Structure and Morphology of Turbulent Premixed Flames. *Recent Advance in Aeronautical Science*, pages 117–138, 1985.

[19] G. Bourque, D. Healy, H. J. Curran, J. M. Simmie, J. de Vries, V. Antonovski, B. Corbin, C. Zinner, and E. Petersen. Effect of higher-order hydrocarbons on methane-based fuel chemistry at gas turbines pressures. *Proceedings of ASME Turbo Expo 2007*, 2007.

[20] D. Bradley. How fast can we burn? *Symposium (International) on Combustion*, 24 (1):247 – 262, 1992.

[21] M. Brandt. *Beschreibung der Selbstzünding in turbulenter Strömung unter Einbeziehung ternärer Mischvorgänge.* PhD thesis, Technische Universität München, 2005.

[22] N. Branley and W. P. Jones. Large eddy simulation of a turbulent non-premixed flame. *Combustion and Flame*, 127(1-2):1914 – 1934, 2001.

[23] W. J. G. Bräunling. *Flugzeugtriebwerke.* Springer-Verlag, 2004.

[24] K. Bray, P. Domingo, and L. Vervisch. Role of the progress variable in models for partially premixed turbulent combustion. *Combustion and Flame*, 141(4):431 – 437, 2005.

[25] K. N. C. Bray, P. A. Libby, and J. B. Moss. Flamelet crossing frequencies and mean reaction rates in premixed turbulent combustion. *Combust. Sci. Tech.*, 41:143–172, 1984.

[26] T. Breitenberger. Validierung und Auswertung von LES in Dolfyn. Master's thesis, TU Darmstadt, 2008.

[27] W. L. Briggs. *A Multigrid Tutorial*. SIAM, Philadelphia, 1987.

[28] R. Cabra, T. Myhrvold, J.Y. Chen, R. W. Dibble, A. N. Karpetis, and R. S. Barlow. Simultaneous laser raman-rayleigh-lif measurements and numerical modeling results of a lifted turbulent h2/n2 jet flame in a vitiated coflow. *Proceedings of the Combustion Institute*, 29(2):1881 – 1888, 2002.

[29] R. Cabra, J.-Y. Chen, R. W. Dibble, A. N. Karpetis, and R. S. Barlow. Lifted methane-air jet flames in a vitiated coflow. *Combustion and Flame*, 143(4):491 – 506, 2005.

[30] CFD Research Corporation. US patent 6272840 B1.

[31] N. Chakraborty and E. Mastorakos. Numerical investigation of edge flame propagation characteristics in turbulent mixing layers. *Physics of Fluids*, 18, 2006.

[32] N. Chakraborty and E. Mastorakos. Direct numerical simulations of localised forced ignition in turbulent mixing layers: the effects of mixture fraction and its gradient. *Flow, Turbulence and Combustion*, 80:155–186, 2008.

[33] Chem1D. Chem1D, a one dimensional laminar flamelet code. URL `www.combustion.tue.nl/flamecodes/chem1d`. February 2010.

[34] M. Chrigui, K. Moesl, W. Ahmadi, A. Sadiki, and J. Janicka. Partially premixed prevalorized kerosene spray combustion in turbulent flow. *Experimental Thermal and Fluid Science*, 34(3):308 – 315, 2010. Sixth Mediterranean Combustion Symposium.

[35] O. Colin, F. Ducros, D. Veynante, and T. Poinsot. A thickened flame model for large eddy simulations of turbulent premixed combustion. *Physics of fluids*, 12(7): 1843–1863, 2000.

[36] B. Cuenot, F. Egolfopoulos, and T. Poinsot. An unsteady laminar flamelet model for non-premixed combustion. *Combustion Theory and Modelling*, 4(1):1364–7830, 2000.

[37] P. Dagaut and M. Cathonnet. The ignition, oxidation and combustion of kerosene: A review of experimental and kinetic modeling. *Progress in Energy and Combustion Science*, 32:48–92, 2006.

[38] R. Dahms, T. D. Fansler, M. C. Drake, T.-W. Kuo, A. M. Lippert, and N. Peters. Modeling ignition phenomena in spray-guided spark-ignited engines. *Proceedings of the Combustion Institute*, 32(2):2743 – 2750, 2009.

[39] G. Damköhler. Der Einfluss der Turbulenz auf die Flammengeschwindigkeit in Gasgemischen. *Z. Elektrochem.*, 46(11):601–652, 1947.

[40] L. P. H. de Goey and J. H. M. ten Thije Boonkkamp. A flamelet description of premixed laminar flames and the relation with flame stretch. *Combustion and Flame*, 119(3):253 – 271, 1999.

[41] L. P. H. de Goey, R. M. M. Mallens, and J. H. M. Ten Thije Boonkkamp. An evaluation of different contributions to flame stretch for stationary premixed flames. *Combustion and Flame*, 110(1-2):54 – 62, 1997.

[42] J. W. Deardorff. A numerical study of three-dimensional turbulent channel flow at large Reynolds numbers. *J. Fluid Mech.*, 41(2):453–480, 1970.

[43] J. E. Dec. Advanced compression-ignition engines - understanding the in-cylinder processes. *Proceedings of the Combustion Institute*, 32(2):2727–2742, 2009.

[44] Deutsche Forschungsgemeinschaft. URL `www.dfg.de/jahresbericht/detail_5_4_-WAE_1344.htm`. February 2010.

[45] F. di Mare, W. P. Jones, and K. R. Menzies. Large eddy simulation of a model gas turbine combustor. *Combustion and Flame*, 137(3):278 – 294, 2004.

[46] T. Doerr. Introduction to aero-engine gas turbine combustion. *Rolls-Royce Deutschland Ltd & Co KG*, 2008.

[47] P. Domingo and L. Vervisch. Triple flames and partially premixed combustion in autoignition of non-premixed turbulent mixtures. *Symposium (International) on Combustion*, 26(1):233 – 240, 1996.

[48] P. Domingo, L. Vervisch, and D. Veynante. Large-eddy simulation of a lifted methane jet flame in a vitiated coflow. *Combustion and Flame*, 152(3):415 – 432, 2008.

[49] M. C. Drake, T. D. Fansler, B. Böhm, S. Busch, and K. Peterson. Understanding ignition processes in spray-guided gasoline engines using high speed laser imaging techniques. *9th International Congress Engine Combustion Process*, 2009.

[50] J. M. Duclos and O. Colin. Arc and kernel tracking ignition model for 3d si engines calculations. *Comodia, Nagoya, Japan*, pages 343–350, 2001.

[51] M. Düsing. *Large-Eddy Simulation turbulenter Vormischflammen*. PhD thesis, TU Darmstadt, 2004.

[52] M. Düsing, A. Sadiki, and J. Janicka. Towards a classification of models for the numerical simulation of premixed combustion based on a generalized regime diagram. *Combustion Theory and Modelling*, 10:105–132, 2006.

[53] L. Elliott, D. B. Ingham, A. G. Kyne, N. S. Mera, M. Pourkashanian, and C. W. Wilson. Genetic algorithms for optimisation of chemical kinetics reaction mechanisms. *Progress in Energy and Combustion Science*, 30(3):297 – 328, 2004.

[54] Environmental Protection Agency. Clean Air Act, 2009.

[55] Environmental Protection Agency. URL `www.epa.gov/airscience/quick-finder/-ozone.htm`. February 2010.

[56] European Comission. Giving wings to emission trading; inclusion of aviation under the european emission trading system (ets): design and impacts, .

[57] European Comission. regulation (ec) no 715/2007 of the european parliament and of the council of 20 june 2007 on type approval of motor vehicles with respect to emissions from light passenger and commercial vehicles (euro 5 and euro 6) and on access to vehicle repair and maintenance information, .

[58] European Comission. Directive 2008/101/ec of the european parliament and of the council of 19 november 2008 amending directive 2003/87/ec so as to include aviation activities in the scheme for greenhouse gas emission allowance trading within the community, .

[59] European Commission. European aeronautics: A vision for 2020 - meeting society's needs and winning global leadership. *Report of the Group of Personalities*, 2001.

[60] T. D. Fansler, M. C. Drake, and B. Böhm. High-speed mie-scattering diagnostics for spray-guided gasoline engine development. *Proceedings of the 8th International Symposium on Internal Combustion Diagnostics*, 2008.

[61] J. H. Ferziger and M. Perić. *Computational Methods for Fluid Dynamics*. Springer, 1999.

[62] M. Freitag and J. Janicka. Investigation of a strongly swirled unconfined premixed flame using LES. *Proceedings of the Combustion Institute*, 31:1477–1485, 2006.

[63] M. Frenklach, H. Wang, and M. J. Rabinowitz. Optimization and analysis of large chemical kinetic mechanisms using the solution mapping method–combustion of methane. *Progress in Energy and Combustion Science*, 18(1):47 – 73, 1992.

[64] S. M. Gallagher, H. J. Curran, W. K. Metclafe, J. M. Simmie, and G. Bourque. A rapid compression machine study of the oxidation of propane in the negative temperature coefficient regime. 2007.

[65] M. Germano, U. Piomelli, P. Moin, and W. Cabot. A dynamic subgrid-scale eddy viscosity model. *Physics of Fluids A*, 3(7):1760–1765, 1991.

[66] J. Gikadi. Turbulenzmodellierung für die Simulation der Brennkammer-Turbine Interaktion in einem Flugtriebwerk. *TU Darmstadt*, 2009.

[67] R. L. Gordon. Private communication. February 2008.

[68] R. L. Gordon, A. R. Masri, and E. Mastorakos. Heat release rate as represented by [OH] [CH2O] and its role in autoignition. *Combustion Theory and Modelling*, 13 (4):1364–7830, 2009.

[69] R. L. Gordon, A. R. Masri, S. B. Pope, and G. M. Goldin. Transport budgets in turbulent lifted flames of methane autoigniting in a vitiated co-flow. *Combustion and Flame*, 151(3):495 – 511, 2007.

[70] R. L. Gordon, A. R. Masri, and E. Mastorakos. Simultaneous rayleigh temperature, oh- and ch2o-lif imaging of methane jets in a vitiated coflow. *Combustion and Flame*, 155(1-2):181 – 195, 2008.

[71] S. Gordon and B. J. McBride. Computer Program for Calculation of Complex Chemical Equilibrium Compositions and Applications. *NASA Reference publication 1311*, 1994.

[72] J. Göttgens, F. Mauss, and N. Peters. Analytic approximations of burning velocities and flame thicknesses of lean hydrogen, methane, ethylene, ethane, acetylene, and propane flames. *Symposium (International) on Combustion*, 24(1):129 – 135, 1992. Twenty-Fourth Symposium on Combustion.

[73] W. Hackbusch. *Multi-Grid Methods and Applications*. Springer, Berlin, 1985.

[74] C. Hasse. *A Two-Dimensional Flamelet Model for Multiple Injections in Diesel Engines*. PhD thesis, RWTH Aachen, 2004.

[75] D.C. Haworth. Progress in probability density function methods for turbulent reacting flows. *Progress in Energy and Combustion Science*, 36(2):168 – 259, 2010.

[76] J. B. Heywood. *Internal combustion engine fundamentals*. 1988.

[77] R. Hilbert and D. Thévenin. Autoignition of turbulent non-premixed flames investigated using direct numerical simulations. *Combustion and Flame*, 128(1-2):22 – 37, 2002.

[78] S. Honnet, K. Seshadri, U. Niemann, and N. Peters. A surrogate fuel for kerosene. *Proceedings of the Combustion Institute*, 32(1):485 – 492, 2009.

[79] C. C. Huang, S. S. Shy, C. C. Liu, and Y. Y. Yan. A transition on minimum ignition energy for lean turbulent methane combustion in flamelet and distributed regimes. *Proceedings of the Combustion Institute*, 31(1):1401 – 1409, 2007.

[80] hypre - high performance preconditioners. User's manual. *Center for Applied Scientific Computing, Lawrence Livermore National Laboratory http://acts.nersc.gov/hypre/*.

[81] M. Ihme, C. M. Cha, and H. Pitsch. Prediction of local extinction and re-ignition effects in non-premixed turbulent combustion using a flamelet/progress variable approach. *Proceedings of the Combustion Institute*, 30(1):793 – 800, 2005.

[82] H. G Im. Study of turbulent premixed flame propagation using laminar flamelet model. *Center for Turbulence Research, Annual Research Briefs*, pages 347–360, 1995.

[83] Intergovernmental Panel on Climate Change. Climate change 2007: Mitigation of climate change. 2007.

[84] Intergovernmental Panel on Climate Change. Climate change 2007: Synthesis report, 2007.

[85] International Civil Aviation Organization. Assessing current scientific knowledge, uncertainties and gaps in quantifying climate change, noise and air quality aviation impacts; final report of the international civil aviation organization (icao) committee on aviation and environmental protection (caep) workshop, 2007.

[86] International Energy Agency. World energy outlook 2009, 2009.

[87] S. James, M. S. Anand, M. K. Razdan, and S. B. Pope. In situ detailed chemistry calculations in combustor flow analyses. *Journal of Engineering for Gas Turbines and Power*, 123(4):747–756, 2001.

[88] J. Janicka and A. Sadiki. Large eddy simulation of turbulent combustion systems. *Proceedings of the Combustion Institute*, 30:537–547, 2005.

[89] W. Jones and B. Launder. The prediction of laminarization with a two-equation model of turbulence. *International Heat and Transfer*, 15:301–314, 1972.

[90] W. P. Jones and S. Navarro-Martinez. Large eddy simulation of autoignition with a subgrid probability density function method. *Combustion and Flame*, 150(3):170 – 187, 2007.

[91] W. P. Jones and S. Navarro-Martinez. Study of hydrogen auto-ignition in a turbulent air co-flow using a large eddy simulation approach. *Computers & Fluids*, 37(7):802 – 808, 2008.

[92] W. P. Jones, S. Navarro-Martinez, and O. Roehl. Large eddy simulation of hydrogen auto-ignition with a probability density function method. *Proceedings of the Combustion Institute*, 31(2):1765 – 1771, 2007.

[93] A. Kempf. *Large-Eddy Simulation of Non-Premixed Turbulent Flames*. PhD thesis, TU Darmstadt, Darmstadt, Germany, 2003.

[94] A. Kempf, H. Forkel, J.-Y. Chen, A. Sadiki, and J. Janicka. Large-eddy simulation of a counterflow configuration with and without combustion. *Proceedings of the Combustion Institute*, 28(1):35 – 40, 2000.

[95] A Ketelheun. Application and Investigation of Flamelet Generated Manifolds Theory with Regard to Mixture Fractions beyond Flammability Limits. Master's thesis, TU Darmstadt, 2008.

[96] A Ketelheun, O. Olbricht, F. Hahn, and J. Janicka. Premixed generated manifolds aiming on the computation of gas turbine combustion. *ASME Turbo Expo: Power for Land, Sea and Air*, 2009.

[97] V. Klapdor. Validierung eines unstrukturierten Verbrennungs-CFD Codes. Master's thesis, TU Darmstadt, 2007.

[98] M. Klein, N. Chakraborty, and R.S. Cant. Effects of turbulence on self-sustained combustion in premixed flame kernels: a direct numerical simulation study. *Flow, Turbulence and Combustion*, 81(4):583–607, 2008.

[99] A. Y. Klimenko and R. W. Bilger. Conditional moment closure for turbulent combustion. *Progress in Energy and Combustion Science*, 25:595–687, 1999.

[100] A. Kolmogorov. The Equations of Turbulent Motion in an Incompressible Fluid. *Izvestia Acad. Sci., USSR*, 66:56–58, 1942.

[101] A. N. Kolmogorov. Dissipation of energy in locally isotropic turbulence. *Acad. Sci. USSR*, 32:16–18, 1941.

[102] H. W. Krüs. Dolfyn Developers Guide. *Cyclone Fluid Dynamics BV*, 2006.

[103] J. Kuehne, A. Ketelheun, and J. Janicka. Analysis of sub-grid PDF of a progress variable approach using a hybrid LES/TPDF method. *33rd Combustion Symposium*, 2010.

[104] G. Lacaze, B. Cuenot, T. Poinsot, and M. Oschwald. Large eddy simulation of laser ignition and compressible reacting flow in a rocket-like configuration. *Combustion and Flame*, 156(6):1166 – 1180, 2009.

[105] G. Lacaze, E. Richardson, and T. Poinsot. Large eddy simulation of spark ignition in a turbulent methane jet. *Combustion and Flame*, 156(10):1993 – 2009, 2009.

[106] T. Landenfeld. *Numerische Beschreibung turbulenter Methandiffusionsflammen mit Schließungsmodellen zweiter Ordnung und angenommenen Wahrscheinlichkeitsdichtefunktionen*. PhD thesis, Technische Universität Darmstadt, 1999.

[107] B. E. Launder, G. J. Reece, and W. Rodi. Progress in the Development of a Reynolds-Stress Turbulent Closure. *Journal of Fluid Mechanics*, 68(3):537–566, 1975.

[108] C. K. Law. *Combustion Physics*. Cambridge University Press, 2006.

[109] C. J. Lawn. Lifted flames on fuel jets in co-flowing air. *Progress in Energy and Combustion Science*, 35(1):1 – 30, 2009.

[110] W. Lazik, T. Doerr, and S. Bake. Low NOx Combustor Development for the Engine3E Core Engine Demonstrator. *ISABE-2007-1190*, 2007.

[111] A. H. Lefebvre. Fuel effects on gas turbine combustion - ignition, stability and combustion efficiency. *Journal of engineering for gas turbines and power*, 107:24–37, 1985.

[112] A. H. Lefebvre. *Gas Turbine Combustion*, volume 2nd edition. Taylor and Francis, 1998.

[113] M. Lesieur, O. Métais, and P. Comte. *Large-Eddy Simulations of Turbulence*. Cambridge Univ. Press, Cambridge, UK, 2005.

[114] A. Liñán. The asymptotic structure of counterflow diffusion flames for large activation energies. *Acta Astronautica*, 1:1007–1039, 1974.

[115] D. Lilly. The Representation of Small-Scale Turbulence in Numerical Simulation Experiments. *Proceedings of the IBM Scientific Computing Symposium on Environmental Sciences*, pages 195–210, 1967.

[116] D. K. Lilly. A proposed modification of the germano subgrid-scale closure method. *Physics of Fluids A*, 4(3):633–635, 1992.

[117] C. N. Markides and E. Mastorakos. An experimental study of hydrogen autoignition in a turbulent co-flow of heated air. *Proceedings of the Combustion Institute*, 30: 883–891, 2005.

[118] E. Mastorakos. Ignition of turbulent non-premixed flames. *Progress in Energy and Combustion Science*, 35:57–97, 2009.

[119] E. Mastorakos, T. A. Baritaud, and T. J. Poinsot. Numerical simulations of autoignition in turbulent mixing flows. *Combustion and Flame*, 109:198–223, 1997.

[120] R. G. McKinney, D. Sepulveda, W. Sowa, and A. K. Cheung. The Pratt & Whitney TALON X low emissions combustor: revolutionary results with evolutionary technology. *45th AIAA Aerospace Sciences Meeting and Exhibits*, 2007.

[121] M. Metghalchi and J. C. Keck. Burning velocities of mixtures of air with methanol, isooctane, and indolene at high pressure and temperature. *Combustion and Flame*, 48(2):191–210, 1982.

[122] J.-B. Michel, O. Colin, and D. Veynante. Comparison of Differing Formulations of the PCM Model by their Application to the Simulation of an Auto-igniting H2/air Jet. *Flow, Turbulence and Combustion*, 83(1):33–60, 2009.

[123] J.-B. Michel, O. Colin, and D. Veynante. Modeling ignition and chemical structure of partially premixed turbulent flames using tabulated chemistry. *Combustion and Flame*, 152(1-2):80 – 99, 2008.

[124] J.-B. Michel, O. Colin, C. Angelberger, and D. Veynante. Using the tabulated diffusion flamelet model adf-pcm to simulate a lifted methane-air jet flame. *Combustion and Flame*, 156(7):1318 – 1331, 2009.

[125] B. P. Mullins. The spontaneous combustion of fuels injected into a hot gas stream. *Symposium on Combustion, Flame and Explosion Phenomena*, 3:704–713, 1949.

[126] S. Navarro-Martinez and A. Kronenburg. LES-CMC simulations of a lifted methane flame. *Proceedings of the Combustion Institute*, 32(1):1509 – 1516, 2009.

[127] D. A. Nikolaus, D. S. Crocker, D. L. Black, and C. E. Smith. Development of a lean direct fuel injector for low emission aero gas turbines. *Proceedings of ASME Turbo Expo 2002*, 2002.

[128] M. Obermüller. Simulation of Sandia Flame D with LES and the FGM Chemistry Model in Dolfyn. Master's thesis, TU Darmstadt, 2010.

[129] O. Olbricht, F. Hahn, A Ketelheun, and J. Janicka. PDF modeling strategies for LES of a bluff-body stabilized H2/CH4 flame. *Turb. Shear Flow Phenom. 6*, 2009.

[130] S.V. Patankar. Numerical Heat Transfer and Fluid Flow. *Hemisphere Publishing Co.*, 1980.

[131] N. Peters. *Turbulent Combustion*. Cambridge University Press, 2000.

[132] C. D. Pierce and P. Moin. Progress-variable approach for large eddy simulation of non-premixed turbulent combustion. *Journal of Fluid Mechanics*, 504:73–97, 2004.

[133] C. D. Pierce. *Progess-Variable Approach for Large-Eddy Simulation of turbulent combustion*. PhD thesis, Standford University, 2001.

[134] U. Piomelli, J. Ferziger, P. Moin, and J. Kim. New Approximate Boundary Conditions for Large Eddy Simulations of Wall-Bounded Flows. *Phys. Fluids A*, 1: 1061–1068, 1989.

[135] H. Pitsch. Large-eddy simulation of turbulent combustion. *Annual Review of Fluid Mechanics*, 38:453–82, 2006.

[136] H. Pitsch and M. Ihme. An Unsteady/Flamelet Progress Variable Method for LES of Nonpremixed Turbulent Combustion. *43rd AIAA Aerospace Sciences Meeting and Exhibit*, 2005.

[137] H. Pitsch and H. Steiner. Large-eddy simulation of a turbulent piloted methane/air diffusion flame (sandia flame d). *Physics of Fluids*, 12(10):2541–2554, 2000.

[138] A. Pocheau. Front propagation in a turbulent medium. *Europhysics Letters*, 20: 401, 1992.

[139] T. Poinsot and D. Veynante. *Theoretical and Numerical Combustion*. Edwards, 2001.

[140] S. B. Pope. *Turbulent Flows*. Cambridge University Press, 2000.

[141] S. B. Pope. Pdf methods for turbulent reactive flows. *Progress in Energy and Combustion Science*, 11(2):119 – 192, 1985.

[142] L. Prandtl. Bericht über die Entstehung der Turbulenz. *Zeitschrift für Angewandte Mathematik und Mechanik*, 5:136–139, 1925.

[143] K. V. L. Rao and A. H. Lefebvre. Minimum ignition energies in flowing kerosine-air mixtures. *Combustion and Flame*, 27(1):1–20, 1976.

[144] O. Reynolds. On the Dynamical Theory of Incompressible Viscous Fluids and the determination of the Criterion. *Philos. Trans. R. Soc. London Ser. A*, pages 123–164, 1895.

[145] C. M. Rhie and W. L. Chow. Numerical study of the turbulent flow past an airfoil with trailing edge separation. *AIAA Journal*, 21(11):1525–1532, 1983.

[146] C. Richards and W Pitts. Global density effects on the self-preservation behaviour of turbulent free jets. *Journal of Fluid Mechanics*, 254:417–435, 1993.

[147] E. S. Richardson. *Ignition modelling for turbulent non-premixed flow.* PhD thesis, Cambridge University, 2007.

[148] E. S. Richardson, N. Chakraborty, and E. Mastorakos. Analysis of direct numerical simulations of ignition fronts in turbulent non-premixed flames in the context of conditional moment closure. *Proceedings of the Combustion Institute*, 31(1):1683 – 1690, 2007.

[149] Rolls-Royce plc. The jet engine, 2005.

[150] M. Schäfer. *Numerik im Maschinenbau.* Springer-Verlag, 1999.

[151] U. Schumann. Subgrid scale model for finite difference simulations of turbulent flows in plane channels and annuli. *Journal of Computational Physics*, 18:376–404, 1975.

[152] J. S. Smagorinsky. General circulation experiments with the primitive equations. *Monthly Weather Review*, 91:99–164, 1963.

[153] G. P. Smith, D. M. Golden, M. Frenklach, N. W. Moriarty, B. Eiteneer, M. Goldenberg, C. T. Bowman, R. K. Hanson, S. Song, W. C. Gardiner, V. V. Lissianski, and Z. Qin. URL `www.me.berkeley.edu/gri_mech`. February 2010.

[154] M. Smith, A. Birch, D. Brown, and M. Fairweather. Studies of ignition and flame propagation in turbulent jets of natural gas, propane and a gas with a high hydrogen content. *Proceedings of the 21st Combustion Symposium*, pages 1403–1408, 1986.

[155] M. D. Smooke, I. K. Puri, and K. Seshadri. A comparison between numerical calculations and experimental measurements of the structure of a counterflow diffusion flame burning diluted methane in diluted air. *Symposium (International) on Combustion*, 21(1):1783 – 1792, 1988.

[156] B. Somers. *The Simulation of Flat Flames with Detailed and Reduced Chemical Models*. PhD thesis, TU Eindhoven, 1994.

[157] L. J. Spadaccini. Ignition delay characteristics of methane fuels. *Progress in Energy and Combustion Science*, 20:431–460, 1994.

[158] L. J. Spadaccini, F. K. Owen, and C. T. Bowman. Influence of aerodynamic phenomena on pollutant formation in combustion. *EPA-600/2-76-247a*, 1976.

[159] D. B. Spalding. Mixing and chemical reaction in steady confined turbulent flames. *Proc. Combust. Inst.*, 13:646–657, 1971.

[160] M. Staufer. *Large Eddy Simulation of Premixed and Partially Premixed Flames*. PhD thesis, TU Darmstadt, Darmstadt, Germany, 2009.

[161] H. N. Subba-Rao and A. H. Lefebvre. Ignition of kerosine fuel sprays in a flowing air stream. *Combustion science and technology*, 8:95–100, 1973.

[162] V. Subramanian, P. Domingo, and L. Vervisch. Large eddy simulation of forced ignition of an annular bluff-body burner. *Combustion and Flame*, 157(3):579 – 601, 2010.

[163] C. J. Sung, C. K. Law, and J.-Y. Chen. Further Validation of an Augmented Reduced Mechanism for Methane Oxidation: Comparison of Global Parameters and Detailed Structure. *Combustion Science and Technology*, 156(1), 2000.

[164] Z. Tan and R. D. Reitz. An ignition and combustion model based on the level-set method for spark ignition engine multidimensional modeling. *Combustion and Flame*, 145(1-2):1 – 15, 2006.

[165] J. F. Thompson. *Handbook of grid generation*. CRC Press, Boca Raton, 1999.

[166] S. R. Tieszen, D. W. Stamps, and T. J. O'Hern. A heuristic model of turbulent mixing applied to blowout of turbulent jet diffusion flames. *Combustion and Flame*, 106(4):442 – 462, 1996.

[167] A. Triantafyllidis. *Large Eddy Simulations of Spark Ignition Processes with the CMC method*. PhD thesis, Cambridge University, 2009.

[168] A. Triantafyllidis, E. Mastorakos, and R.L.G.M Eggels. Large Eddy Simulations of forced ignition of a non-premixed bluff-body methane flame with Conditional Moment Closure. *Combustion and Flame*, 156:2328–2345, 2009.

[169] T. Tsuboi and H. Gg. Wagner. Homogeneous thermal oxidation of methane in relected shock waves. *Proc. Combust. Inst. 15*, pages 883–890, 1975.

[170] H. A. van der Vorst. A fast and smoothly converging variant of Bi-CG for the solution of nonsymmetric linear systems. *SIAM J. Sci. Stat. Comput.*, 13(2):631–644, 1992.

[171] J. A. van Oijen. *Flamelet-Generated Manifolds: Development and Applications to Premixed Laminar Flames*. PhD thesis, TU Eindhoven, 2002.

[172] O. Vermorel, S. Richard, O. Colin, C. Angelberger, A. Benkenida, and D. Veynante. Towards the understanding of cyclic variability in a spark ignited engine using multi-cycle les. *Combustion and Flame*, 156(8):1525 – 1541, 2009.

[173] A. W. Vreman, B. A. Albrecht, J. A. van Oijen, L. P. H. de Goey, and R. J. M. Bastiaans. Premixed and nonpremixed generated manifolds in large-eddy simulation of sandia flame d and f. *Combustion and Flame*, 153(3):394 – 416, 2008.

[174] N. Waldbüßer. *NOx Minderung am PKW-Dieselmotor mit einem Kombinationssystem zur Abgasnachbehandlung*. PhD thesis, Technische Universität Kaiserslautern, 2005.

[175] J. Warnatz, U. Mass, and R. W. Dibble. *Combustion: physical and chemical fundamentals, modeling and simulation, Experiments, Polutant Formation*. 2001.

[176] J. Weckering. Implementation and Validation of a Two-Dimensional Flamelet Model into AC-FluX. *ITV, RWTH Aachen*, 2005.

[177] J. Weckering. Untersuchung über die Entschwefelung von NOx-Speicher-Katalysatoren für kombinierte Abgasnachbehandlungsverfahren. Master's thesis, 2006.

[178] J. Weckering, A. G. Varias, and V. Doquet. Numerical investigation of sub-critical crack growth in alpha-titanium due to hydride formation and fracture. *ECCOMAS 2004*, 2004.

[179] J. Weckering, R. Gordon, A. Sadiki, R. Eggels, and J. Janicka. Investigation of auto-ignition of a lifted methane-air jet flame in hot coflow with progress variable approach. *24. Deutscher Flammentag, Bochum*, 2009.

[180] J. Weckering, A. Sadiki, J. Janicka, and E. Mastorakos. Investigations of ignition probability of a forced ignited turbulent methane jet based on LES. *ECCOMAS 2010*, 2010.

[181] J. Weckering, A. Sadiki, J. Janicka, E. Mastorakos and R.L.G.M. Eggels. A forced ignition probability analysis method using LES and Lagrangian particle monitoring. *Proceedings of the Combustion Institute*, 33:2919–2925, 2011.

[182] B. Wegner. *A large-eddy simulation technique for the prediction of flow, mixing and combustion in gas turbine combustors*. PhD thesis, TU Darmstadt, 2006.

[183] P. Wenzel, C. Kruger, R. Steiner, R. Schießl, C. Hofrath, and U. Maas. 3D-CFD Simulation of DI-Diesel Combustion applying a Progress Variable Approach accounting for detailed chemistry. *SAE International*, 2007.

[184] F. A. Williams. Recent Advances in Theoretical Descriptions of Turbulent Diffusion Flames, Turbulent Mixing in Reactive and Non reactive Flows. *Plenum Press*, 1975.

[185] F. A. Williams. *Combustion Theory, The Fundamental Theory of Chemically Reacting Flow Systems*. The Benjamin/Cummings Publishing Company, 2nd edition, 1985.

[186] I. Wygnanski and H. Fiedler. Some measurements in the self-preserving jet. *Journal of Fluid Mechanics*, 38(03):577–612, 1969.

[187] A. Yoshizawa. Statistical theory for compressible turbulent shear flows, with the application to subgrid modeling. *Physics of Fluids*, 29(7):2152–2164, 1986.

[188] Y. B. Zeldovich. The oxidation of nitrogen in combustion and explosions. *Acta Physicochimica*, 1946.

RESUME

PERSONAL

Name: Jeremy Weckering
Nationality: French
Birth: 22 April 1979, in Toul, France

EDUCATION

07/1997 Baccalauréat Scientifique, mention bien, Lycée Louis Majorelle, Toul, France
09/97 – 06/98 ESSTIN, Nancy, France
09/98 – 06/00 Classes préparatoires PT*, Lycée Loritz, Nancy, France

08/00 – 07/04 **Ecole Polytechnique**, Palaiseau, France
Specialization: "Mechanics Material & Structures"/"Engineering Sciences"
Master Thesis: "Numerical Investigation of Sub-Critical Crack Growth in α-Titanium due to Hydride Formation and Fracture", Prof. A. Varias, Malmö University, Sweden
Awarded in March 2005: "Ingénieur Diplômé de l'Ecole Polytechnique"

10/03 – 02/06 **RWTH Aachen**, Germany
Mechanical Engineering / Energy Engineering / Combustion Engines
2004/2005: 1 year fellowship of the DAAD (German Academic Exchange Service)
Student Internship: "Numerical investigation of the combustion in a diesel engine", Prof. Dr.-Ing., Dr.-h. c., Dr.-Ing. E. h. N. Peters
Diploma Thesis by Daimler Chrysler AG: "Investigation of the desulfation of NOx-traps for combined exhaust gas after-treatment systems", Prof. Dr.-Ing. S. Pischinger
Awarded in March 2006: "Diplom-Ingenieur"

11/06 – 06/10 **Ph.D. studies at TU Darmstadt, Institute EKT, Prof. Dr.-Ing. Janicka**
Development of Numerical Modeling Methods for Prediction of Ignition Processes in Aero-Engines
Research fellowship: DFG-Graduate School GRK1344 in collaboration with Rolls-Royce Deutschland: "Unsteady System Modelling of Aircraft Engines"
Visiting periods at Rolls-Royce Deutschland, Combustion Department, Dr. R. Eggels (03/07 – 08/07) and at Cambridge University, U.K., Hopkinson Lab., Prof. E. Mastorakos (04/09 – 06/09)